Unsteady Hydrodynamics of Ships Moving in Confined Waterways

PhD Thesis

YIHAN LIU

Department of Naval Architecture, Ocean and Marine Engineering
University of Strathclyde, Glasgow

December 19, 2023

This thesis is the result of the author's original research. It has been composed by the author and has not been previously submitted for examination which has led to the award of a degree.

Abstract

When a ship is navigating on water surface, its resistance can be divided into three components: frictional resistance, eddy resistance, and wave-making resistance (Havelock, 1909). While in many cases, the steady component dominates the wave-making resistance, there are still certain instances where unsteady effects cannot be ignored. For example:

- Sudden changes of boundaries, such as the width and depth of the waterway. This may occur when ships navigate in port, harbor or lock environments. It will potentially increase the risk of collisions or grounding incidents.
- When a ship is overtaking (or being overtaken) or passing other vessels in busy waterways, the unsteady effects of the free surface can generate horizontal unsteady forces between the two ships. This can result in collisions between the vessels and lead to the blockage of the waterway.
- Another typical scenario is when a ship keeps accelerating in open area, particularly in extremely shallow depths. In this case, the unsteady effects will significantly increase after the ship's velocity exceeds the critical speed. At this point, the unsteady effects alter the flow field around the ship, resulting in changes in wave-making resistance.

This thesis posits that the aforementioned unsteady effects are closely correlated with unsteady waves on the free surface. Hence, the primary objectives of this research are two-fold:

1) To develop a linear unsteady numerical program which is capable of simulating

the unsteady free surface effects. This program will accurately capture the formation and evolution of unsteady waves.

2) To devise a real-time updating mesh method that handles changes in waterway boundaries and depths encountered during the simulation process. Additionally, it ensures temporal continuity for all cells on the free surface.

In this thesis, Chapter 1 will be an introduction and literature review of the research topic. Chapter 2 introduces the methodology used in this research. Chapters 3 to 5 constitute the main body of this thesis. Specifically, Chapter 3 presents the simulation of unsteady waves generated by a single object, with particular focus on the simulation of the previously mentioned scenario of a ship accelerating in shallow water. Chapter 4 aims to simulate multiple objects. In this chapter, the ship-to-ship problem and the unsteady bank effect within a confined waterway will be investigated. Due to the presence of interacting objects, the grid is required to be updated in real-time to accommodate changes in the boundary conditions. The simulation results will be compared with experimental data to validate their accuracy. Chapter 5 will build upon the foundation established in Chapter 3 by extending the grid handling techniques to account for unsteady banks. Additionally, the unsteady hydrodynamic model developed in Chapter 2 will also be incorporated. This integration will enable the simulation of the intricate wave phenomena that occurs during the process of a vessel entering a lock. The simulation results will be compared against experimental data as well as computational fluid dynamics (CFD) results to validate their accuracy. This comparative analysis serves to ensure the reliability and fidelity of the simulation outcomes. By undertaking these efforts, Chapter 4 aims to provide a comprehensive understanding of the wave behavior within the lock chamber during vessel entry, contributing to the advancement of knowledge in the field of unsteady water dynamics. Finally, Chapter 6 serves as the conclusion which summarizing all the achievements of this thesis and also proposing future directions for research.

Contents

List of Figures

List of Tables

Preface/Acknowledgements

I would like to express my great thanks and gratitude to my supervisor Dr. Zhiming Yuan at Strathclyde University, for his quality and kindly academic supervision, guidance as well as endless support throughout the years of this research. I thank him for the enormous concern for my work at Strathclyde University. During my PhD time, his kind encouragement of my current and future research development inspired me in what I do, especially for building a decent foundation for my academic career.

I also would like to thank Dr Saishuai Dai, Research Fellow at Strathclyde University, who has always been accessible to advise me for his valuable advice and helpful suggestions during my experiment.

I want to extend my great appreciation to Dr. Mingxin Li who has helped me with the experience of fluid dynamics from the beginning of my research.

I also wish to thank significantly my friends and schoolmates, Dr. Ming Zhang, Mr. Shuangrui Yu, Mr. Fengshen Zhu, Mr. Boyu Liao, Mr. Haitao Wu and Mr. Guangwei Zhao for their valuable help throughout my PhD programme.

Finally, I am grateful to my parents and wife, without their encouragement and understanding, I could not finish my PhD career.

Chapter 0. Preface/Acknowledgements

Chapter 1

Introduction

1.1 Background

With the continuous growth in global trade demands, a significant volume of goods is transported worldwide through vital transportation hubs such as the Suez Canal, Panama Canal, and Kiel Canal, which connect various parts of the world. However, this increased activity has resulted in exceptionally congested waterways. Despite the surge in maritime traffic, expanding the dimensions of these waterways, including canals or locks, is not easily feasible, leading to inadequate navigational safety margins. Consequently, the navigation of numerous large vessels through these restricted water channels, such as canals or locks, brings challenges to maritime safety. The limited maneuvering space within these narrow passages increases the risks associated with collisions, grounding, and other maritime incidents. Resolving these safety issues is crucial for ensuring the smooth and secure flow of maritime trade and navigation. In fact, any accidents occurring in these busy waterways can potentially cause severe loss of life and economic damage. The recent incident in 2021, where the Suez Canal was blocked for a prolonged period, serves as a prominent example. This event not only disrupted global trade but also inflicted significant financial losses on the affected businesses, disrupting supply chains and generating cascading effects throughout the global economy.

Describing the hydrodynamic characteristics of an object navigating through a narrow

waterway with abrupt variations is an exceptionally challenging task. In such scenarios, the fluid undergoes rapid compression as it traverses along the sides and beneath the vessel, giving rise to the generation of a return flow and a phenomenon known as the "piston effect" within the waterway. These intricate interactions pose significant difficulties in accurately predicting the hydrodynamic behavior associated with ship-lock effects.

Based on the continuity of the free-surface boundary conditions in time, the methods employed in the study can be categorized into quasi-steady and fully unsteady approaches. The quasi-steady method neglects all unsteady terms in the free-surface conditions, except when considering pressure calculations using the Bernoulli equation. This method is highly effective for solving the hydrodynamic problems of vessels moving at a constant velocity in open water areas. On the other hand, the fully unsteady method retains the unsteady terms in the process of solving the free-surface conditions, allowing for the interdependence of the studied problem at each time step. This approach is particularly effective in solving problems involving unsteady boundaries such as unsteady bank or step bottom problems.

This document represents a hybrid thesis format, consisting of published papers and conference contributions. It comprises an introductory section (Chapter 1), followed by substantial chapters (Chapters 2-5) presenting the research findings, and concluding with a summary (Chapter 6). The substantial chapters encompass individual research articles and conference papers, predominantly authored by the primary researcher.

1.2 Literature review

In the past few decades, extensive research has been conducted on the inviscid steady flow problems of ships using potential flow theory. Initially, a two-dimensional (2D) method known as strip theory was employed to investigate the hydrodynamic behavior of ships in confined waterways. This method, utilized by Tuck (1964, 1966, 1967) and Beck et al. (1975), is based on the assumption of slender ships and offers efficiency and predictability. However, its limitations become evident as it fails to provide sufficiently accurate results due to the neglect of three-dimensional (3D) effects. As a result, the

3D potential flow method remains one of the most commonly employed approaches for free surface effects, as indicated by reliable outcomes obtained from published results (Xu et al., 2016; Yao and Zou, 2010; Yuan, 2019).

However, it is crucial to acknowledge that previous studies have overlooked the significant influence of the unsteady effects on the free surface. Unsteady effects play a vital role in various scenarios, including ship acceleration, interactions among multiple bodies, and changes in waterway boundaries or depths. Neglecting these effects would be imprudent as they have a profound impact on the hydrodynamics of the system in such situations. Specifically, unsteady effects primarily stem from the unsteady flow around the ship, as highlighted by research conducted by Day et al. (2009) and Doctors et al. (2008).

Therefore, to gain a comprehensive understanding of the unsteady effects in ship hydrodynamics, this research focuses on three aspects of unsteady effects: 1) the acceleration effect of ships, 2) passing ship effects, and 3) ship-lock effects. By investigating how these unsteady effects impact the ship's resistance and the generated wave field, valuable insights can be gained. This research aims to provide a more holistic perspective on ship hydrodynamics by considering the complexities associated with unsteady phenomena.

1.2.1 The acceleration effect of ships

Predicting ship resistance has historically been treated as a steady problem. That is, a single resistance value is obtained for each condition, for example, for each combination of speed and water depth. There are however several contributions to the study of unsteady ship resistance estimation. To the best of the authors' knowledge, Havelock (1949) was the first to investigate the transient wave resistance on a submerged body. Havelock (1949) focused on a cylinder with uniform acceleration, expressing the wave resistance as the sum of a component at constant velocity and a component due to the effect of the acceleration. Following Havelock (1949), Lunde (1951, 1957) developed a mathematical theory to predict transient wave resistance. Later, Wehausen (1961) proposed an asymptotic formulation expressing the unsteady

wave resistance whose oscillations are predicted to decay inversely with time. Calisal (1977) extended Wehausen's (1961) method to include the development of the wave pattern in unrestricted water. Pinkster (2004) developed a potential flow solver to investigate the ship-to-ship problem, where the unsteady hydrodynamic force can be expressed with the aid of an added mass term. More recently, Day et al. (2009) built on Wehausen's (1961) work to include the effect of finite depth as well as width in a towing tank, which Wehausen (1961) considered infinite.

Experimental and theoretical investigations on unsteady resistance are primarily motivated by the performance of unconventional vessels such as hover craft (Barratt, 1965; Doctors and Sharma, 1972; Haussling and Van Eseltine, 1978; Yeung, 1975). These craft have historically been simplified as two-dimensional pressure distributions on the water surface (Doctors, 1975, 1993). The aforementioned studies were motivated by the presence of oscillations in the time-history signal of craft towed in a tank. The key problem in such cases is that the oscillation amplitude in the time-history of the resistance can be significant and may complicate the accurate measurement of the steady value (Li et al., 2020). Although a multitude of unsteady wave drag theories have been proposed, as shown above, the subject of a ship accelerating past a critical depth Froude number is rarely investigated.

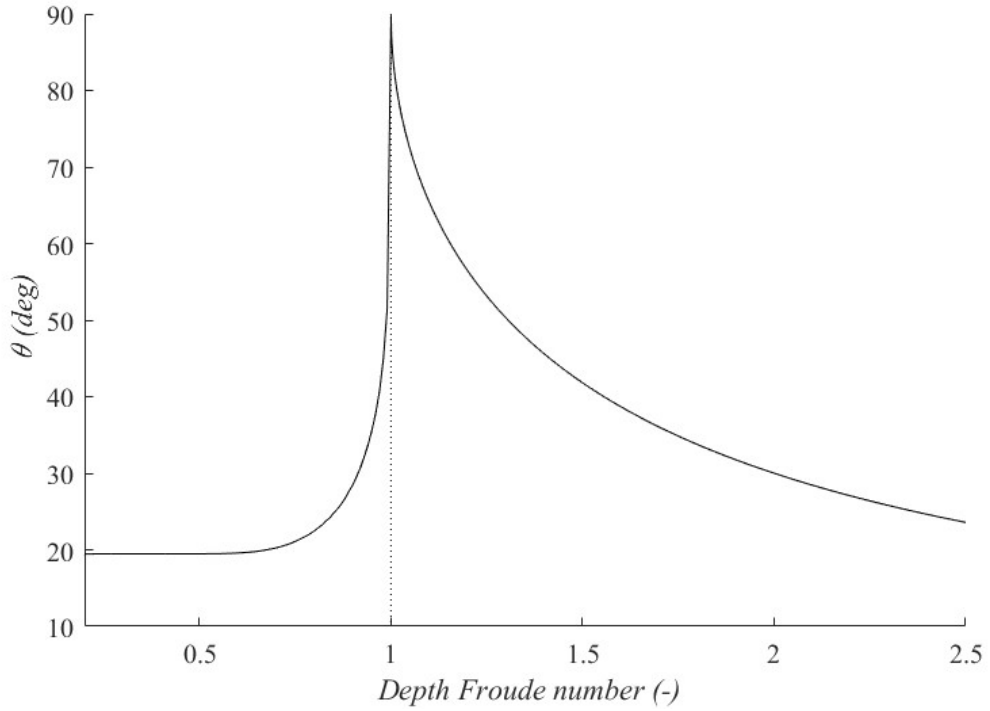

Figure 1.1: Kelvin half angle as a function of the depth Froude number. The relationships used to construct this figure are given in Havelock (1949)). Experimental measurements of the Kelvin half angle can be found in Johnson (1957).

In shallow waters, the Kelvin wake and corresponding to the angle between each arm of the V-shaped wave pattern and centreline (θ) depends on its depth Froude number (Lee and Lee, 2019). According to theories, when F_h=1 the wave pattern is transformed into a wave front that is perpendicular to the ship centreline (Havelock, 1908). That is, the Kelvin half-angle is equal to 90° (Tunaley, 2014) as shown in Figure 1.1.

Many approaches to modelling ship drag theoretically are unable to re-create the phenomena occurring at F_h=1. For example, the well-known slender body theory (Tuck, 1966, 1967) predicts a singularity at that speed. Feldman (1972) and later, Gourlay and Tuck (2001) addressed this gap, but the methodology is valid for a ship travelling at a uniform speed. There are also thought to be non-linear and dispersive effects one must handle at and around the critical depth Froude number. In addition, one must consider unsteady effects when a ship accelerates. The present study

compares a linear unsteady potential flow solver with an unsteady Reynolds-Averaged Navier-Stokes (URANS) solver to establish the relative importance of nonlinear and unsteady effects. Specifically, if unsteady effects dominate resistance with little contribution of nonlinear effects, then the solutions from the two aforementioned solvers must agree. If nonlinear effects are important, one expects to observe some disagreement between the two adopted methodologies.

To the best of the authors' knowledge, Kevorkian and Yu (1989) were first to focus exclusively on trans-critical transitions caused by changes in the water depth. Redekopp and You (1995) modelled a disturbance passing through the critical depth Froude number using the forced Korteweg-deVries (fKdV) equation. The above approaches model the problem in a single dimension. Jiang et al. (2002) combined a slender body approach with Boussinesq equations to model the two-dimensional free surface as a vessel advances over a restriction in the water depth. Later, Torsvik et al. (2006) used a set of forced Boussinesq equations to study the trans-critical transition of pressure distribution on the water surface. The acceleration intensity was shown to govern whether a solitary wave is emitted from the vessel, with relatively low acceleration intensities allowing the solitary wave to detach and propagate independently of the hull.

Shockwaves produced when a craft breaches the critical depth Froude number are shown by Jiang et al. (2002) and Grue (2017) using Boussinesq-type modelling, however, both of these pieces of research employed a transition in the water depth to create a rapid and significant increase in the depth Froude number. The authors' previous work on fully confined water (Terziev et al., 2021b) investigated the water depth transition problem using a URANS approach.

As shown above, a number of studies have examined problems similar to those explored herein. However, no previous research has compared fully non-linear Navier-Stokes-based methodologies with potential flow solutions to investigate the problem at hand. As a consequence, the viscous influence on the ship's resistance under the conditions examined subsequently remains unknown.

Additionally, the hydrodynamic forces that depend on acceleration are commonly

referred to as added mass. However, it has been established in many previous studies that the magnitude of added mass, or the coefficient of added mass, primarily depends on the shape of the object and its velocity, rather than the acceleration. For example, studies by Flagg and Newman (1971) and Newman (2018) investigated the influence of the width of a ship and the water depth on the added mass while Ghassemi and Yari (2011) studied the added mass coefficient computation of sphere, ellipsoid and marine propellers. Wakaba and Balachandar (2007) studied the added mass force at finite Reynolds and acceleration numbers. They found the added mass coefficient is acceleration independent. A similar conclusion is also mentioned in Javanmard et al.'s (2020) research, which focused on using a new CFD method to calculate the translational added mass coefficients of underwater vehicles. However, it should be noted that in this particular research, accurately reflecting the contribution of added mass to wave-making resistance is challenging. This is because the hydrodynamic forces in Eq. (2.62) are not decomposed to extract distinct added mass forces. Instead, the unsteady hydrodynamic forces are determined by directly solving for the velocity potential φ, where the influence of added mass is inherently incorporated within the fully unsteady velocity potential φ. In fact, in other studies (Doctors and Sharma, 1972; Pinkster, 2004; Shebalov, 1970; Wehausen, 1961) related to acceleration, the added mass as a component in the Bernoulli equation has indeed been mentioned. However, it is worth noting that it has not been specifically isolated and studied separately in those cases.

1.2.2 Passing ship effects

In a heavy traffic harbor area, it is normal for ships to pass each other very closely. In this case, the moored ship always experiences significant hydrodynamic forces caused by ship-generated waves. This can result in unwanted large motion and high sway forces which are reasons for various accidents. Such as NTSB (1991) once recorded a damage case caused by the passing ship effect. In addition, these effects will be significantly amplified in shallow water or confined waterway environments. These passing effects can be divided into two types according to the passing ship speed. In the first case, the

passing ship speed is so low that the ship-generated waves will not be very significant which means the hydrodynamic forces of the moored ship normally come from the pressure variation because of the passing ship. In this case, the most important factors affecting the passing effect are the size of the passing ship, the distance between the two ships, the existence of the bank wall and the water depth. In the second condition, the moored ship will be passed by another high-speed ship. At this time, the ship-generated wave is the main medium for transmitting the hydrodynamic forces acting on the moored ship. It is not difficult to understand that the size and intensity of the waves are the key factors affecting the ship-passing effect in this case.

So far, potential flow models have been widely used to study ship-passing effects. In particular, the classical slender body theory is still useful in predicting ship-ship interactions. Tuck and Newman (1976) use this theory to study the hydrodynamic forces between two ships. After that, Wang (1975) and Yeung (1978) also did similar researches with the slender body theory. Until a few years ago, Varyani and Krishnankutty (2006) calculated the hydrodynamic interaction between two ships in close proximity based on the slender body theory while one of the two ships is moored alongside the bank. Wang (2007) studied the problem of revolution translation between two slender bodies in close proximity based on the slender body theory and he solved an analytic solution with this method. More recently, the three-dimensional panel method has become the more commonly used method (Söding et al. 2005; Xiang and Faltinsen 2011; Xu et al. 2016; Zhou et al. 2012). From these studies, one obtained conclusion is the potential-flow solver performs well on the prediction of hydrodynamic forces between two ships while the ship speed is low. Benefit from the development of computer computing power, researchers have become accustomed to using various turbulence models based on CFD (Computational Fluid Dynamics) technology to study viscous effects on ship-ship problems (Jin et al. 2016; Sian et al. 2016;Zou and Larsson 2013).

However, it can be said that in the decades after Yeung (1978) published his study, the research of the ship-ship effect has made some progress, but the progress has not been satisfactory. In particular, unsteady interactions among multiple ships are often

overlooked. One important reason is that the free surface is always treated as a rigid wall so that the free surface effect can only be ignored, or the free surface is considered as a simple steady problem which means the contribution of unsteady terms are not included. Mousaviraad et al. (2016b) conducted experiments on the ship-ship interaction in still water and waves. They also performed URANS simulations while taking into account the free surface boundary conditions (Mousaviraad et al. 2016a). The above studies represent the capabilities of current CFD technology. Due to the significant increase in computer computing power, the current work is not limited to the interaction force itself, but also extends to the influence of free surfaces on the ship-ship effect. However, even so, neither in the CFD simulation nor in the model experiment, the wave elevation on the free surface is still not included in present studies. Moreover, when dealing with the case of two or even multiple ships moving at the same time, computationally demanding may still be the biggest bottleneck of the CFD method.

The studies mentioned above are often based on the assumption of low passing speed, which is often not the case in reality. As the passing speed increases, so does the range of the far-field wave, which is bound to affect another moored or moving ship. To study the free surface effect, Yuan et al. (2015) proposed an uncoupled method based on the superposition principle to account for the different speeds appearing in the free-surface boundary conditions. In this approach, the speed difference between the two ships is assumed to be small, so the problem can be approximated as two steady state problems. Subsequently, Yuan et al. (2019) extended their work to the time domain using a quasi-steady approach. At this time, the velocity terms in the free surface condition are taken into account, and the time terms are also added in the final calculation of forces. However, in this method, when solving the boundary equation, the unsteady terms in the free surface condition are still not included, which means the contributions of the unsteady terms are still not considered.

1.2.3 Ship-lock effects

Due to the complex hydrodynamic conditions, the maneuverability of ships when entering a lock has not been fully understood by researchers. According to the research work by Vantorre and Richter (2011), the hydrodynamic characteristics of the ship entering a lock will change with factors such as approach channel and approach structure layouts, water depth, translation waves, return flow, and cushion effects, etc. This conclusion can be verified by the phenomenon in real operations. In the process of entering the lock, the ship will inevitably experience a sudden narrowing of the channel and the water depth will decrease to a small value. This means the flow will be compressed to pass through the bottom and both sides of the ship which will result in an increase in flow velocity and a decrease in pressure on the ship. From analyzing the pressure distribution, it can be predicted the ship will sink towards the lock bottom.

At the same time, a wave-making resistance and pitch moment will be induced because of the pressure difference between the ship's bow and stern. In this case, one can imagine the wave-making resistance, sinkage and trim value of the ship will be amplified if the water depth keeps decreasing. On the other hand, if the shape of the waterway on the port and starboard side of the ship is asymmetric, the ship will also receive a lateral force and a yaw moment which can lead the ship skews towards the bank. All these phenomena will bring some potential risks to the ship entering a lock, such as grounding and collision. Actually, the blockage of the Suez Canal in March 2021 was caused by a cargo ship stranded in the waterway.

In order to investigate the ship's hydrodynamic behavior in confined waterways, researchers have done a lot of work in the past decades. In the early years, due to the limit of computing power, the experimental measurements were considered to be the most reliable approach to estimating the ship-bank, ship-bottom, ship-lock and ship-ship interactions. In the 1990s, a model test was carried out in the Towing Tank in Antwerp to study if the Pierre Vandamme lock in Zeebrugg can receive a bulk carrier with a large beam (Vantorre and Delefortrie 2013). The David Taylor Model Basin conducted a large number of experiments to study the difference of

maneuverability of ships in the Panama Canal with different cross-sections (Schoenherr 1960). Fujino (1968) proposed an empirical formula to calculate the lateral force and yaw moment of a ship in restricted waterways. From 2008 to 2009, Delefortrie et al. (2008, 2009) carried out a self-propelled model test to test the sailing performance of three different ship types in the third set of locks of the Panama Canal. In addition, Flanders Hydraulics Research and Ghent University conducted a series of model tests on ship-bank (Lataire et al. 2009; Lataire et al. 2016), ship-bottom (Lataire et al. 2012a; Lataire et al. 2016), ship-lock (Lataire et al. 2012b) and ship-ship interaction (Vantorre et al. 2002).

In the past few decades, there have been numerous research activities trying to establish a numerical tank and conduct ship hydrodynamic tests in virtual environments. With the rapid development of computer technology, CFD-based numerical methods have been widely used in this area. The CFD method does have advantages in dealing with some complex hydrodynamic problems. However, the calculations with the CFD method may require the support of High Performance Computing (HPC) platforms. In fact, although there are some successful cases of using the CFD method to simulate the hydrodynamic performance of ships in confined waterways (Sakamoto et al. 2007; Tezdogan et al. 2016; Zou and Larsson 2013), it is still difficult to use this method widely because of the large computational time. Therefore, the previously mentioned 3D potential flow method becomes one of the most commonly used methods for ship-lock problems. According to the published results (Xu et al. 2016; Yao and Zou 2010; Yuan 2019), the 3D potential flow solver can provide reliable results. However, in the framework of the 3D potential flow method, the free surface is usually treated as a rigid wall in ship-ship or ship-lock interaction problems, which means the complexity of the free surface, such as the non-linear and unsteady problems are both not considered. This is also why there are only very limited publications using the 3D potential flow method to study the ship-lock interaction problem.

1.3 Aims & Objectives

The purpose of this thesis is to investigate the unsteady hydrodynamics of ships in confined waterways. The unsteady effects of the free surface need to be taken into consideration. The ultimate goal of this research is to develop a linear unsteady algorithm to simulate the waves generated by ships during the process of entering a lock, including the return flow and piston phenomenon. Accordingly, the current research work includes the following aspects:

- Predicting the wave making resistance generated by an accelerating ship in open and shallow water areas.
- Study the passing ship problem to predict the unsteady interaction forces between multiple ships in a confined waterway, taking into account the variations in the free surface boundary caused by the presence of other vessels.
- Integrate the previous numerical algorithms to predict the unsteady wave resistance experienced by ships during the process of entering a lock, as well as the wave phenomena generated within the lock. It is important to emphasize that, in this scenario, the free surface mesh should be updated in real-time to accommodate the changing boundaries of the free surface and also ensure that all elements on the free surface remain connected at each time step.

1.4 Novelty and Contribution to the Knowledge

Novelty of the research

- This thesis presents a in-house developed potential flow solver, named MHydro, which is based on 3D boundary element method that established by a Rankine type Green function. It successfully accomplishes the construction of a fully unsteady free surface.
- This is the first time to expand the ship acceleration concern beyond a critical depth Froude number, leveraging a comparison of Unsteady Reynolds Averaged

Navier-Stokes outcomes and 3D panel-based potential flow solutions via MHydro.

- This is also the first work to systematically model the unsteady free-surface waves when a ship enters a lock. The methodology developed in this thesis is novel and original. All the predicted results are validated against model tests.
- In this thesis, a novel real-time updated method for meshing the free surface has been applied in the potential flow solver MHydro, ensuring the continuity of all panels on the free surface at each time step.
- This thesis implement a novel return flow model to predict the unsteady hydrodynamic forces during ship entering a lock. This model showed the importance of the return flow, particularly when the blockage effects are evident.

Contribution to the Knowledge

- It has been observed that, during the ship acceleration process, the relationship between wave making resistance and acceleration experiences a sudden change near the critical velocity. Prior to reaching the critical velocity, wave making resistance consistently increases with increasing acceleration. However, once the velocity surpasses the critical point, the relationship becomes inverse, where higher acceleration results in reduced wave resistance.
- During the process of a ship entering a lock, it has been observed that the fluid inside the lock exhibits a piston phenomenon, characterized by simultaneous rising and falling motion of the free surace in the lock. This phenomenon is intricately linked to the unsteady effects of the free surface and is also influenced by sudden constriction of the waterway and the closure of lock gate.
- A novel numerical tool has been introduced, which enables the precise estimation of unsteady hydrodynamic forces experienced by moving vessels. This tool also anticipates the wave field generated on the free surface and the resulting velocities of fluid particles.

1.5 Thesis Outline

The objective of this thesis is to investigate the unsteady hydrodynamic effects caused by ships during the process of entering a lock. To address this issue, the thesis first examines the unsteady effects induced by continuously accelerating ships in open water areas, specifically focusing on the shallow water region. Subsequently, the study explores the unsteady hydrodynamic interactions between multiple ships in a restricted channel. Finally, the investigation extends to the ship-lock interaction problem. The structure of the thesis is organized into several sections, as illustrated in Figure 1.2:

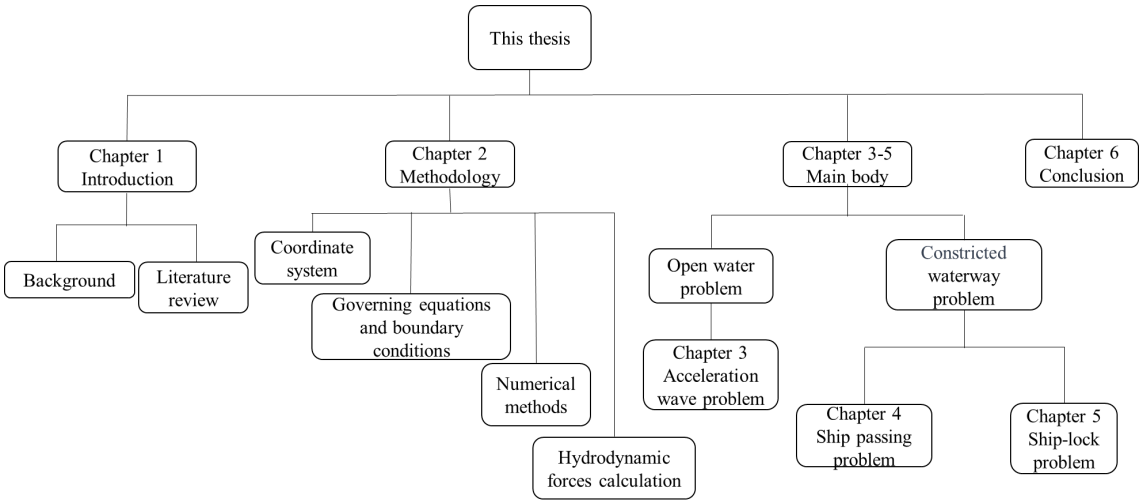

Figure 1.2: Thesis outlines

In this research, the Rankine source method, originally proposed by Hess and Smith (1964), will be utilized. This method incorporates simple Green's functions into the boundary integral formulation, distributing sources on the object surface, the free surface, and the seabed. This allows for a flexible selection of free surface and seabed conditions within the boundary value problem (BVP). A 3D boundary element program based on the Rankine source method then will be developed to investigate the unsteady wave resistance encountered by ships entering a lock, as well as the various wave phenomena generated within the lock. Ultimately, the simulated results will be compared with experimental data to validate their accuracy.

Chapter 2

Methodology

2.1 Coordinate system

Taking into account the characteristic motion of ships in waves, this dissertation establishes two distinct right-handed coordinate systems for the investigation of the problem.

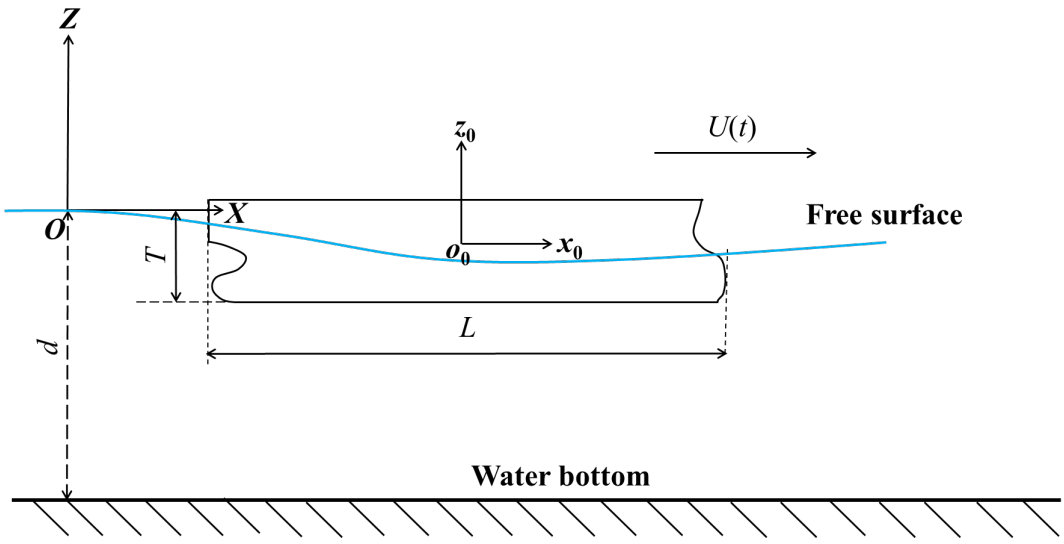

(a)

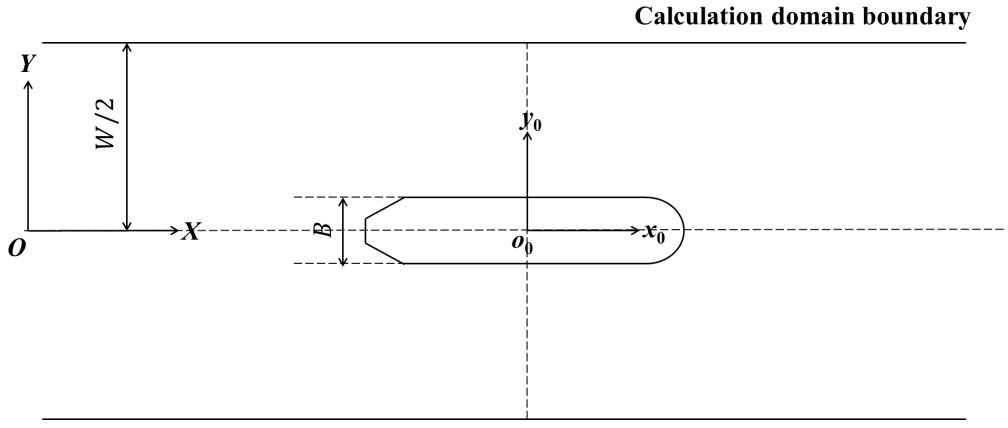

(b)

Figure 2.1: Coordinate system definition, where d and T means the water depth and the draft of the ship, respectively; L is the length of the ship and W and B represent the width of the calculation domain and the ship.

As illustrated in Figure 2.1, the first coordinate system is the spatial fixed coordinate system denoted as $O-XYZ$. It remains stationary and unaffected by fluid or vessel motion. The undisturbed still water surface is chosen as the OXY plane, with the OZ axis oriented vertically upward. Secondly, the body-fixed coordinate system $o_0-x_0y_0z_0$ is affixed to the vessel and moves with it. Equations pertaining to the vessel's surface expressed in this coordinate system do not contain time variables. The origin o_0 is located at the vessel's center of gravity, the positive direction of the ox axis points towards the bow of the vessel and lies in the midship plane, the $o_0x_0y_0$ plane coincides with the still water surface when the vessel is in its equilibrium position, and the o_0z_0 axis is oriented vertically upward with respect to the $o_0x_0y_0$ plane.

2.2 Governing equations and boundary conditions

Based on the potential flow theory, the fluid is assumed to be ideal which means it's inviscid, irrotational, and incompressible. The wave motion is described by the velocity potential $\Phi(x, y, z, t)$ and the free surface wave elevation velocity potential $\zeta(x, y, t)$.
In the body-fixed coordinate system, the velocity potential $\Phi(x, y, z, t)$ can be decomposed as

$$\Phi(x, y, z, t) = \varphi_s(x, y, z) + \varphi_u(x, y, z, t) \tag{2.1}$$

where $\varphi_s(x, y, z)$ is the time-independent part while $\varphi_u(x, y, z, t)$ is the unsteady part which represents the flow motion induced by the external disturbance such as the presence of other ships or changes in waterways. In this research, the uniform-flow is considered as the basic steady flow, so the Eq. (2.1) can be simplified as

$$\Phi(x, y, z, t) = -Ux + \varphi_u(x, y, z, t) \tag{2.2}$$

The velocity potential $\varphi_u(x, y, z, t)$ should satisfy the Laplace equation

$$\frac{\partial^2 \varphi_u}{\partial x^2} + \frac{\partial^2 \varphi_u}{\partial y^2} + \frac{\partial^2 \varphi_u}{\partial z^2} = 0 \tag{2.3}$$

Only with appropriately specified initial boundary conditions provided in advance can the solution to the Laplace equation be determined. Therefore, correctly describing the initial boundary conditions is equally important as solving the equation itself. The following discussion pertains to the relevant initial boundary conditions for the problem of ship motion in waves.

(1) Body surface condition

The ship's surface is a solid surface, impervious, forming a part of the boundary of the flow field around the ship. Furthermore, the ship's surface has a velocity, so the normal velocity at any point on the ship's surface in the x-direction should be equal to the ship's velocity $U(t)$. Therefore, on the body surface, the following condition should be satisfied:

$$\frac{\partial \varphi_u}{\partial \boldsymbol{n}} = U n_1 \tag{2.4}$$

where $n = (n_1, n_2, n_3)$ is the unit normal vector on body-surface. $\frac{\partial}{\partial n}$ represents the partial derivative which is defined to be positive into the fluid domain. On the right-hand side of the equation, U_n represents the projection of the velocity at a point on the body surface in the normal direction, while on the left-hand side, it represents the normal component of the velocity of the fluid particles immediately adjacent to

that point. This relationship ensures that there is no fluid penetration through the solid surface from one side to the other, essentially providing a boundary condition on the solid wall surface from a kinematic perspective. Finally, in this thesis, as the ship's motion is characterized solely along the x-direction, thus n_1 is substituted into Eq. (2.4).

(2) Free surface condition

Using the function ζ to represent the free surface height, i.e., $z = \zeta(x, y, t)$, and , the boundary condition for the free surface is as follows:

$$\frac{\partial \zeta}{\partial t} - U\frac{\partial \zeta}{\partial x} + \frac{\partial \varphi_u}{\partial x}\frac{\partial \zeta}{\partial x} + \frac{\partial \varphi_u}{\partial y}\frac{\partial \zeta}{\partial y} - \frac{\partial \varphi_u}{\partial z} = 0, \text{ at } z = \zeta \tag{2.5}$$

$$\frac{\partial \varphi_u}{\partial t} - U\frac{\partial \varphi_u}{\partial x} + g\zeta + \frac{1}{2}\nabla\varphi_u \cdot \nabla\varphi_u + \frac{P}{\rho} = 0, \text{ at } z = \zeta \tag{2.6}$$

where g is the gravitational acceleration, ρ is the fluid density and P is the forcing pressure on the free-surface.

The physical interpretations of equations Eq. (2.5) and Eq. (2.6) are as follows: Eq. (2.5) signifies that fluid particles on the wave surface always remain on the wave surface, and this is referred to as the kinematic boundary condition. Eq. (2.6) implies that the pressure at a certain point on the wave surface always equals the atmospheric pressure, and this is known as the dynamic boundary condition. Both of these expressions contain nonlinear terms. Consequently, even though the Laplace equation itself is linear, the inherently nonlinear nature of the free surface conditions transforms the entire initial-boundary value problem into a nonlinear problem. For the sake of simplification in problem-solving, it is common practice to set the relative pressure at the free surface to zero and neglect surface tension on the free surface. Additionally, the free surface conditions often omit nonlinear and unsteady terms, resulting in the following relationships:

$$-U\frac{\partial \zeta}{\partial x} - \frac{\partial \varphi_u}{\partial z} = 0 \tag{2.7}$$

$$-U\frac{\partial \varphi_u}{\partial x} + g\zeta = 0, \tag{2.8}$$

Subsequently, by performing the operation $\partial/\partial x$, Eq. (2.8) can be substituted into Eq. (2.7), so the above two equations can be combined to the well-known Newman-Kelvin free surface condition:

$$\zeta = \frac{U}{g}\frac{\partial \varphi_u}{\partial x} \tag{2.9}$$

$$\frac{\partial \zeta}{\partial x} = \frac{U}{g}\frac{\partial^2 \varphi_u}{\partial x^2} \tag{2.10}$$

$$U^2\frac{\partial^2 \varphi_u}{\partial x^2} + g\frac{\partial \varphi_u}{\partial z} = 0 \tag{2.11}$$

The free surface condition mentioned above has been utilized in Dr. Yuan's research since 2014. All nonlinear and unsteady terms are disregarded, and only during the calculation of wave elevations and hydrodynamic forces can the unsteady effects be reflected in the Bernoulli integration (further details are provided in Section 2.4). Consequently, this method is also known as the quasi-steady method.

However, this thesis aims to investigate the unsteady effects of the free surface. For this purpose, a three-level difference scheme has been introduced to discretize the free surface conditions while preserving all the unsteady terms. This upgraded method is termed the fully unsteady method, and its specifics will be extensively elaborated upon in Section 3.3.

(3) Radiation condition

When dealing with external domain problems, apart from boundary conditions at the body surface and the free surface, corresponding boundary condition must also be provided at infinity, known as radiation conditions. In time domain analysis, it is generally assumed that the fluid starts moving at a certain moment, and before that, the fluid is at rest. In simple terms, one can assume that waves should vanish at infinity. Therefore, the radiation condition is given in the following form:

$$\varphi_u \to 0, \zeta \to 0 \text{ as } \sqrt{x^2+y^2} \to \infty \tag{2.12}$$

(4) Bottom and side-wall surface conditions

The boundary condition on the sea bottom and side walls is quite similar to the body surface condition which can be expressed as

$$\frac{\partial \varphi_u}{\partial \boldsymbol{n}} = 0 \tag{2.13}$$

Thus, the solution for the velocity potential φ_u, governed by the aforementioned Laplace equation and boundary conditions, is as follows:

$$\begin{cases} \frac{\partial^2 \varphi_u}{\partial x^2} + \frac{\partial^2 \varphi_u}{\partial y^2} + \frac{\partial^2 \varphi_u}{\partial z^2} = 0, & \text{In the fluid domain} \\ U^2 \frac{\partial^2 \varphi_u}{\partial x^2} + g \frac{\partial \varphi_u}{\partial z} = 0, & \text{On the free surace} \\ \frac{\partial \varphi_u}{\partial \boldsymbol{n}} = U n_1, & \text{On the body surface} \\ \frac{\partial \varphi_u}{\partial \boldsymbol{n}} = 0, & \text{On the control surface} \\ \varphi_u \to 0, \zeta \to 0, & \sqrt{x^2+y^2} \to \infty \end{cases} \tag{2.14}$$

2.3 Numerical implementations

2.3.1 Green's function

In the previous section, the solution for the velocity potential φ_u was provided. However, in practical problems, due to the complexity of boundary conditions, finding solutions analytically can be highly challenging. Therefore, numerical methods have become a more effective solution. Common numerical methods include the Green's function method, the finite element method, and the finite difference method. In the calculation of ship hydrodynamic performance, the Green's function method, also known as the boundary integral equation method or the boundary element method, is commonly used. This method is quite flexible in its application and can adapt to various complex boundaries encountered in practical engineering problems.

Green's function method comes in two primary forms: the mixed distribution method that includes both distributed sources (and sinks) and dipoles, and the source distribution method that only involves sources (and sinks).

For the mixed distribution form of the Green's function method, its boundary integral equation is as follows:

$$C(p)\Phi(p,t) = \iint_S \left[\Phi(q,t)\frac{\partial G(p,q)}{\partial n} - G(p,q)\frac{\partial \Phi(q,t)}{\partial n} \right] \mathrm{d}S \tag{2.15}$$

where p represents the field point; q represents the source point; S represents the entire boundary of the domain, which consists of the body surface S_0, the free surface S_F, and the radiation control surface S_∞. The coefficient C has the following value:

$$C(p) = \begin{cases} 1 & \text{In the fluid domain} \\ 0 & \text{Out of the fluid domain} \\ \alpha(p) & \text{On the boundary of the fluid domain} \end{cases} \tag{2.16}$$

where $\alpha(p)$ represents the solid angle subtended by the boundary surface at point p in space.

For the source distribution form of the Green's function method, the boundary integral equation can be expressed as:

$$\frac{\partial \Phi(p,t)}{\partial n} = C(p)\sigma(p,t) + \iint_S \sigma(q,t)\frac{\partial G(p,q)}{\partial n}\ \mathrm{d}S \tag{2.17}$$

$$\Phi(p,t) = \iint_S \sigma(q,t)G(p,q)\mathrm{d}S \tag{2.18}$$

where $\sigma(q,t)$ is the source term, representing the intensity of sources at point p.

Velocity potentials on different boundary surfaces should satisfy the corresponding boundary conditions, meaning that the velocity potential or its normal derivative is specified on these boundary surfaces. By substituting these conditions into the above boundary integral equation and solving it, it will be easy to obtain the velocity potential at any location in the flow field. This way, the equations only contain the values of

the velocity potential on the boundaries, which significantly reduces the computational workload. Therefore, in terms of computational efficiency, the Green's function method is superior to domain-type methods such as finite difference or finite element methods.

2.3.2 3-D boundary element method

When discussing the motion of ships in waves, the boundaries of the domain typically consist of the body surface S_B, the free surface S_F and either the control surface S_C or the far-field radiation surface S_R . If one arbitrarily chooses a Green's function that satisfies the Laplace equation, such as the simplest one, employing Rankine sources, the function can be modified as

$$G(\overrightarrow{\mathbf{X}}, \overrightarrow{\xi}) = \frac{1}{r} \tag{2.19}$$

where $r = \sqrt{(x-\xi)^2 + (y-\eta)^2 + (z-\zeta)^2}$ is the distance between the source point $\overrightarrow{\mathbf{X}} = (x, y, z)$ and field point $\overrightarrow{\xi} = (\xi, \eta, \zeta)$. However, considering the sources need to be distributed not only on the free surface and the ship hull but also on the control surface, and since the seabed is often not established but is treated as a mirror, the Green's function utilizing the method of images should be expressed as follows

$$G(\overrightarrow{\mathbf{X}}, \overrightarrow{\xi}) = \frac{1}{r} + \frac{1}{r'} \tag{2.20}$$

where $r' = \sqrt{(x-\xi)^2 + (y-\eta)^2 + (z+2d+\zeta)^2}$ is the distance between the image source point and field point. Therefore, the Green function in Eq. (2.20) can satisfy the sea bottom boundary condition.

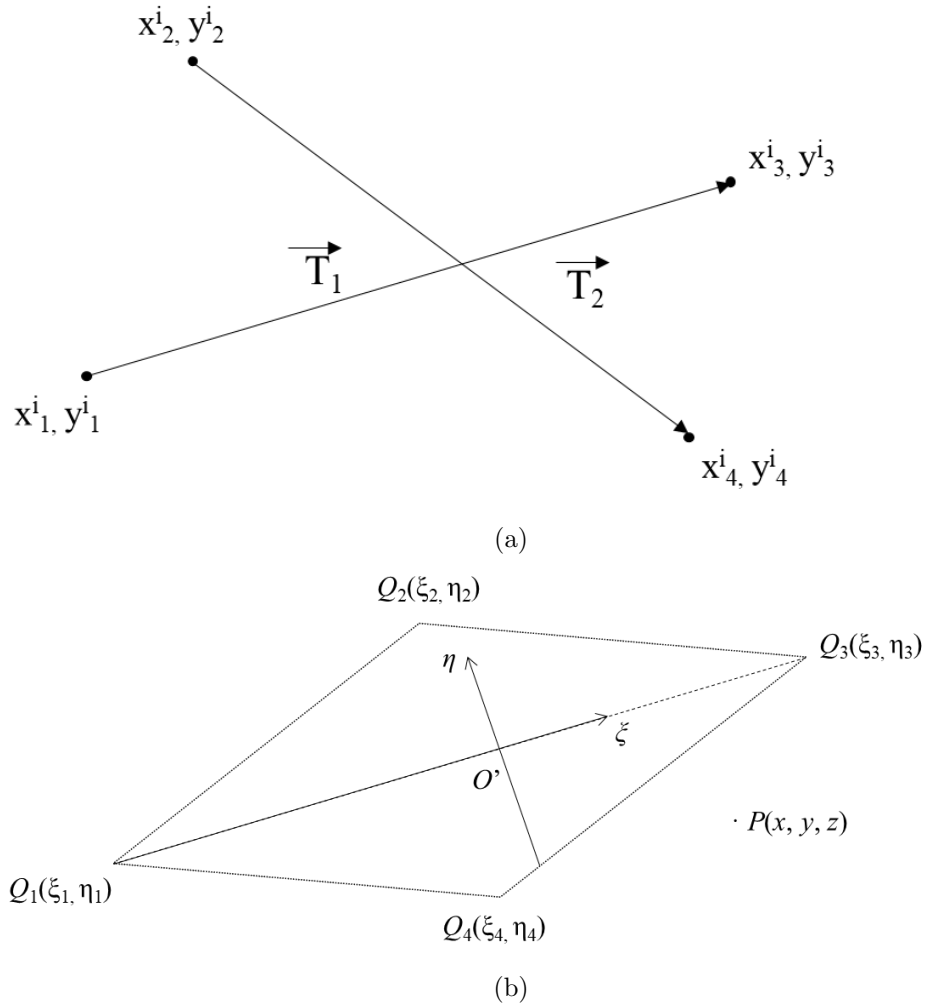

Figure 2.2: Coordinate systems, (a) input points in reference coordinate system where $\vec{T_1}$ and $\vec{T_2}$ are diagonal vectors; (b) quadrilateral element coordinate system $O' - \xi\eta\zeta$, where O' is on the geometry centroid, P is the source of the element and ζ axis on its normal vector.

In this method, there are two coordinate systems, one is the reference coordinate system and another is the element coordinate system, as shown in Figure 2.2. For input data and the associated influence coefficients, they should be based on the reference coordinate system. The element coordinate system is only utilized when calculating the specific induced velocity components.

Between the two coordinate systems, there is a transformation matrix enables a straightforward conversion of coordinates (Hess and Smith, 1964):

In general the two diagonal vectors in reference system are not orthogonal, use i represents input data, so their components are as follows

$$\begin{array}{lll} \mathrm{T_{1x}} = \mathrm{x_3^i} - \mathrm{x_1^i} & \mathrm{T_{1y}} = \mathrm{y_3^i} - \mathrm{y_1^i} & \mathrm{T_{1z}} = \mathrm{z_3^i} - \mathrm{z_1^i} \\ \mathrm{T_{2x}} = \mathrm{x_4^i} - \mathrm{x_2^i} & \mathrm{T_{2y}} = \mathrm{y_4^i} - \mathrm{y_2^i} & \mathrm{T_{2z}} = \mathrm{z_4^i} - \mathrm{z_2^i} \end{array} \tag{2.21}$$

The vector $\vec{N} = \vec{T_1} \times \vec{T_2}$ has the following components:

$$\begin{aligned} N_x &= T_{2y}T_{1z} - T_{1y}T_{2z} \\ N_y &= T_{1x}T_{2z} - T_{2x}T_{1z} \\ N_z &= T_{2x}T_{1y} - T_{1x}T_{2y} \end{aligned} \tag{2.22}$$

So the unit normal vector $\vec{n}$ to the pane of the element can be expressed as

$$\begin{aligned} n_x &= \frac{N_x}{N} \\ n_y &= \frac{N_y}{N} \\ n_z &= \frac{Nz}{N} \end{aligned} \tag{2.23}$$

where

$$N = \sqrt{N_x^2 + N_y^2 + N_z^2} \tag{2.24}$$

Now, the plane of the element can be completely determined by a specified point whose coordinates $\overline{x}, \overline{y}, \overline{z}$are the average of the four input points

$$\begin{aligned} \overline{x} &= \frac{1}{4}\left(x_1^i + x_2^i + x_3^i + x_4^i\right) \\ \overline{y} &= \frac{1}{4}\left(y_1^i + y_2^i + y_3^i + y_4^i\right) \\ \overline{z} &= \frac{1}{4}\left(z_1^i + z_2^i + z_3^i + z_4^i\right) \end{aligned} \tag{2.25}$$

Now it is possible to project the input points into the plane of the element along the normal vectors, lead to the corner points in the quadrilateral element system. The signed distance of the k-th (k=1, 2, 3, 4) point is

$$d_k = n_x\left(\overline{x} - x_k\right) + n_y\left(\overline{y} - y_k\right) + n_z\left(\overline{z} - z_k\right) \quad k = 1, 2, 3, 4 \tag{2.26}$$

It turns out that all the d_k have the same magnitude, the sole distinction lies in the opposing signs of points 1 and 3 when compared to points 2 and 4. So d_k can be presented as

$$d_k = (-1)^{k-1} d_1 \quad k = 1, 2, 3, 4 \tag{2.27}$$

Then the magnitude of the common distance is

$$d = |d_1| \tag{2.28}$$

Until now, the corner points in the reference coordinate system are given by

$$\begin{aligned} x'_k &= x^i_k + n_x d_k \\ y'_k &= y^i_k + n_y d_k \quad k = 1, 2, 3, 4 \\ z'_k &= z^i_k + n_z d_k \end{aligned} \tag{2.29}$$

In order to construct the element coordinate system, two perpendicular unit vectors $\vec{t_1}$ and $\vec{t_2}$ in the element plane are necessary:

$$\begin{aligned} t_{1x} &= \frac{T_{1x}}{T_1} \\ t_{1y} &= \frac{T_{1y}}{T_1} \\ t_{1z} &= \frac{T_{1z}}{T_1} \end{aligned} \tag{2.30}$$

where

$$T_1 = \sqrt{{T_{1x}}^2 + {T_{1y}}^2 + {T_{1z}}^2} \tag{2.31}$$

Because $\vec{t_2}$ can also be expressed by $\vec{n} \times \vec{t_1}$, so its components are

$$\begin{aligned} t_{2x} &= n_y t_{1z} - n_z t_{1y} \\ t_{2y} &= n_z t_{1x} - n_x t_{1z} \\ t_{2z} &= n_x t_{1y} - n_y t_{1x} \end{aligned} \tag{2.32}$$

where $\vec{t_1}$ is the vector parallel to the x or ξ axis while $\vec{t_2}$ is parallel to the y or η axis and $\vec{n}$ is parallel to the z or ζ axis.

Now, everything is ready for the transformation between the two coordinate systems. The transformation matrix is necessary which is composed of three basis unit vectors $\vec{t_1}$, $\vec{t_2}$ and $\vec{n}$:

$$\begin{aligned} a_{11} = t_{1x} \quad a_{12} = t_{1y} \quad a_{13} = t_{1z} \\ a_{21} = t_{2x} \quad a_{22} = t_{2y} \quad a_{23} = t_{2z} \\ a_{31} = n_x \quad a_{32} = n_y \quad a_{33} = n_z \end{aligned} \tag{2.33}$$

Thus the following matrix is obtained

$$\begin{matrix} a_{11} & a_{12} & a_{13} \\ a_{21} & a_{22} & a_{23} \\ a_{31} & a_{32} & a_{33} \end{matrix} \tag{2.34}$$

Finally, one input space point x^i, y^i, z^i in the reference coordinate system $O - XYZ$ has the corner point has a projection on the elemental plane as (x', y', z') and the point (x, y, z) in the element coordinate system can be represented as follows:

$$\begin{aligned} x &= a_{11}\left(x' - x_o\right) + a_{12}\left(y' - y_o\right) + a_{13}\left(z' - z_o\right) \\ y &= a_{21}\left(x' - x_o\right) + a_{22}\left(y' - y_o\right) + a_{23}\left(z' - z_o\right) \\ z &= a_{31}\left(x' - x_o\right) + a_{32}\left(y' - y_o\right) + a_{33}\left(z' - z_o\right) \end{aligned} \tag{2.35}$$

where x_o, y_o, z_o is the coordinate of the origin of the element coordinate system in the reference coordinate system. It's also the geometry centroid of the element plane.

Once the elemental coordinate system has been established, it becomes possible to commence the computation of the induced velocity caused by a point P in space. As shown in Figure 2.2b, if there is a plane quadrilateral source element lying in the $\xi\eta$-

plane (element coordinate system), the source density of this panel Q can be written as $\sigma(Q)$. The number of panels on the body, free and control surface can be denoted as N_b, N_f and N_c respectively. As mentioned before, the reference coordinate system is expressed as $O-XYZ$, the element system $O'-\xi\eta\zeta$ is established with O' on the geometry centroid and ζ axis on its normal vector.

The source of the element at general point $P(x,y,z)$ will induce the velocity components. The potential at point P is

$$\varphi_{Q,P} = \sigma(Q) \iint_Q G_{Q,P} d\xi d\eta \tag{2.36}$$

As the source density on panel Q remains constant, the velocity component at point P can be formulated based on the body surface boundary condition as

$$\frac{\partial \varphi_{Q,P}}{\partial \xi} = \sigma(Q) \iint_Q \frac{\partial G_{Q,P}}{\partial \xi} d\xi d\eta \tag{2.37}$$

$$\frac{\partial \varphi_{Q,P}}{\partial \eta} = \sigma(Q) \iint_Q \frac{\partial G_{Q,P}}{\partial \eta} d\xi d\eta \tag{2.38}$$

$$\frac{\partial \varphi_{Q,P}}{\partial \zeta} = \sigma(Q) \iint_Q \frac{\partial G_{Q,P}}{\partial \zeta} d\xi d\eta \tag{2.39}$$

The accurate solution of Eq. (2.37) to Eq. (2.39) can be found in the research of Hess and Smith (1964):

$$\begin{aligned} \frac{\partial \varphi_{Q,P}}{\partial \xi} = \sigma(Q) \Bigg[& \frac{\eta_2 - \eta_1}{l_{12}} \log\left(\frac{r_1 + r_2 - l_{12}}{r_1 + r_2 + l_{12}}\right) + \frac{\eta_3 - \eta_2}{l_{23}} \log\left(\frac{r_2 + r_3 - l_{23}}{r_2 + r_3 + l_{23}}\right) \\ & + \frac{\eta_4 - \eta_3}{l_{34}} \log\left(\frac{r_3 + r_4 - l_{34}}{r_3 + r_4 + l_{34}}\right) + \frac{\eta_1 - \eta_4}{l_{41}} \log\left(\frac{r_4 + r_1 - l_{41}}{r_4 + r_1 + l_{41}}\right) \Bigg] \end{aligned} \tag{2.40}$$

$$\frac{\partial \varphi_{Q,P}}{\partial \eta} = -\sigma(Q)\left[\frac{\xi_2-\xi_1}{l_{12}}\log\left(\frac{r_1+r_2-l_{12}}{r_1+r_2+l_{12}}\right)+\frac{\xi_3-\xi_2}{l_{23}}\log\left(\frac{r_2+r_3-l_{23}}{r_2+r_3+l_{23}}\right)\right.$$
$$\left.+\frac{\xi_4-\xi_3}{l_{34}}\log\left(\frac{r_3+r_4-l_{34}}{r_3+r_4+l_{34}}\right)+\frac{\xi_1-\xi_4}{l_{41}}\log\left(\frac{r_4+r_1-l_{41}}{r_4+r_1+l_{41}}\right)\right] \tag{2.41}$$

$$\begin{aligned}\frac{\partial \varphi_{Q,P}}{\partial \zeta} = \sigma(Q)\Bigg[&\arctan\left(\frac{m_{12}e_1-h_1}{zr_1}\right)-\arctan\left(\frac{m_{12}e_2-h_2}{zr_2}\right)\\&+\arctan\left(\frac{m_{23}e_2-h_2}{zr_2}\right)-\arctan\left(\frac{m_{23}e_3-h_3}{zr_3}\right)\\&+\arctan\left(\frac{m_{34}e_3-h_3}{zr_3}\right)-\arctan\left(\frac{m_{34}e_4-h_4}{zr_4}\right)\\&+\arctan\left(\frac{m_{41}e_4-h_4}{zr_4}\right)-\arctan\left(\frac{m_{41}e_4-h_1}{zr_1}\right)\Bigg]\end{aligned} \tag{2.42}$$

where

$$\begin{aligned}l_{12} &= \sqrt{(\xi_2-\xi_1)^2+(\eta_2-\eta_1)^2}\\ l_{23} &= \sqrt{(\xi_3-\xi_2)^2+(\eta_3-\eta_2)^2}\\ l_{34} &= \sqrt{(\xi_4-\xi_3)^2+(\eta_4-\eta_3)^2}\\ l_{41} &= \sqrt{(\xi_1-\xi_4)^2+(\eta_1-\eta_4)^2}\end{aligned} \tag{2.43}$$

where

$$\begin{aligned}\mathrm{m}_{12} = \tfrac{\eta_2-\eta_1}{\xi_2-\xi_1} \qquad \mathrm{m}_{23} = \tfrac{\eta_3-\eta_2}{\xi_3-\xi_2}\\ \mathrm{m}_{34} = \tfrac{\eta_4-\eta_3}{\xi_4-\xi_3} \qquad \mathrm{m}_{41} = \tfrac{\eta_1-\eta_4}{\xi_1-\xi_4}\end{aligned} \tag{2.44}$$

and

$$r_k = \sqrt{(x-\xi_k)^2+(y-\eta_k)^2+z^2} \quad , k = 1,2,3,4 \tag{2.45}$$

$$e_k = z^2+(x-\xi_k)^2 \quad , k = 1,2,3,4 \tag{2.46}$$

$$h_k = (y - \eta_k)(x - \xi_k) \quad , k = 1, 2, 3, 4 \tag{2.47}$$

So the velocity potential $\varphi_{Q,P}$ can be expressed as

$$\begin{aligned}\varphi_{Q,P} = \sigma(Q) \cdot \Bigg[& \sum_{i=1}^{3} \frac{(\eta_{i+1} - \eta_i)(x - \xi_i) - (\xi_{i+1} - \xi_i)(y - \eta_i)}{l_{i,i+1}} \times \log \frac{r_i + r_{i+1} - l_{i,i+1}}{r_i + r_{i+1} + l_{i,i+1}} \\ & + \frac{(\eta_1 - \eta_4)(x - \xi_4) - (\xi_1 - \xi_4)(y - \eta_4)}{l_{4,1}} \times \log \frac{r_4 + r_1 - l_{4,1}}{r_4 + r_1 + l_{4,1}} \Bigg] \\ & + z \cdot \frac{\partial \varphi_{Q,P}}{\partial \zeta}\end{aligned} \tag{2.48}$$

It should be mentioned the second partial derivative of φ is also required in Eq. (2.11), so the relevant formulae are as follows:

$$\frac{\partial^2 \varphi_{Q,P}}{\partial \xi^2} = 2\sigma(Q) \cdot \left[\sum_{i=1}^{3} \frac{(\eta_{i+1} - \eta_i)(r_i + r_{i+1})}{r_i r_{i+1} \left[(r_i + r_{i+1})^2 - l_{i,i+1}^2 \right]} + \frac{(\eta_1 - \eta_4)(r_1 + r_4)}{r_1 r_4 \left[(r_1 + r_4)^2 - l_{1,4}^2 \right]} \right] \tag{2.49}$$

$$\frac{\partial^2 \varphi_{Q,P}}{\partial \eta^2} = -2\sigma(Q) \cdot \left[\sum_{i=1}^{3} \frac{(\xi_{i+1} - \xi_i)(r_i + r_{i+1})}{r_i r_{i+1} \left[(r_i + r_{i+1})^2 - l_{i,i+1}^2 \right]} + \frac{(\xi_1 - \xi_4)(r_1 + r_4)}{r_1 r_4 \left[(r_1 + r_4)^2 - l_{1,4}^2 \right]} \right] \tag{2.50}$$

$$\begin{aligned}\frac{\partial^2 \varphi_{Q,P}}{\partial \varsigma^2} = 2\sigma(Q) \cdot \Bigg[& \sum_{i=1}^{3} \frac{\left[(\eta_{i+1} - \eta_i)(x - \xi_i) - (\xi_{i+1} - \xi_i)(y - \eta_i) \right](r_i + r_{i+1})}{r_i r_{i+1} \left[(r_i + r_{i+1})^2 - l_{i,i+1}^2 \right]} \\ & + \frac{\left[(\eta_1 - \eta_4)(x - \xi_4) - (\xi_1 - \xi_4)(y - \eta_4) \right](r_1 + r_4)}{r_1 r_4 \left[(r_1 + r_4)^2 - l_{1,4}^2 \right]} \Bigg]\end{aligned} \tag{2.51}$$

Another point to note is when the space point P approaches points on the panel Q that lie within the same $O' - \xi\eta$ plane, if P is in the quadrilateral, $\frac{\partial \varphi_{Q,P}}{\partial \xi} = 2\pi$, otherwise $\frac{\partial \varphi_{Q,P}}{\partial \xi} = 0$ (Hess and Smith, 1964).

Additionally, Eq. (2.36) to Eq. (2.51) are all based on the element coordinate system,

so a transformation matrix that can transfer all the points come back to the reference system is also necessary:

$$\begin{aligned} x' &= x_o + a_{11}x + a_{21}y + a_{31}z \\ y' &= y_o + a_{12}x + a_{22}y + a_{32}z \\ z' &= z_o + a_{13}x + a_{23}y + a_{33}z \end{aligned} \tag{2.52}$$

In this context, the entire computational domain boundary can be represented using a series of quadrilateral elements

$$S = \sum_{1}^{N_b} \Delta s_j + \sum_{1}^{N_f} \Delta s_j + \sum_{1}^{N_c} \Delta s_j \tag{2.53}$$

where N denotes the total number of panels on this surface, so if $\overrightarrow{\mathbf{X}}$ is the point on the boundary of the calculation domain, the potential at $\overrightarrow{\mathbf{X}}$ is

$$\varphi\left(\overrightarrow{\mathbf{X}}_i\right) = \sum_{j=1}^{N} \sigma_j \iint_{S_b+S_f+S_c} G\left(\overrightarrow{\mathbf{X}}_i, \overrightarrow{\xi}\right) dS_\xi = \sum_{j=1}^{N} \sigma_j G_{i,j}, i = 1, 2, \ldots, N \tag{2.54}$$

In the above equation, G_{ij} is the influence cofficient which can be derived from Eq. (2.48). Similarly, the remaining constituents within the boundary integral formulations for velocity and acceleration can be determined as

$$\frac{\partial \varphi}{\partial n}\left(\overrightarrow{\mathbf{x}}_i\right) = 2\pi\sigma_i + \sum_{\substack{j=1 \\ j\neq i}}^{N} \sigma_j \iint_{S_b+S_j+S_c} \frac{\partial}{\partial n_i} G\left(\overrightarrow{\mathbf{x}}_i, \vec{\xi}\right) dS_\xi = 2\pi\sigma_i + \sum_{\substack{j=1 \\ j\neq i}}^{N} \sigma_j G^n_{i,j}, i = 1, 2, \ldots, N \tag{2.55}$$

$$\frac{\partial \varphi}{\partial x}\left(\overrightarrow{\mathbf{x}}_i\right) = 2\pi\sigma_i + \sum_{\substack{j=1 \\ j\neq i}}^{N} \sigma_j \iint_{S_b+S_f+S_c} \frac{\partial}{\partial x_i} G\left(\overrightarrow{\mathbf{x}}_i, \vec{\xi}\right) dS_\xi = 2\pi\sigma_i + \sum_{\substack{j=1 \\ j\neq i}}^{N} \sigma_j G^x_{i,j}, i = 1, 2, \ldots, N \tag{2.56}$$

$$\frac{\partial \varphi}{\partial z}\left(\overrightarrow{\mathbf{x}}_i\right) = 2\pi\sigma_i + \sum_{\substack{j=1 \\ j\neq i}}^{N} \sigma_j \iint_{S_b+S_f+S_c} \frac{\partial}{\partial z_i} G\left(\overrightarrow{\mathbf{x}}_i, \vec{\xi}\right) dS_\xi = 2\pi\sigma_i + \sum_{\substack{j=1 \\ j\neq i}}^{N} \sigma_j G^z_{i,j}, i = 1, 2, \ldots, N \tag{2.57}$$

$$\frac{\partial^2 \varphi}{\partial x^2}\left(\overrightarrow{\mathbf{x}}_i\right) = \sum_{j=1}^{N} \sigma_j \iint_{S_b+S_f+S_c} \frac{\partial G\left(\overrightarrow{\mathbf{x}}_i, \vec{\xi}\right)}{\partial x_i^2} dS_\xi = \sum_{j=1}^{N} \sigma_j G^{\mathrm{xx}}_{i,j}, i = 1, 2, \ldots, N \tag{2.58}$$

where the influence coefficients $G^n_{i,j}$, $G^x_{i,j}$ and $G^z_{i,j}$ can be obtained by Eq. (2.40) - (2.42) and $G^{xx}_{i,j}$ can be given by Eq. (2.49) - (2.51).

Finally, upon substituting Eq.(2.54) through Eq.(2.58) into the body, free, and control surface boundary conditions, respectively, the equation system governing the solution for the source density σ will be established

$$[\mathbf{P}_{i,j}]\{\boldsymbol{\sigma}_j\} = [\mathbf{Q}_i], i = 1, 2, \ldots, N; j = 1, 2, \ldots, N \tag{2.59}$$

where $\mathbf{P}_{i,j}$ is the coefficient matrix while $\mathbf{Q}_i$ is a matrix composed of the boundary conditions for each panel. In most cases, $\mathbf{P}_{i,j}$ is a matrix with full rank, signifying that the source density σ_j for each panel can be resolved using a standard matrix-solving technique, such as Gaussian Elimination.

2.4 Hydrodynamic forces calculation

Since the source density σ_j of each panel is obtained, it should be easy to calculate hydrodynamic forces applied on the ship hull and wave elevations on the free surface now. The hydrodynamic forces exerted on the ship hull can be computed by integrating the product of the fluid pressure on the body surface and the unit normal vector over the wetted surface of the ship. This is represented as:

$$F_i = \iint_{S_b} p n_i \, \mathrm{d}S, i = 1, 2, \cdots, 6 \tag{2.60}$$

where i represents the degree of freedom, and

$$n_i = \begin{cases} \boldsymbol{n}, & i = 1, 2, 3 \\ \boldsymbol{x} \times \boldsymbol{n}, & i = 4, 5, 6 \end{cases} \tag{2.61}$$

p is the pressure acting on each panel of body surface, it can be given by Bernoulli's equation

$$p = -\rho \left[\frac{\partial \varphi_u}{\partial t} - U \frac{\partial \varphi_u}{\partial x} + \frac{1}{2} \left(\nabla \varphi_u \right)^2 \right] \tag{2.62}$$

Similarly, the wave elevation on the free surface can be obtained by kinematic free surface boundary condition

$$\zeta = -\frac{1}{g} \left[\frac{\partial \varphi_u}{\partial t} - U \frac{\partial \varphi_u}{\partial x} + \frac{1}{2} \left(\nabla \varphi_u \right)^2 \right] \tag{2.63}$$

where g is the gravitational acceleration. It is worth noting that, in the methods mentioned thus far, the unsteady terms in the free surface conditions have been neglected, which prevents obtaining an accurate time derivative of the velocity potential φ_u. To address this issue, a kind of second order upwind difference scheme is employed in this thesis.

At the first time step

$$\frac{\partial \varphi_u}{\partial t} = 0 \tag{2.64}$$

At the second or third time step

$$\frac{\partial \varphi_u}{\partial t} = \frac{\varphi_u^2 - \varphi_u^1}{\Delta t} \tag{2.65}$$

At other time steps

$$\frac{\partial \varphi_u}{\partial t} = \frac{3\varphi_u^i - 4\varphi_u^{i-1} + \varphi_u^{i-2}}{2\Delta t} \tag{2.66}$$

where Δt is the length of each time step and i represents the current time step.

Chapter 3

The unsteady hydrodynamics of a trans-critically accelerating ship in shallow water

3.1 Introduction

In numerous previous studies, it has been shown that a ship manoeuvring in shallow water presents greater challenges due to increased hydrodynamic forces, loss of control, and higher energy consumption (Sun et al. 2013). Particularly, when ships accelerate in shallow water, the pronounced unsteady effects significantly impact their behaviour. Therefore, investigating the issues of wave resistance and wave interaction when ships accelerate in extremely shallow water would provide valuable insights for their manoeuvring.

When sailing in shallow water, vessels are affected by a hydrodynamic interaction between the hull and seabed. This interaction changes the wave pattern and increases ship resistance. The former is of particular interest because the so-called Kelvin wake depends on the combination of water depth and ship speed, expressed by the depth Froude number, $F_h{=}V/\sqrt{gh}$, where V is the ship speed, h is the water depth, and g is the gravitational acceleration. In very shallow water, the denominator of F_h is equal to the wave speed. The depth Froude number is therefore the ratio of the ship and

wave speeds.

If the critical value of the depth Froude number (F_h=1) is surpassed, for example, when a vessel advances over a change in the water depth shockwaves may be generated (Jiang et al. 2002). Under the aforementioned conditions, the vessel radiates large amplitude waves (Grue 2017). Upon passing over a reduction in water depth, the depth Froude number changes from a subcritical value (F_h<1) to a supercritical value (F_h>1). In shallow water hydrodynamics the water depth and/or the vessel speed may be manipulated to the same effect. Therefore, one may expect that similar phenomena can be reproduced by either changing the speed or changing the depth.

The key question addressed in the chapter is to investigate the phenomena occurring as a ship accelerated past the critical depth Froude number for a constant water depth. The present study compares Unsteady Reynolds Averaged Navier-Stokes results with 3D panel-based potential flow solutions using MHydro (Li et al. 2020), to address the aforementioned question.

The remainder of this chapter proceeds with some case studies and details of the numerical solver and potential flow method are given. Next, results focusing on the resistance characteristics are discussed, followed by conclusions.

3.2 Case study selection

The Wigley hull, with particulars shown in Table 3.1, is chosen to perform case studies. To the best of the authors' knowledge, no experimental campaign has studied a trans-critically accelerating ship in shallow water. Selecting the Wigley hull maximises the potential for other researchers to re-use the results presented here in their future studies because the hull is easily modelled mathematically and is frequently used for potential flow-based studies (Andrun et al. 2019; Bašić et al. 2020; Li et al. 2020; Yuan et al. 2014).

Table 3.1: Wigley hull principal dimensions.

Parameter	Symbol	Value	Units
Length	$\boldsymbol{L}$	3	m
Draft	$\boldsymbol{T}$	0.1875	m
Beam	$\boldsymbol{B}$	0.3	m
Displacement	$\boldsymbol{\nabla}$	0.076	m^3

The depth Froude number gives the parameters varied to produce a test matrix. Namely, the ship speed, V, and the water depth, d. Following Day et al. (2009) and Li et al. (2020) multiples of the gravitational acceleration are used to vary the ship speed. The aforementioned authors used values between $0.08g$ and $0.02g$, but their studies focused on a rapidly accelerating hull to a target speed and maintaining that speed. By contrast, the objective of the current study is observing transient phenomena during acceleration. For this reason, the maximum acceleration chosen in this research is $0.02g$, that is, the lowest acceleration intensity used by Day et al. (2009) and Li et al. (2020). Additionally, acceleration intensities equal to $0.01g$, $0.005g$, and $0.002g$ are used. These values are combined with depth-to-draft ratios of d/T=1.2, 1.5 to gauge the effect of water depth on the results. The test matrix is given in Table 3.2. Each case is allowed to develop up to and including a depth Froude number of 2. In addition to the accelerating case studies, steady, constant velocity cases were modelled using CFD to estimate the deviation between the fixed speed resistance and accelerating resistance. The depth Froude numbers modelled at constant velocities are also given in Table 3.2.

Table 3.2: Adopted case studies

Case number	Acceleration	Depth Froude number	d/T
1	$0.02g$	Variable	1.2
2	$0.01g$		
3	$0.005g$		
4	$0.002g$		
5	$0.02g$		1.5
6	$0.01g$		
7	$0.005g$		
8	$0.002g$		
9	0	0.6	1.2
10		0.8	
11		0.89	
12		0.95	
13		1	
14		1.05	
15		1.2	
16		1.4	
17		1.7	
18	0	0.6	1.5
19		0.8	
20		0.89	
21		0.95	
22		1	
23		1.05	
24		1.2	
25		1.4	
26		1.7	

3.3 Methods

The potential flow solver, MHydro (Yuan 2019), based on 3D boundary element method (BEM) by using a Rankine type Green function is introduced to study unsteady free surface effects. This solver has previously been used in the study of deep and shallow water ship hydrodynamics, for example, by Yuan (2019). In order to obtain the solution, it is necessary to correlate all results at each time step, so the unsteady terms in free-surface boundary conditions are preserved. These enable the simulation of unsteady effects on the free surface. The specific methodology is introduced in detail in the

following sections.

3.3.1 Description of the problem

As mentioned in Chapter 2, to describe the problem, two right-handed coordinate systems shown in Figure 3.1 are defined. As can be seen from that figure, the global coordinate system O-XYZ is fixed on the earth while the local coordinate system o_0-$x_0y_0z_0$ is fixed to the ship hull and moves forward with the ship. In both frameworks, the positive direction of the x-axis points to the ship bow, the positive direction of the y-axis points to the port side of the ship and the positive z-axis points to upward. The undisturbed calm-free surface is located at z=0.

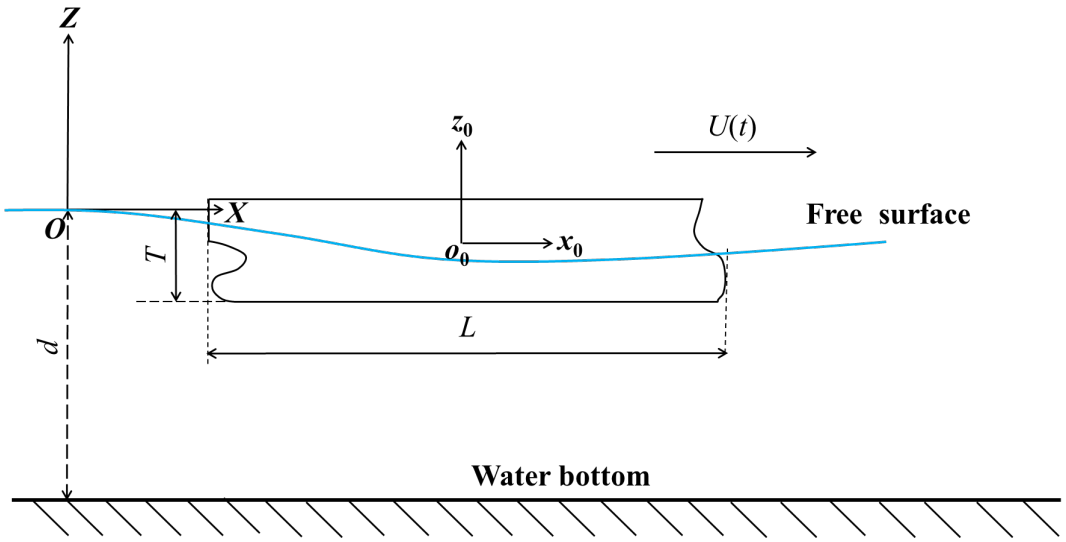

(a)

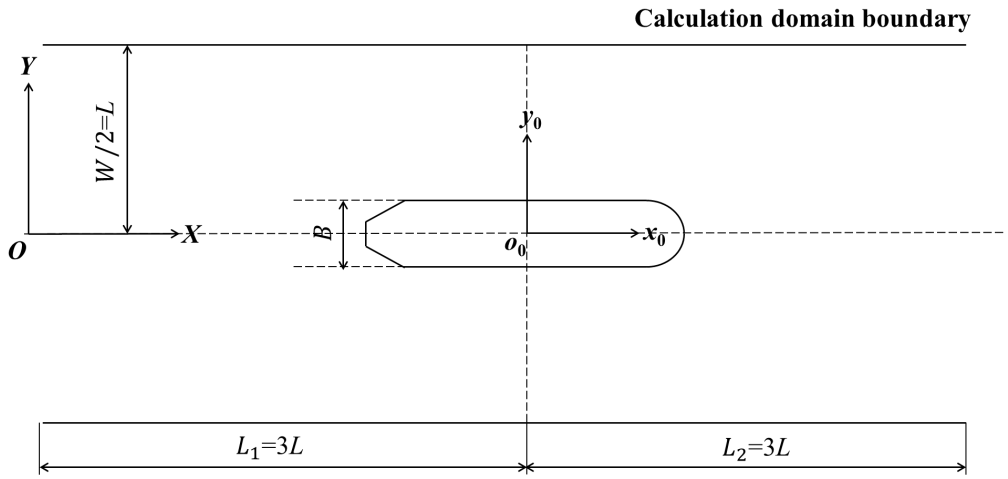

(b)

Figure 3.1: Sketch of the problem. In (a), L is the length of the ship and $U(t)$ is the ship velocity which is changing with time. T represents the draft of the ship while the water depth is denoted as d. (b) shows a top view of the problem, where it can be seen that the distance between the front and rear boundaries of the computational domain and the midship point are both $3L$. On the other hand, both the port and starboard boundaries are L away from the centreline of the ship. Finally, B in this figure represents the ship breadth.

3.3.2 Discretization of boundary conditions

In chapter 2, a linear, steady free surface condition was employed. However, the continuous acceleration problem of a ship in shallow water discussed in this chapter represents a typical unsteady problem. Therefore, the extension of the potential flow solver, MHydro, to address unsteady effects became a necessary undertaking.

The free surface conditions mentioned in Eq. (2.5) and Eq. (2.6) are fully implicit type whose solutions can be obtained iteratively. Firstly, since in this problem, unsteady effects will dominate over nonlinear effects, the nonlinear terms in the boundary conditions will be neglected, resulting in a linear unsteady free surface condition, as shown below:

$$\frac{\partial \zeta}{\partial t} - U\frac{\partial \zeta}{\partial x} - \frac{\partial \varphi_u}{\partial z} = 0, \text{ at } z = \zeta \tag{3.1}$$

$$\frac{\partial \varphi_u}{\partial t} - U\frac{\partial \varphi_u}{\partial x} + g\zeta + \frac{1}{2}\nabla\varphi_u \cdot \nabla\varphi_u = 0, \text{ at } z = \zeta \tag{3.2}$$

Since the boundary conditions have been obtained, the next step is to solve the resulting equations by discretizing them to each time step. When t=0, the ship accelerates from rest with a constant acceleration, therefore the initial value of φ_u and ζ are denoted as $\varphi_u^0 = 0$ and $\zeta^0 = 0$. When $t = \Delta t$, small ship speed is developed and the linear-steady Neumann-Kelvin problem in Eq. (2.11) is solved at this time step to obtain the φ_u^1 and ζ^1.

Next, in order to ensure that the free surface condition is interrelated at all time steps, the second-order upwind difference scheme mentioned in Eq. (2.64) - Eq. (2.66) is applied to the time and space derivatives of velocity potential φ_u and wave elevatrion ζ:

taking derivatives with respect to time,

$$\begin{aligned} (\varphi_t)_{i,j}^0 &= 0, \\ (\zeta_t)_{i,j}^0 &= 0 \end{aligned} \quad t = 0 \tag{3.3}$$

$$\begin{aligned} (\varphi_t)_{i,j}^1 &= \frac{\varphi_{i,j}^1 - \varphi_{i,j}^0}{\Delta t} \\ (\zeta_t)_{i,j}^1 &= \frac{\zeta_{i,j}^1 - \zeta_{i,j}^0}{\Delta t} \end{aligned} \quad t = \Delta t \tag{3.4}$$

$$\begin{aligned} (\varphi_t)_{i,j}^{m+1} &= \frac{1}{\Delta t}\left(\frac{3}{2}\varphi_{i,j}^{m+1} - 2\varphi_{i,j}^m + \frac{1}{2}\varphi_{i,j}^{m-1}\right) \\ (\zeta_t)_{i,j}^{m+1} &= \frac{1}{\Delta t}\left(\frac{3}{2}\zeta_{i,j}^{m+1} - 2\zeta_{i,j}^m + \frac{1}{2}\zeta_{i,j}^{m-1}\right) \end{aligned} \quad t > \Delta t \tag{3.5}$$

taking derivatives with respect to space,

$$\begin{aligned} (\varphi_x)_{i,j}^{m+1} &= \frac{\varphi_{i,j}^{m+1} - \varphi_{i,j-1}^{m+1}}{\Delta x} \\ (\zeta_x)_{i,j}^{m+1} &= \frac{\zeta_{i,j}^m - \zeta_{i,j-1}^{m+1}}{\Delta x} \end{aligned} \quad \text{on the J-th column} \tag{3.6}$$

$$\begin{aligned}(\varphi_x)_{i,j}^{m+1} &= \frac{\varphi_{i,j}^{m+1} - \varphi_{i,j+1}^{m+1}}{\Delta x} \\ (\zeta_x)_{i,j}^{m+1} &= \frac{\zeta_{i,j}^{m+1} - \zeta_{i,j+1}^{m+1}}{\Delta x}\end{aligned} \quad \text{on the (J-1)-th column} \tag{3.7}$$

$$\begin{aligned}(\varphi_x)_{i,j}^{m+1} &= \frac{1}{\Delta x}\left(\frac{3}{2}\varphi_{i,j}^{m+1} - 2\varphi_{i,j+1}^{m+1} + \frac{1}{2}\varphi_{i,j+2}^{m+1}\right) \\ (\zeta_x)_{i,j}^{m+1} &= \frac{1}{\Delta x}\left(\frac{3}{2}\zeta_{i,j}^{m+1} - 2\zeta_{i,j+1}^{m+1} + \frac{1}{2}\zeta_{i,j+2}^{m+1}\right)\end{aligned} \quad \text{on other columns} \tag{3.8}$$

where m represents the m-th time step and i and j indicate the location of the cell on the free surface. In this case, each panel line consists of a total of J columns.

Then substituting the Eq. (3.3) to Eq. (3.8) into the kinematic free surface condition, allows one to obtain the value of $(\zeta)_{i,j}^{m+1}$:

$$\frac{1}{\Delta t}\left(\frac{3}{2}\zeta_{i,j}^{m+1} - 2\zeta_{i,j}^{m} + \frac{1}{2}\zeta_{i,j}^{m-1}\right) - U\frac{1}{\Delta x}\left(\frac{3}{2}\zeta_{i,j}^{m+1} - 2\zeta_{i,j+1}^{m+1} + \frac{1}{2}\zeta_{i,j+2}^{m+1}\right) - \frac{\partial\varphi_{i,j}^{m+1}}{\partial z} = 0 \tag{3.9}$$

$$\frac{3}{2}\left(\frac{1}{\Delta t} - \frac{U}{\Delta x}\right)\zeta_{i,j}^{m+1} + 2\frac{U}{\Delta x}\zeta_{i,j+1}^{m+1} - \frac{1}{2}\frac{U}{\Delta x}\zeta_{i,j+2}^{m+1} = \frac{2}{\Delta t}\zeta_{i,j}^{m} - \frac{1}{2}\frac{1}{\Delta t}\zeta_{i,j}^{m-1} + \frac{\partial\varphi_{i,j}^{m+1}}{\partial z} \tag{3.10}$$

Therefore, the following matrix will be created to obtain the wave elevations on the free surface at the current time step.

$$[\mathbf{A}_{i,j}]\left\{\boldsymbol{\zeta}_j^{m+1}\right\} = [\mathbf{B}_j], i = 1, 2, \ldots, N; j = 1, 2, \ldots, N \tag{3.11}$$

where $[\mathbf{A}_{i,j}]$ is the coefficient matrix, $\left\{\boldsymbol{\zeta}_j^{m+1}\right\}$ is the wave elevations at (m+1)-th time step and $[\mathbf{B}_j]$ is the right-hand side of the equations in the system:

$$[\mathbf{A}_{i,j}] = \begin{bmatrix} \frac{3}{2}\left(\frac{1}{\Delta t} - \frac{U}{\Delta x}\right) & 2\frac{U}{\Delta x} & -\frac{1}{2}\frac{U}{\Delta x} & 0 & \cdots & 0 \\ 0 & \frac{3}{2}\left(\frac{1}{\Delta t} - \frac{U}{\Delta x}\right) & 2\frac{U}{\Delta x} & -\frac{1}{2}\frac{U}{\Delta x} & \cdots & 0 \\ \vdots & & \ddots & & & \vdots \\ \vdots & & & \ddots & & \vdots \\ 0 & \cdots & \cdots & \cdots & \frac{3}{2}\frac{1}{\Delta t} - \frac{U}{\Delta x} & \frac{U}{\Delta x} \\ 0 & \cdots & \cdots & \cdots & \frac{3}{2}\frac{1}{\Delta t} + \frac{U}{\Delta x} & -\frac{U}{\Delta x} \end{bmatrix} \tag{3.12}$$

$$\left\{\boldsymbol{\zeta}_j^{m+1}\right\} = \begin{bmatrix} \zeta_{i,j}^{m+1} \\ \zeta_{i,j+1}^{m+1} \\ \zeta_{i,j+2}^{m+1} \\ \vdots \\ \zeta_{i,J}^{m+1} \end{bmatrix} \tag{3.13}$$

$$[\mathbf{B}_j] = \begin{bmatrix} \frac{2}{\Delta t}\zeta_{i,j}^{m} - \frac{1}{2}\frac{1}{\Delta t}\zeta_{i,j}^{m-1} + \frac{\partial \varphi_{i,j}^{m+1}}{\partial z} \\ \frac{2}{\Delta t}\zeta_{i,j+1}^{m} - \frac{1}{2}\frac{1}{\Delta t}\zeta_{i,j+1}^{m-1} + \frac{\partial \varphi_{i,j+1}^{m+1}}{\partial z} \\ \vdots \\ \frac{2}{\Delta t}\zeta_{i,J}^{m} - \frac{1}{2}\frac{1}{\Delta t}\zeta_{i,J}^{m-1} + \frac{\partial \varphi_{i,J}^{m+1}}{\partial z} \end{bmatrix} \tag{3.14}$$

Then, all variables in the dynamic free-surface condition can be updated with the results obtained and it can be solved by Eq. (2.59):

$$\frac{1}{\Delta t}\left(\frac{3}{2}\varphi_{i,j}^{m+1} - 2\varphi_{i,j}^{m} + \frac{1}{2}\varphi_{i,j}^{m-1}\right) - U\frac{\partial \varphi_{i,j}^{m+1}}{\partial x} + g\zeta_{i,j}^{m+1} = 0 \tag{3.15}$$

$$\frac{3}{2}\frac{1}{\Delta t}\varphi_{i,j}^{m+1} - U\frac{\partial \varphi_{i,j}^{m+1}}{\partial x} = \frac{2}{\Delta t}\varphi_{i,j}^{m} - \frac{1}{2}\frac{1}{\Delta t}\varphi_{i,j}^{m-1} - g\zeta_{i,j}^{m+1} \tag{3.16}$$

In the above process, as the number of iterations k increases, all variables will be continuously updated until both $\left|\varphi_{i,j}^{m+1,k} - \varphi_{i,j}^{m+1,k-1}\right| < \varepsilon$ and $\left|\zeta_{i,j}^{m+1,k} - \zeta_{i,j}^{m+1,k-1}\right| < \varepsilon$ are satisfied.

Different from the method used by Pinkster (2004), this research does not decompose the hydrodynamic forces in Eq. (2.62) to extract separate added mass forces. Instead,

the velocity potential φ_u is directly solved to obtain the unsteady hydrodynamic forces.

3.4 Results and discussion

This section includes the results from both MHydro and CFD simulations. The CFD results were simulated and provided by Dr. Terziev (2023) using STAR-CCM software. Three sets of resistance results are extracted from the CFD solution, consisting of the total resistance (R_T), frictional resistance (R_F), and pressure resistance (R_P). The latter components represent the normal and tangential components of the total, respectively. As such, the frictional resistance includes the effects of surface curvature, while the pressure resistance represents a combination of the viscous pressure resistance and wave resistance (Molland et al., 2017). The viscous pressure resistance typically attains a small portion of the total at all speeds (Terziev et al., 2021a).

On the other hand, the potential flow theory used to compare results provides wave-making resistance. Since viscous pressure resistance is small, the results from the potential flow method and URANS method are compared directly. Splitting the viscous pressure resistance from the pressure resistance would require so-called double body numerical simulations, where the water surface is replaced by a rigid symmetry plane. However, since the free surface deforms considerably near the critical depth Froude number, double body simulations will not provide an adequate estimate of the viscous pressure resistance. In light of these facts, the numerically obtained pressure resistance is compared directly with the wave resistance calculated using the potential flow approach.

Another thing should be mentioned here is, throughout the simulation process, the most time-consuming cases took STAR-CCM approximately 30000 CPU hours to complete while it takes MHydro about half of that tine to complete the simulation of the same case. Due to the very low initial speed of the ship in this particular case and the fully unsteady method requires MHydro to strictly control the time step length, the time improvement of MHydro over the CFD method isn't notably significant in this case.

3.4.1 Pressure and wave resistance

This section compares wave and pressure resistance during ship acceleration for two depth-to-draft ratios. Figure 3.2 compares CFD and MHydro results from Table 3.2, which includes constant velocity cases. All forces are normalized using ship mass force F_m Day et al. (2009). A peak near F_h=1 emerges due to fore and aft wave systems' interaction in steady conditions. In Figure 3.2, this interference peaks between F_h=1.05 and F_h=1.2, depending on dimensionless acceleration (a/g).

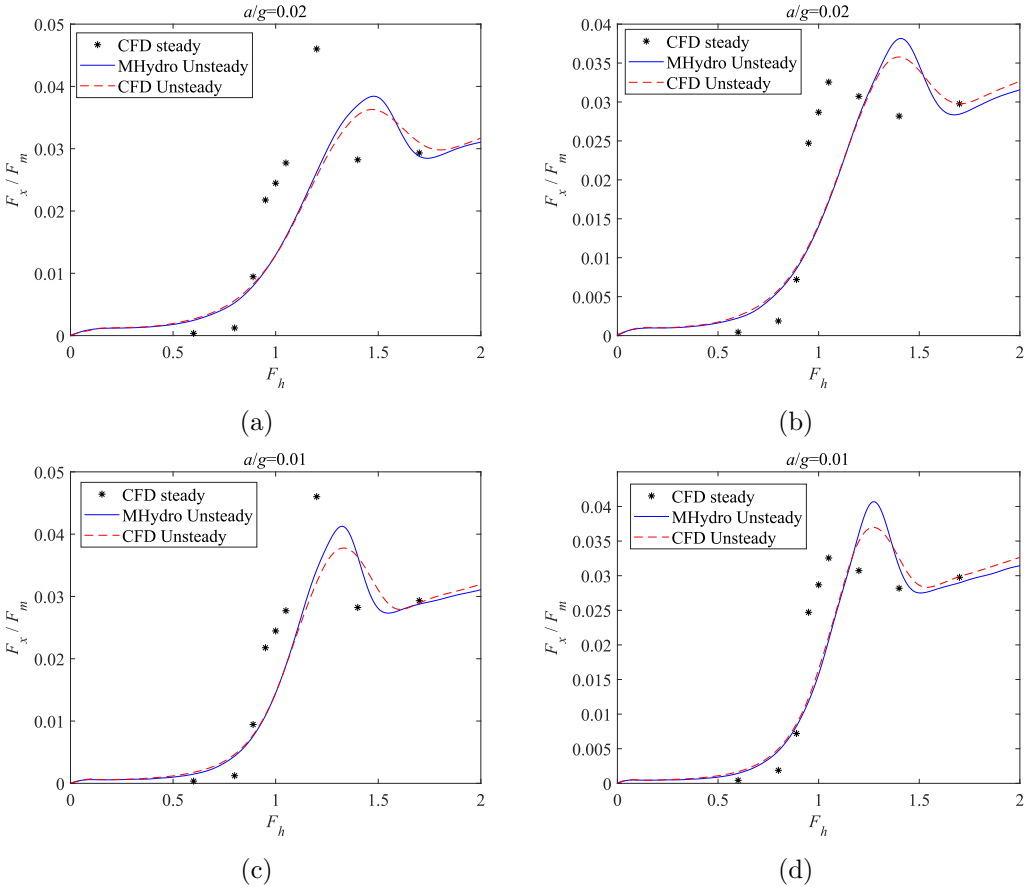

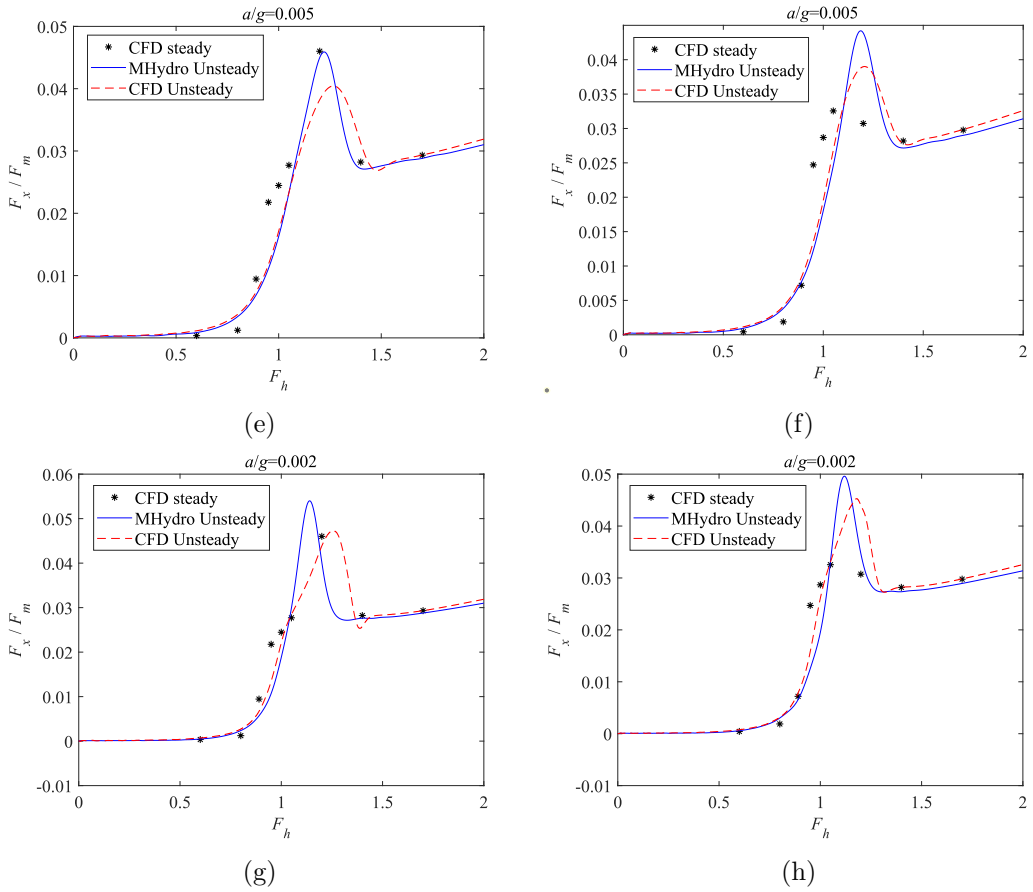

Figure 3.2: Changes of resistance during ship acceleration. The tiles on the left show d/T=1.2 while the tiles on the right show d/T=1.5.F_x/F_m (with F_m equals to mg) is the dimensionless wave resistance obtained by MHydro and pressure resistance obtained through the URANS method described previously. It also should be noted that the results of CFD here are pressure resistance while MHydro results are only wave making resistance.

It should be noted that because a limited number of points are selected for testing the constant speed case, the corresponding peak values shown in Figure will not necessarily indicate the exact peak since that curve can only provide an approximate range of where the peak value will appear. That increase in resistance is clearly influenced by the water depth, as evidenced by the higher F_x values when d/T=1.2 relative to d/T=1.5. This phenomenon changes when acceleration is added. In other words, the unsteady wave generated by the existence of acceleration has a significant impact on the resistance. The depth Froude number at which CFD-derived resistance peaks occur for d/T=1.2

decreases by 10.25% when the acceleration halves from a=0.02g to a=0.01g. A further halving of the acceleration to 0.005g reduces the F_h at which the resistance peak occurs by a further 5.13% relative to the 0.01g case. Reducing the acceleration further has a marginal effect of 0.94% in the depth Froude number. A similar monotonic decrease in the position of the peak is found when d/T=1.5, but the range reduces to 2.21% between a=0.005g and a=0.002g. In other words, at larger water depths, the position of the peak in resistance shows greater variation and sensitivity to acceleration than in very shallow waters.

The difference between the magnitude of the peaks predicted by CFD and MHydro is between 5.54% and 12.44% for d/T=1.2, and 6.23% and 11.75% for d/T=1.5. When the water depth corresponds to d/T=1.2, the difference between the two predictions grows by approximately 3% at each step between a=0.02g to a=0.005g. At a=0.002g, the disagreement between the two solvers peaks at 12.44%. In the case where d/T=1.5, that effect is only partially replicated. That is to say, the disagreement grows with decreasing acceleration, but this is only up to a=0.005g, where the discrepancy peaks at 11.75%. A further reduction in the acceleration decreases the difference by approximately 3%.

In terms of the disagreement in the position of the two peaks, the solvers predict remarkably close results for high accelerations. Interestingly, the difference between the predictions grows monotonically from 0.75% and 0.68% to 10.13% and 5.54% for d/T=1.2 and d/T=1.5, respectively. Further investigations are necessary to determine why the two sets of predictions performed better for the lowest acceleration when the water depth is slightly larger. Such an effect could be explained through the presence of non-linear effects, which are known to grow in importance with decreasing water depth, but such conclusions require more detailed investigations, preferably using experimental data to eliminate any bias in numerical or potential solutions.

When comparing the results obtained from MHydro and CFD, it can be concluded that no matter whether d/T=1.2 or d/T=1.5, the peak of results from MHydro will appear before the peak predicted by CFD, and the resistance value obtained from MHydro is always larger. The phenomenon is especially obvious when the acceleration is small. It is postulated that this difference arises due to viscous and nonlinear

terms. Nonlinear terms are ignored in MHydro, which means that MHydro provides a linear and unsteady result while the CFD results are nonlinear and unsteady. As the acceleration increases, the unsteady effect increases in relative importance, eclipsing nonlinear effects. Therefore, the unsteady effect occupies a dominant position when the acceleration is sufficiently large, which is why the results obtained from MHydro and CFD show less agreement when the acceleration is small. Conversely, the difference between the results obtained from the two prediction methods is smallest when the acceleration is large. The discussion above is also supported by observations made elsewhere regarding the linear potential flow solutions near the critical depth Froude number (Lea and Feldman, 1972; Tuck, 1978; Tuck and Taylor, 1970).

3.4.2 Acceleration effects

As stated previously, there are two main influencing factors in the problem examined herein: the magnitude of the acceleration and the water depth. These are discussed in turn.

It can be seen from Figure 3.3 that after the introduction of acceleration, both the peak value of the resistance and the position where this peak appears change. Having established good agreement between CFD and MHydro, additional case studies are explored in Figure 3.3 with the potential flow solver only due to its faster turnaround time and lesser computational requirements. Figure 3.3 also shows that the greater the acceleration, the smaller the resistance peak and the later it appears along the examined depth Froude number range. It can therefore be concluded that the unsteady effect induced by the acceleration has a significant influence on the results. The shifting in position of the peak in resistance can be explained by the shock wave at the bow caused by the acceleration. In the initial stages when the ship speed is low a shock wave will be emitted forward causing additional wave/pressure resistance. As the speed of the ship increases to the same speed as the wave, the wave making resistance reaches a maximum. This phenomenon appears as the peak in Figure 3.2.

In other words, as the acceleration increases, the velocity of the resulting shock wave also increases, so the ship speed must be higher before the shockwave can be overtaken.

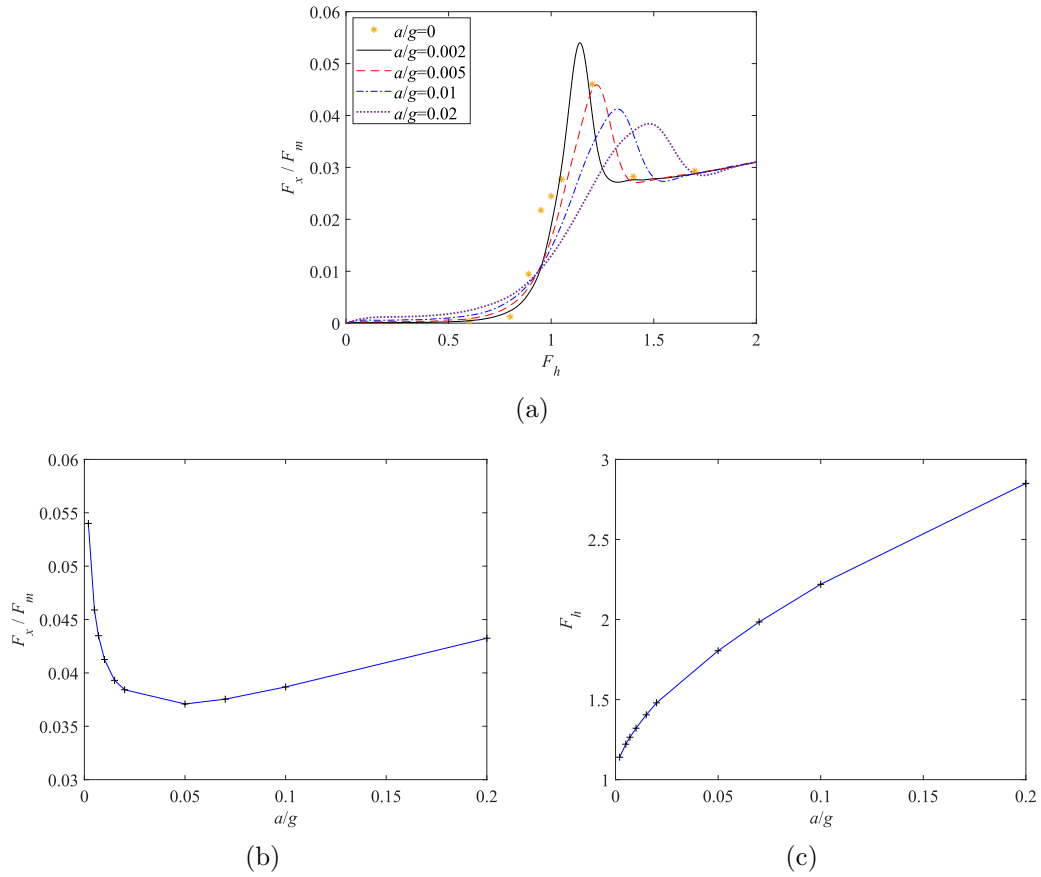

Figure 3.3: (a) Changes of fully-unsteady resistance with varying acceleration; (b) Resistance peak value for different accelerations; (c) Peak location at different acceleration; Cases depicted correspond to $d/T = 1.2$.

Thus, the position of the peak is delayed at higher accelerations. Following this, as the ship continues to accelerate, the shock wave will be overtaken by the ship, so the resistance drops sharply for a narrow band of F_h values, followed by a linear increase. Another observation on the results presented herein is that regardless of acceleration, the time-history of the resistance passes through a single point, located close to F_h=1. In all cases, the growth in resistance beyond that point is approximately linear until the peak of resistance is reached. These results are depicted in Figure 3.4a and Figure 3.4b (or Figure 3.4c and Figure 3.4d) for d/T=1.2 and d/T=1.5, respectively.

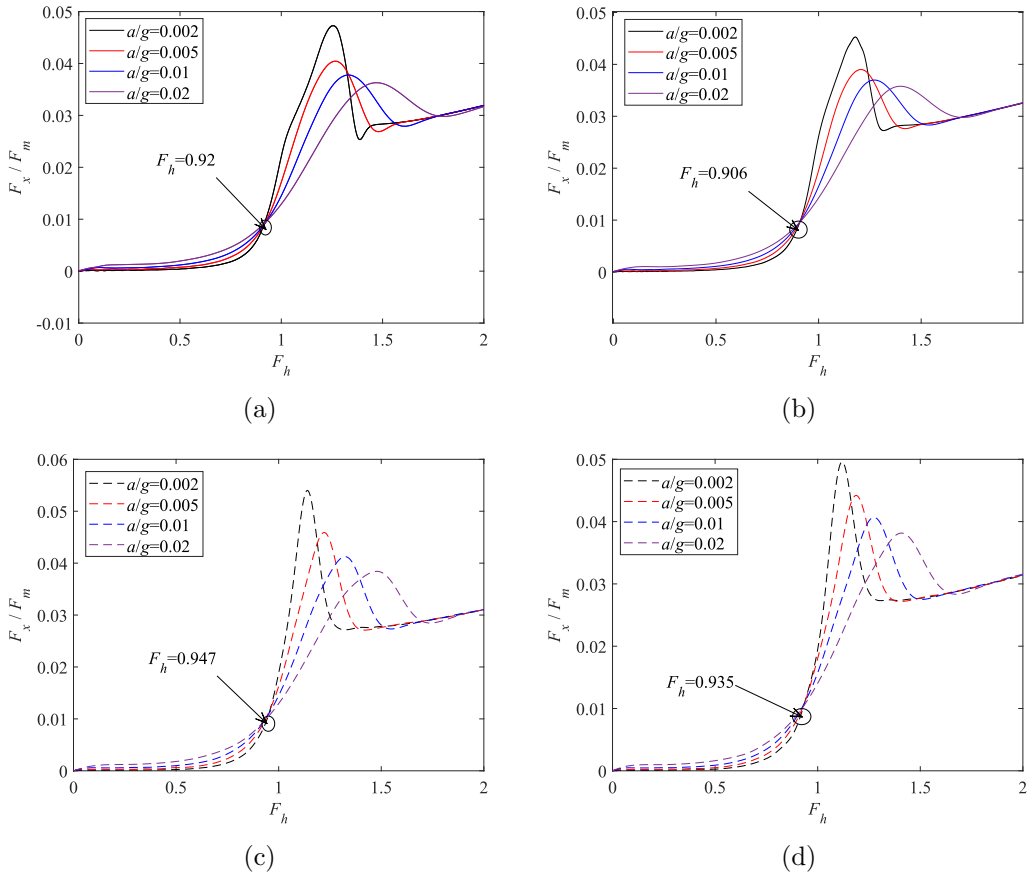

Figure 3.4: Resistance time-history for all acceleration intensities. (a) Resistance time-history at d/T=1.2 for CFD. (b) Resistance time-history at d/T=1.5 for CFD. (c) Resistance time-history at d/T=1.2 for MHydro. (d) Resistance time-history at d/T=1.5 for MHydro.

When the water depth corresponds to d/T=1.5, the CFD results show that resistance time-histories coincide at approximately F_h=0.906, while the potential flow results predict this point at about F_h=0.935. Similarly, when d/T=1.2, CFD predicts a shift in this point to approximately F_h=0.92, contrasting MHydro's estimation at around $F_h = 0.947$. Prior to and following the intersection point, resistance follows unique paths. To the best of the authors' knowledge, such phenomena have not been shown in the existing literature. In order to study the cause of this phenomenon, wave fields around the ship are shown in Figure 3.5.

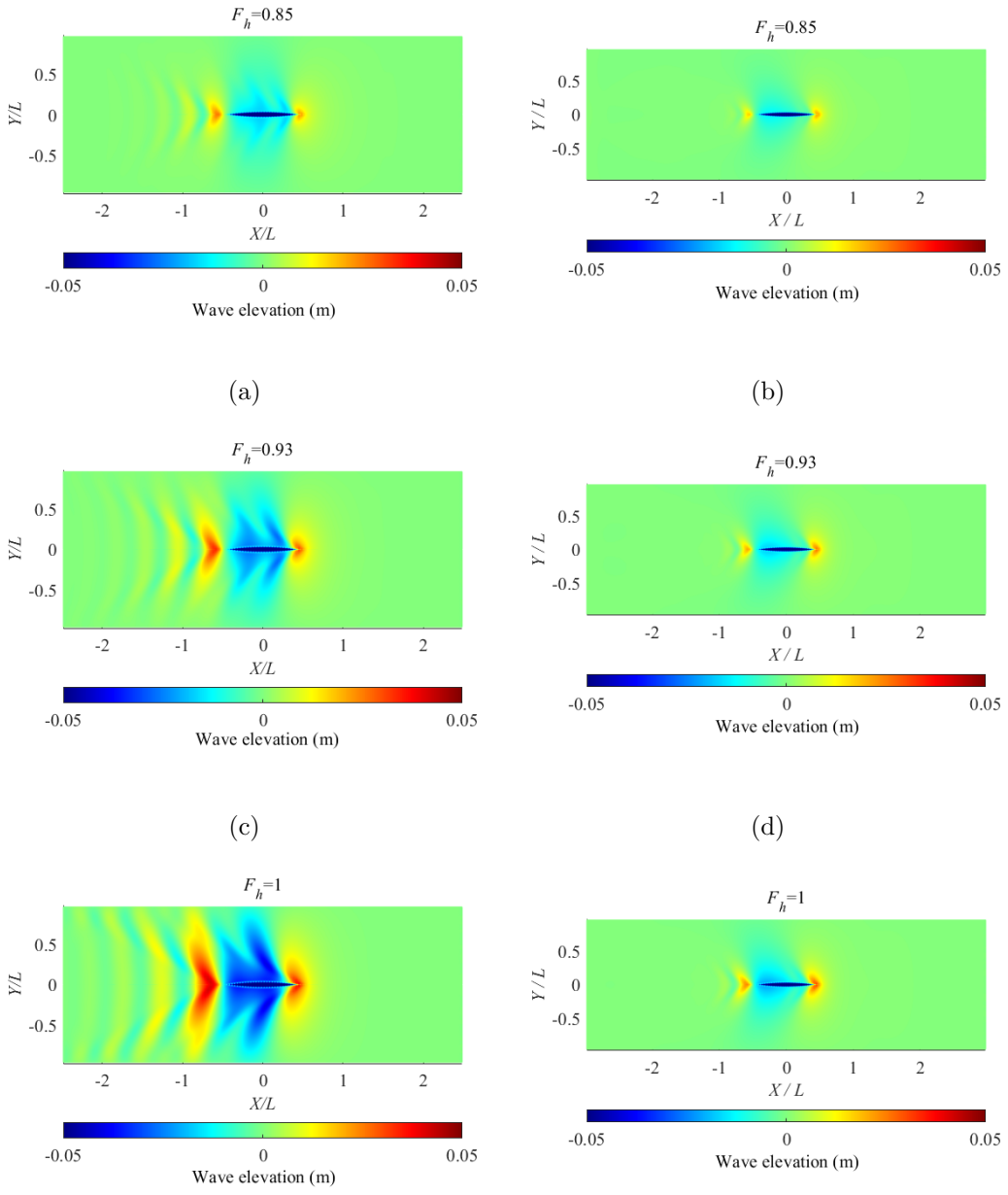

Figure 3.5: Wave fields around the ship with different accelerations where the left figures correspond to an acceleration of $0.002g$, while the right figures correspond to $a = 0.02g$. These results were computed using MHydro for d/T=1.2.

When F_h or the acceleration is different, wave elevations at the bow and stern also

change accordingly. It can also be observed that when the acceleration is lower, the wave field around the ship is more pronounced. This is due to the fact that with lower acceleration, the ship requires more time to accelerate to the same velocity. In other words, this is the result of a cumulative acceleration effect.

A more evident depiction is visible in Figure 3.6. It can be seen the wave at the bow is mainly determined by the velocity of the ship, while the condition is different for waves at the stern. It is precisely this difference in the bow-stern wave field that leads to the observed intersection point of resistance in Figure 3.4.

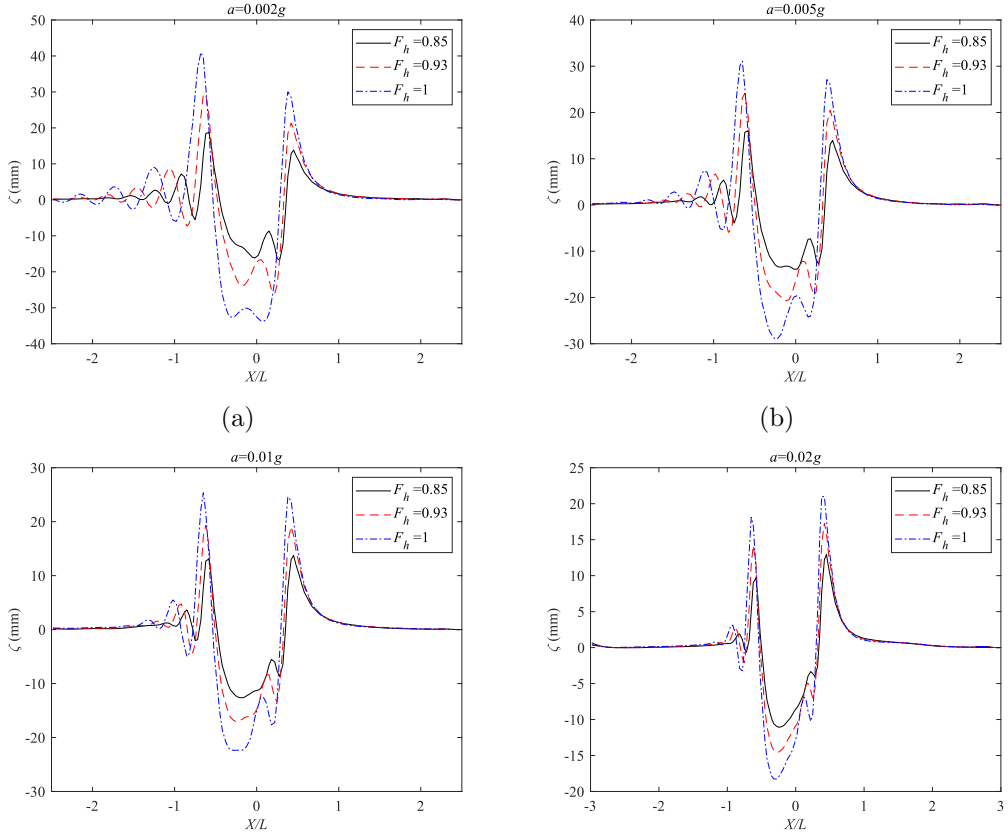

Figure 3.6: Wave elevations on the port side of ship with different accelerations (y/L=0.0167). These results were computed using MHydro for d/T=1.2.

As shown in Figure 3.7a, the wave elevation at the ship stern is inversely proportional to the acceleration. A greater acceleration will bring more pronounced unsteady effects, and when superimposed on the original wave field at the ship stern, results in smaller

wave peaks and troughs. It should also be mentioned that the waves at the ship stern show peaks before the critical speed and troughs after it. This means that when F_h <1, the smaller the acceleration, the closer the wave elevation at the bow and stern, and the less the wave resistance. However, after this point, as the acceleration decreases, the wave trough at the stern will increase significantly. According to Bernoulli's equation, the pressure field at the stern of the ship will also decrease, resulting in greater wave resistance. This is also why the peak value of the resistance decreases with an increase in acceleration.

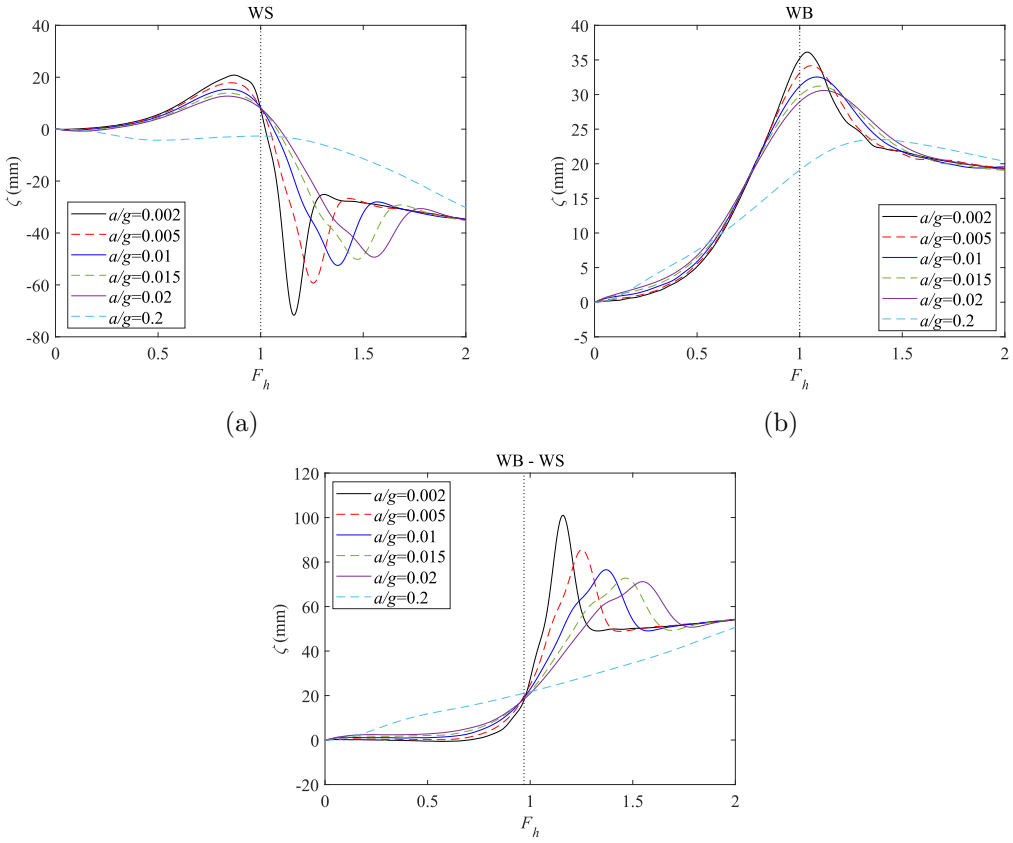

Figure 3.7: Wave elevations around the ship stern and bow with different accelerations. (a) Stern wave (WS); (b) Bow wave (WB); (c) Wave difference between ship bow and stern. These results were computed using MHydro for d/T=1.2.

3.4.3 Finite depth effects

As evidenced by the agreement between the constant speed and accelerating results shown in Figure 3.2g, the effect of acceleration at a=0.002g and d/T=1.2 is weak. However, there is a significant difference between the corresponding values at $d/T = 1.5$. The aforementioned observation, in conjunction with the fact that the peak shifts along the F_h range with varying acceleration indicates that the depth Froude number is not the best parameter to represent the time-varying velocity.

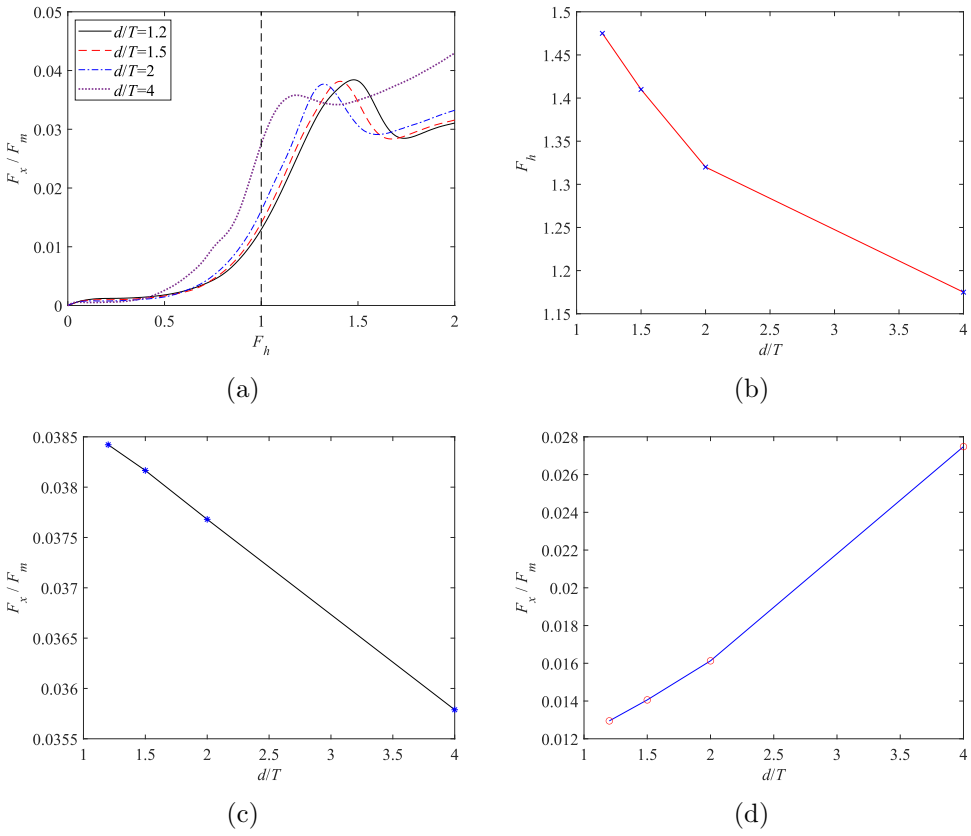

Figure 3.8: Wave resistance and associated peaks at different water depths, computed using MHydro; (a) shows the time-history of the resistance, (b) shows the position of the peak as a function of d/T, (c) shows the magnitude of the peak for varying d/T ratios while (d) shows the resistance value at F_h=1.

Figure 3.8 shows a set of example cases with a/g=0.02 for d/T=1.2-4 computed with MHydro. Under this framework, larger depth-to-draft ratios push the peak towards higher F_h values and reduce its magnitude. That effect is most perceptible between

d/T=2 and d/T=4. The resistance penalty induced as a shallow water effect at higher F_h decreases rapidly with increasing water depth. If the water depth were increased beyond d/T=4, the characteristic peak of resistance observed in shallow waters would vanish.

A second observation from Figure 3.8 is that shallow water may be advantageous in terms of reduced resistance when accelerating a vessel. Specifically, the values depicted for F_h=1 in Figure 3.8d demonstrate that the higher the water depth, the higher the resistance. For the given acceleration, the increase in resistance between very shallow water (d/T=1.2) and moderately shallow water (d/T=4) is more than 100%. That is a consequence of the delay in the appearance of the resistance peak to higher depth Froude numbers as shown in Figure 3.8c.

As seen in Figure 3.9c, when the water depth is shallower, there is a greater peak in wave-making resistance. This is easily understandable because as the water depth decreases, the shallow water effect becomes more pronounced. In contrast, Figure 3.9d indicates that, at a constant acceleration, shallower water depth corresponds to higher a depth Froude number at the peak of wave-making resistance. However, as F_h inherently incorporates water depth, such a comparison isn't entirely equitable. This once again demonstrates that the depth Froude number F_h is not suitable for investigating the impact of water depth on resistance.

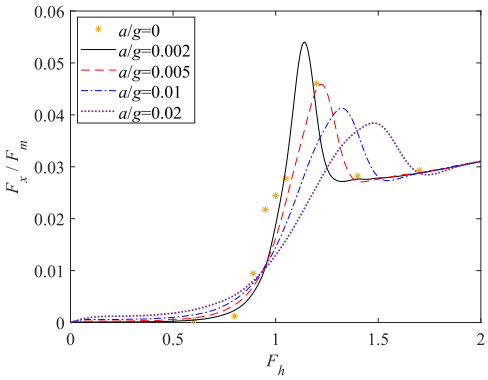

(a)

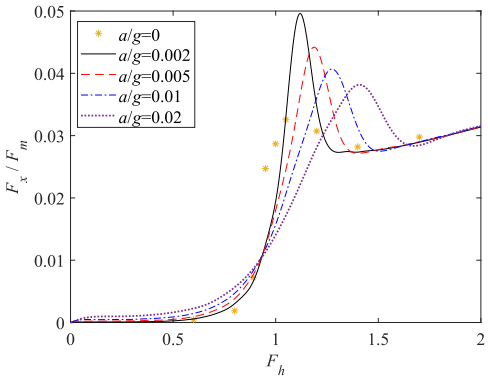

(b)

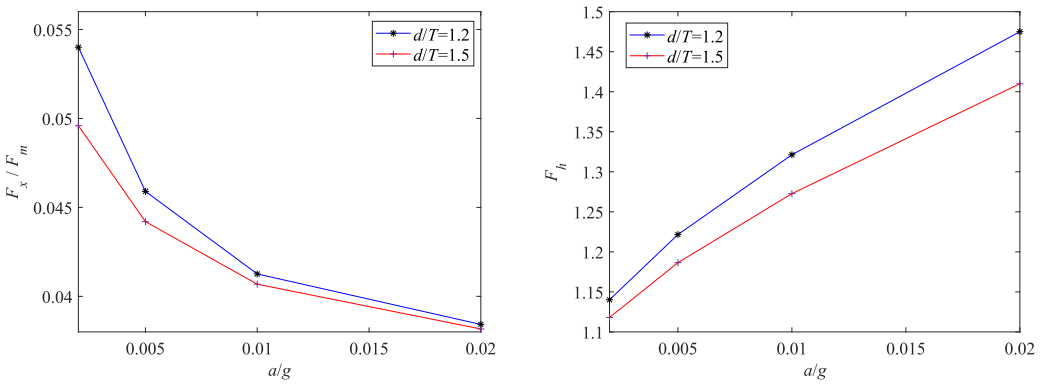

(c) (d)

Figure 3.9: Comparison of resistance values for different accelerations and water depths; (a) and (b) show d/T=1.2 and d/T=1.5, respectively; (c) and (d) show the magnitude of the resistance peak as a function of the acceleration and its position along the F_h range, respectively.

3.4.4 Unsteady free surface effects

The results by MHydro shown in the above sections are obtained by solving the fully unsteady Boundary Value Problem (BVP) defined in Eq. (2.4), Eq. (2.5) and Eq. (2.6). It would be interesting to investigate the effect of unsteadiness on free surface boundary condition. A quasi-steady solution in Eq. (2.11) is therefore proposed, in which the time dependent terms in Eq (2.5) and Eq. (2.6) are ignored at each time step. For both unsteady and quasi-steady methods, the unsteady Bernoulli's equation in Eq. (2.62) is used to calculate the hydrodynamic force, more specifically, the wave-making resistance in the present study.

Figure 3.10a shows a direct comparison of the results obtained from quasi-steady and unsteady free-surface solutions mentioned above. The discrepancies indicate the importance of the unsteady free-surface condition on the present acceleration problem. The free-surface effects are predominant at near critical speed region. Due to the unsteady nature of the acceleration problem, the unsteady terms on free-surface condition must be considered.

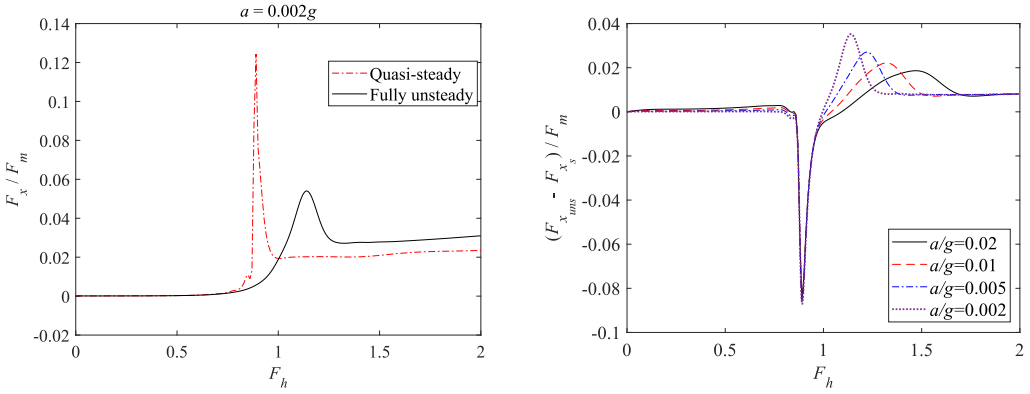

(a) (b)

Figure 3.10: Wave-making resistance obtained by MHydro. (a) MHydro results with and without considering the time-dependent terms on free-surface boundary condition; (b) the unsteady component in MHydro results.

The impact of unsteady effects on wave-making resistance is more evident in Figure 3.10b. It is observed that the influence of unsteadiness is minimal when the velocity is below the critical speed (F_h <1). However, near the critical speed, there is a significant increase in unsteady effects. Once the velocity exceeds the critical speed (F_h >1), the intensified unsteady effects, accompanied by increasing acceleration, lead to a balanced wave field around the ship hull, resulting in a reduction in wave-making resistance. This conclusion aligns with the earlier analysis presented in Figure 3.7.

3.5 Summary

A craft accelerating past the speed of the fundamental wave in a given medium experiences a fluctuation in resistance. To the best of the authors' knowledge, such effects had not previously been documented for the case of a steadily accelerating ship in shallow water, where the wave speed is a constant value which is a function of the gravitational acceleration and water depth only. The present study aimed to fill this gap in the literature by combining URANS and potential flow solutions.

Four acceleration intensities and two water depths were modelled using the Wigley parabolic hull. In all cases, a pronounced peak in the resistance was observed near the

critical depth Froude number. The results show a maximum disagreement in the prediction of the resistance peak's location along the examined depth Froude number between 5.54% and 12.44% for d/T=1.2, and 6.23% and 11.75% for d/T=1.5, respectively.

Results showed excellent agreement in the low and high-speed range, past the critical transition, indicating that the resistance in that range is linear and dominated by unsteady rather than nonlinear terms. Some deviation was found between the two solvers near the critical speed, which was interpreted as an indication that nonlinear effects influence the solution in that range. A point near but less than F_h=1 was identified for both water depths modelled where all acceleration intensities cross, creating an intersection point. The existence of this point was explained through the proximity of the trans-critical boundary and the fact that no steady flow is possible when the depth Froude number is unity.

Although this research has confidence in the results presented herein in view of the agreement between the two solvers, experimental data of trans-critically accelerating ship resistance would be invaluable in demonstrating the exact level of accuracy. In addition, models of trans-critical acceleration in fully confined water are of particular interest since the blockage ratio would also be an important parameter. Such cases are also interesting because the trans-critical range can occupy a significant portion of the depth Froude number depending on the blockage (Lataire et al., 2012a).

Chapter 4

Unsteady effects between passing and moored ships in shallow and confined water

4.1 Introduction

When ships manoeuvre in ports or channels, various hydrodynamic interactions occur, affecting ship behaviour. Examples include ship-bottom, ship-bank, ship-lock, and ship-ship interactions. Ship-ship interactions involve overtaking, encountering, and the effect of passing on moored ships. The passing ship effect excites the moored ship, which must transfer the forces to the quay mooring equipment without overloading it or causing excessive motion. Managing these interactions is crucial for safe and efficient ship operations.

Passing ship effects have attracted significant attention from the research and engineering community. Remery's (1974) groundbreaking work involved extensive physical scale model tests using two tanker models. In recent years, there has been notable progress in tools and knowledge within this field. Researchers have employed various methods to study ship-ship interactions, such as utilising existing scale model test databases, employing empirical models, employing numerical potential flow tools, and employing numerical RANS (Reynolds-Averaged Navier-Stokes) methods. Each

method has its own strengths and limitations and should be applied within its appropriate contexts.

Passing ship interactions in shallow and confined waterways are significant and require special consideration in calculation tools. Many existing tools do not fully account for the effects of channel confinement. For instance, physical scale model tests conducted in open sections and their derived empirical models, as well as numerical packages with fixed water surfaces, may not adequately capture these effects. To address this gap and provide an opportunity for the scientific community to validate their research tools, the Knowledge Centre for MANoeuvring in SHallow and CONfined water (MANSHOC) has published eight benchmark tests as part of the PESCA (Passing Effects in Shallow and Confined Areas) test program (Van Zwijnsvoorde et al., 2022). These benchmark tests serve as a means to assess and validate the performance of various tools in accurately simulating passing ship effects in shallow and confined waterways. Researchers can utilize these tests to enhance their understanding and refine their tools for such scenarios.

This research focuses specifically on the validation of unsteady effects using PESCA test data. One experiment from the benchmarking data effort (Van Zwijnsvoorde et al., 2022) is replicated by potential flow solver MHydro. Further details can be found in the MASHCON conference paper.

4.2 Methods

Theoretically, ship passing problem is an multi-body problem, in order to study the influence of ship-ship interactions in this problem, it is necessary to superimpose the motion of the two ships, lead to the wave field on the free surface.

4.2.1 Description of the problem

In this research, there are three coordinate systems (as shown in Figure 4.1). One is fixed on the ground as the reference coordinate system, the other two are fixes on the passing and moored ship as the local coordinate systems. The passing ship sails with

a constant forward speed U and gradually passes over the moored ship.

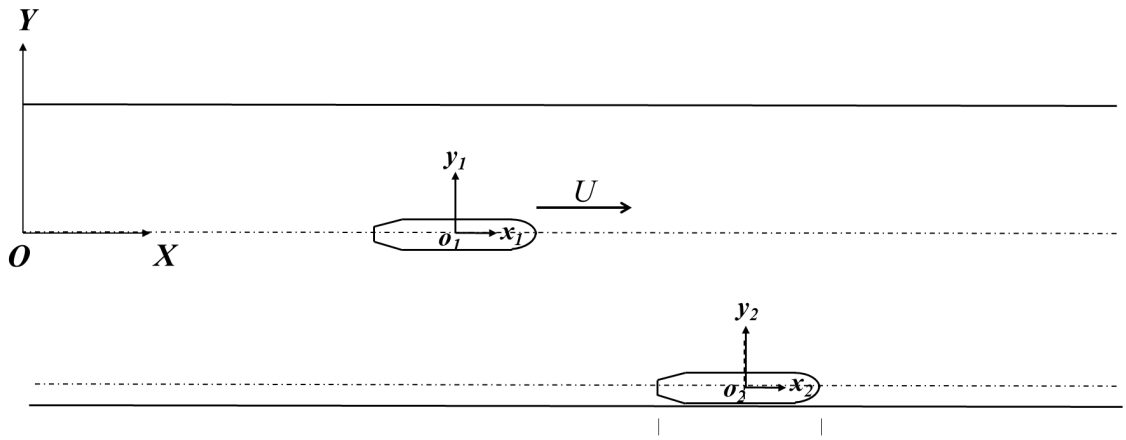

Figure 4.1: The coordinate system

4.2.2 Multi-ship interaction

As mentioned earlier, this chapter will involve separately calculating the wave field generated by each of the two ships and then superimposing them.

First, allow the passing ship to move while keeping the moored ship stationary. In this condition, there are two body surface condition, for the passing ship is the same as Eq. (2.4):

$$\frac{\partial \varphi_u}{\partial \boldsymbol{n}} = U n_1 \tag{4.1}$$

For the moored ship is the same as the mentioned control surface condition in Eq. (2.13):

$$\frac{\partial \varphi_u}{\partial \boldsymbol{n}} = 0 \tag{4.2}$$

Next, by applying Eq. (3.1)-Eq. (3.16), the source density σ_1 caused by the passing ship on the free water surface can be obtained.

In the second step, keep the passing ship stationary and allow the moored ship to move. It should be mentioned that the velocity of the moored ship is always 0. In this case, the boundary conditions for the passing ship is presented as Eq. (4.2) while the body surface condition of moored ship is expressed as Eq. (4.1). Then, once again, using

Eq. (3.1)-Eq. (3.16), the source density σ_2 caused by the moored ship will be solved. Finally, by adding the two source density together, it will be easy to obtain the total source density σ.

4.3 Research set-up

To verify the accuracy of this method, the simulation results were compared with the experimental results in the 6$^{\text{th}}$ International Conference on Ship Manoeuvring in Shallow and Confined Water (6$^{\text{th}}$ MASHCON). In the present study, the total length of the towing tank is 87.5 m. Its width is 7.0 m and this tank has a maximum water depth of 0.5 m.

In order to study the ship passing effect in the case of a congested channel, a bank was constructed spanning from 3m to 62.23m of the tank's length. At the same time, the value of water depth was also controlled at a low level to simulate the shallow water effect. The passing ship model (C04) selected here is KCS (Kriso Container Ship) while a Neo Panamax container was chosen as the moored ship model (C0P) which is moored along a quay. It should be mentioned that there is another moored ship (T0Y) which is moored along a jetty layout in the experiment. Nevertheless, the case of T0Y was not studied in this research since the influence of ship length has been researched detailedly and the jetty layout is difficult to model. The sketch of the problem can be seen in Figure 4.2:

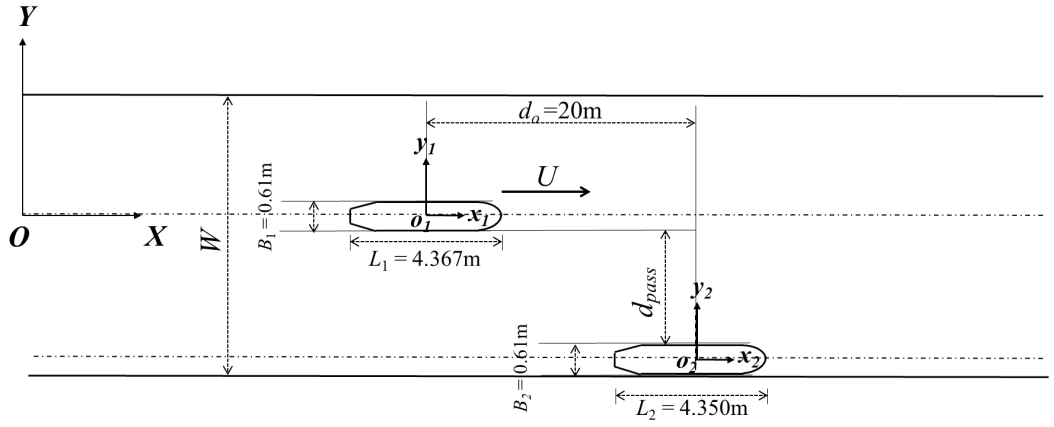

(a)

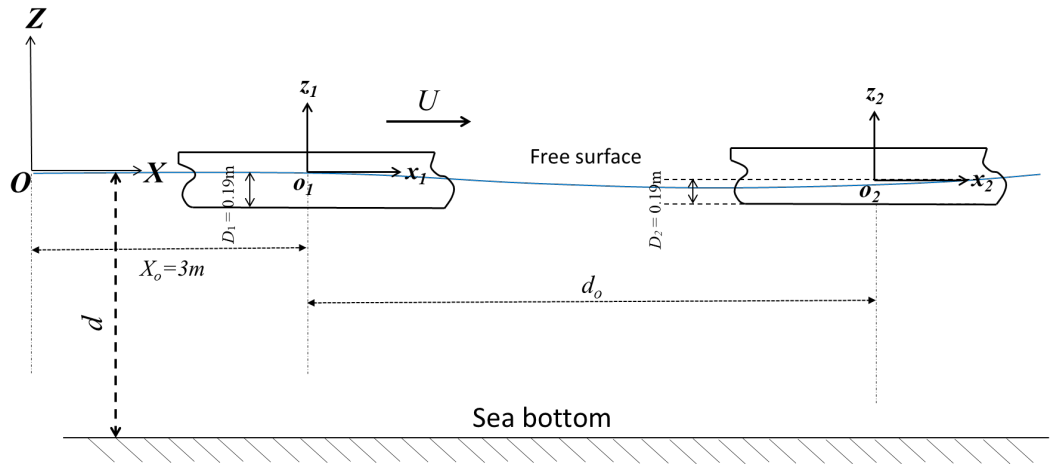

(b)

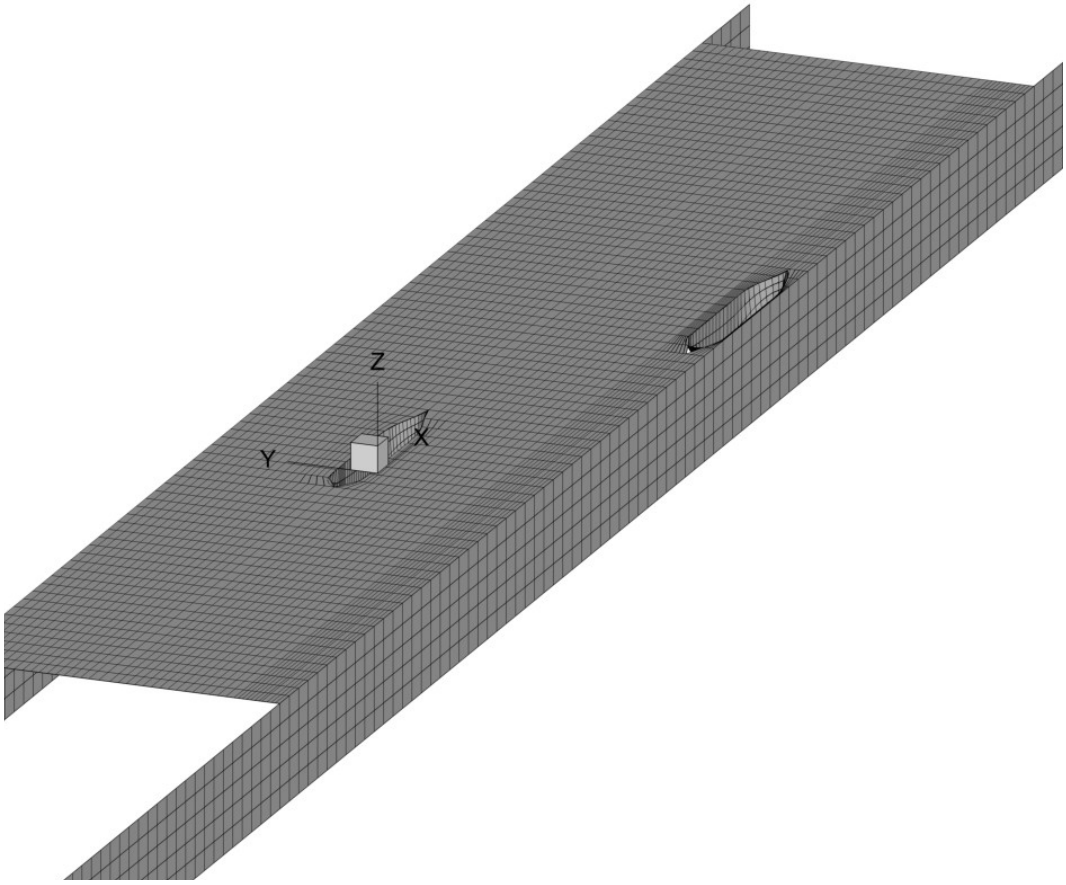

(c)

Figure 4.2: Sketch of the problem. (a): Top view of the problem; (b): Side view of the problem; (c): Mesh distribution on the computational domain.

There are 6 cases in the experiment and this research chooses the case C0406S32-CF0700 to simulate here. As can be seen in Figure 4.2a and Figure 4.2b, there are three right-handed coordinate systems in this problem: a global coordinate system O-XYZ is fixed at $X_o = 0m$ on the ground and two local coordinate systems o_1-$x_1y_1z_1$ which is located on the passing ship at $X_o = 3m$ and o_2-$x_2y_2z_2$ who is fixed on the moored ship. Here, L_1 is the length of C04 and L_2 is the length of C0P while d_o is the distance bewteen the center of the two ships; d is the water depth and D_1 and D_2 are the draft of the two ships; B_1 and B_2 are the breadth of the two ships and W is the width of the waterway; the distance between side of the two ships is denoted as d_{pass}. The ship particulars are given in Table 4.1.

Table 4.1: Ship particulars

(a): General parameters.		
Ship	C04	C0P
		MS(1:80)
$\boldsymbol{L_{pp}}$ (m)	4.367	4.350
$\boldsymbol{B}$ (m)	0.61	0.61
$\boldsymbol{D}$ (m)	0.19	0.19
		FS(1:1)
$\boldsymbol{L_{pp}}$ (m)	349.4	348.0
$\boldsymbol{B}$ (m)	48.9	48.8
$\boldsymbol{D}$ (m)	15.2	15.2

(b): Loading specific parameters.		
Ship	C04	C0P
$\boldsymbol{m}$ (kg)	320.6	326.2
$\boldsymbol{X_G}$ (m)	-0.048	-0.114
$\boldsymbol{Z_G}$ (m)	0.003	-0.002
$\boldsymbol{I_{xx}}$ (kgm^2)	11.9	11.2
$\boldsymbol{I_{yy}}$ (kgm^2)	367.4	396.6
$\boldsymbol{I_{zz}}$ (kgm^2)	385.8	376.1
$\boldsymbol{GM}$ (m)	0.09	0.045

Figure 4.2c is the mesh distribution on the computational domain. It's obvious that elements are not only distributed on ship hull but also built on bank surface. In order to save computational cost, the mesh of the sea bottom was not created, instead, a mirroring method was used for processing. In addition, based on the same

consideration, the grid is not evenly distributed on the entire free surface but divides the free surface into two parts. And because most of the experimental results in this comparison are about the moored ship, the grids around the passing ships are set to be sparser while the grid density in the width direction around the moored ships is increased.

In the numerical modelling, as shown in Figure 4.2c, there are 1480 and 1530 panels respectively distributed on the surface of the passing ship and the moored ship, while the number of panels on the free surface and bank surface is 10920 and 984, respectively. In this research, the simulation starts from x_0=8m and ends at x_0=31.5m. In order to avoid reflections at the boundary of the computational domain that could affect the results, the length of the computational domain is set to be 16.5 times the length of the passing ship. The width of the computational domain is kept consistent with the model test and is set to be 4 times the width of the passing ship. Additionally, during the calculation, the free surface will move together with the passing ship to ensure that all panels on the free surface maintain a constant distance from the passing ship at each time step, and the mesh on the free surface will be updated in real time.

In the context of ship navigation, apart from considering the interactions between ships, the influence brought about by the presence of the bank is also a crucial factor that cannot be overlooked. Obstacles within the lateral range of a vessel or alterations in the cross-sectional shape of a waterway alter the pressure field around the vessel, thereby affecting its hydrodynamics response. The design of canal cross-sections depends on the lateral distance between the ship and the bank. At this point, the restricted water effect can be referred to as ship-bank interaction. To study the interactions between the ship and bank, this thesis also selects a case of an unsteady bank to study.

The case of the unsteady bank is similarly derived from the 6^{th} MASHCON, and a 1/75 scale model of the renowned benchmark vessel KVLCC2 (Quadvlieg, 2014) was utilised in the model experiments. Comprehensive information of the ship was provided in the SIMMAN 2014 workshop, with essential dimensions presented in Table 4.2.

Table 4.2: Main dimensions of the KVLCC2 ship model.

Scale factor	1	75
$\boldsymbol{L}$ (m)	320	4.267
$\boldsymbol{T}$ (m)	58	0.773
$\boldsymbol{B}$ (m)	20.8	0.277
$\boldsymbol{C_B}$ (-)	0.81	
$\boldsymbol{C_M}$ (-)	0.81	

The present work discusses results for a channel with a constant vertical bank at one side and a so-called dock opening at the other side. The details of the channel dimensions are shown in Figure 4.3 and Table 4.3.

Table 4.3: Position of the wave gauges and velocity measurement.

WG	$\boldsymbol{x_0}$ (m)	$\boldsymbol{y_0}$ (m)	Explanation of the position
In longitudinal plane at $\boldsymbol{y_0}$ = 1.6675 m (0.1 m from quay wall)			
1	19.466	1.668	2 ship lengths before the first corner of the dock
2	28.00	1.668	At the first corner of the dock
4	36.534	1.668	At the 2nd corner of the dock
5	45.068	1.668	2 ship lengths after the first corner of the dock
In lateral plane at $\boldsymbol{x_0}$ = 32.267 m (centre line of dock opening)			
6	32.267	3.400	0.100 m from the starboard bank
3	32.267	1.668	Aligned with WG 1,2,4,5
7	32.267	-0.966	Centre of the dock
8	32.267	-3.400	0.100 m from the dock end
Velocity measurement			
-	27.000	1.6675	0.195 m above bottom; 0.1 m from quay wall

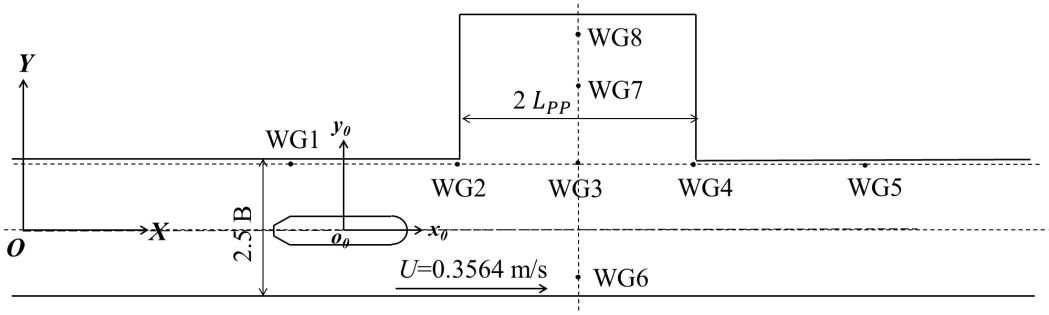

(a)

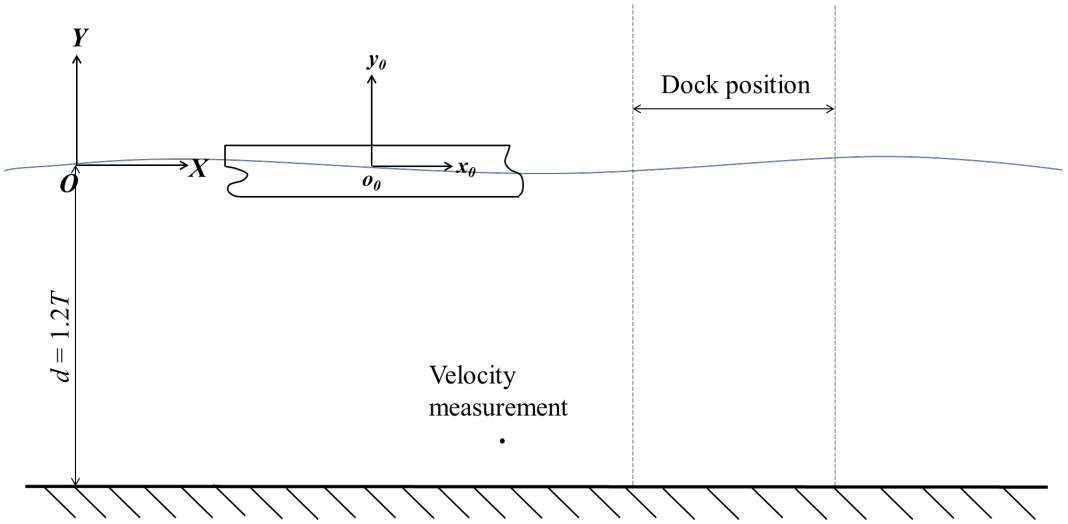

(b)

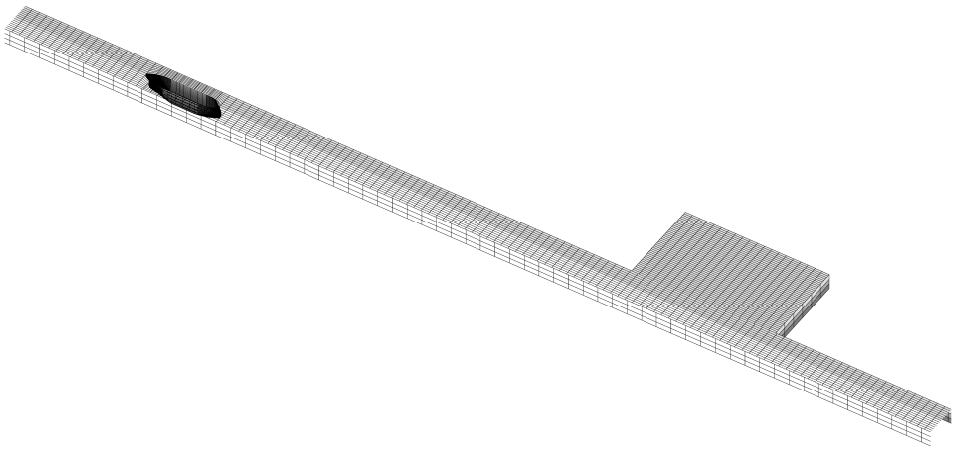

(c)

Figure 4.3: Sketch of the numerical model. (a): Top view of the model; (b): Side view of the model; (c): Mesh distribution in the computational domain.

In the numerical modelling, a total of 3,960 panels are distributed on the ship hull. For the free surface and bank surface, a total of 2,080 and 639 panels were used in the current case. In addition, to ensure the continuity of the calculation results in time domain, the time step is set to 0.0168s.

It should be noted that in all the calculations, all degrees of freedom are constrained. As a result, the sinkage and trim are obtained from the force divided by the hydrostatic

restoring force. The sinkage of the ship model was measured near the bow and the stern and then recomputed as midship sinkage and trim around the ship's origin. The same is true for the lateral force, which was measured near bow and stern and then expressed as a total sway force and yawing moment around the ship's origin.

4.4 Validations and discussions of passing ship effect

4.4.1 Quasi-steady method

Convergence study

The mesh convergence study is firstly performed. The panel number on each of the ship hull is 1480 and 1530 which is shown in Figure 4.4 and the convergence study of panel number on free surface can be seen in Figure 4.5.

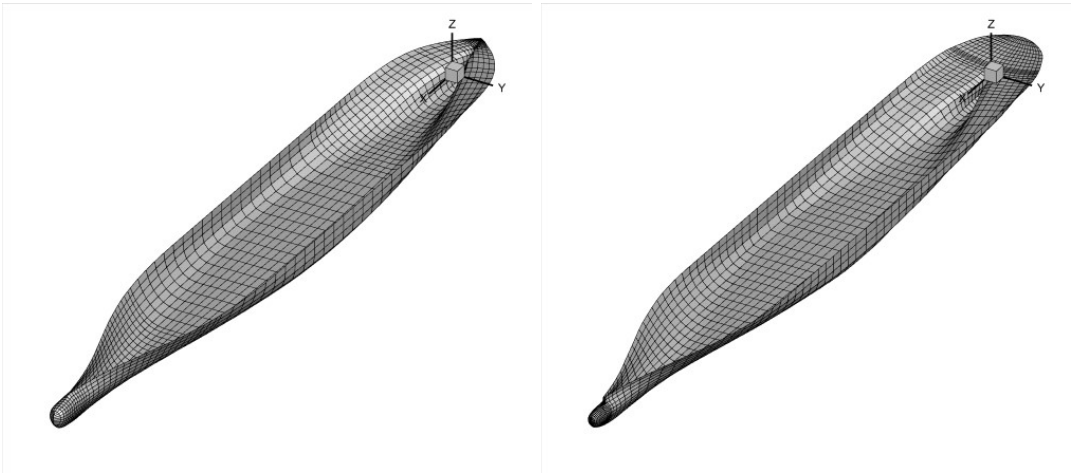

(a) (b)

Figure 4.4: Ship model used in this section. (a): Model of the passing ship (KCS) ; (b): Model of the moored ship (Neo Panamax container).

As shown in Figure 4.5, it is evident that when the grid density is set to 20x20, the simulated results deviate significantly from the expected values, indicating that the grid density within the computational domain is far from achieving convergence. However, by increasing the grid density to 40x20 and 50x20, with 40 and 50 grids distributed within the length of the ship, respectively, and 20 grids distributed throughout the

width of the entire computational domain, a pronounced convergence trend becomes apparent. Under these conditions, the results of these two sets of tests exhibit close proximity to each other. It should be noted that, for the sake of brevity, this section does not present all the results but focuses on comparing the trim of the passing ship, the sway force applied on the moored ship and the wave elevation at WG3 and WG12 where WG is the abbreviation for wave gauge and the positions of the wave gauges can be found in Figure 4.6 (Van Zwijnsvoorde et al., 2022).

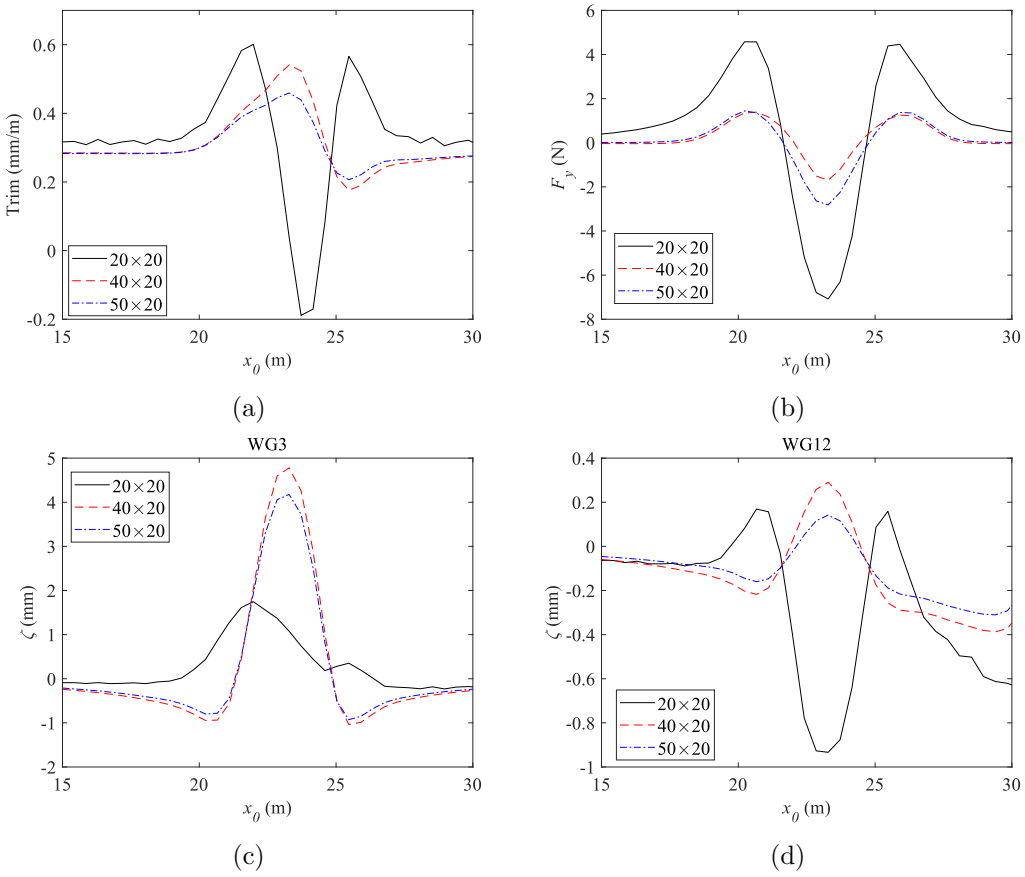

Figure 4.5: Convergence study on the two ship model in passing with different panel numbers of the free surface. The passing ship C04 passes the moored ship C0P with the speed $U = 0.3451$ m/s at the water depth h/D_1 =1.2. (a): Trim of the passing ship; (b): F_y of the moored ship;(c): Wave elevation at WG3; (d) Wave elevation at WG12.

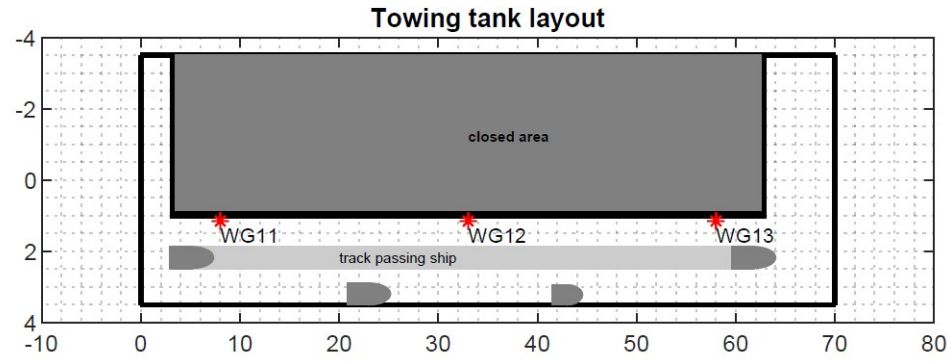

(a)

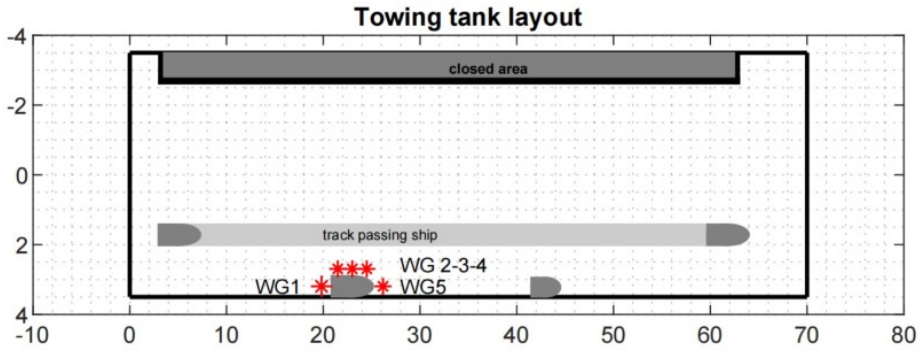

(b)

Figure 4.6: Wave gauges position. (a): Wave gauges around the bank; (b): Wave gauges around the moored ship.

Finally, considering both computational accuracy and time, the simulated results obtained from the second set of grids were selected for further investigation.

Simulation results and discussions

The boundary model mentioned in Section 4.3 will be compared and discussed in this section. Figure 4.7 displays the time series of sinkage and trim of both the passing ship and the moored ship when the former passes the latter. As shown in Figure 4.7, MHydro can accurately predict the change trend of the sinkage for both passing ships and moored ships. The only problem is that the predicted sinkage for the passing ship is much smaller than the experimental result. This is understandable, since the speed of the passing ship is very low in this case, the viscous resistance dominates instead

of inertia resistance while the fluid in potential flow theory is assumed to be inviscid, irrotational, and incompressible. This inevitably leads to a gap between the numerical results and the experimental results. For the moored ship, its velocity is zero, which means that all hydrodynamic forces acting on the hull come from the waves generated by the passing ship. Therefore, the influence of viscous is much smaller. This is why MHydro can make a relatively accurate prediction of the sinkage for moored ship.

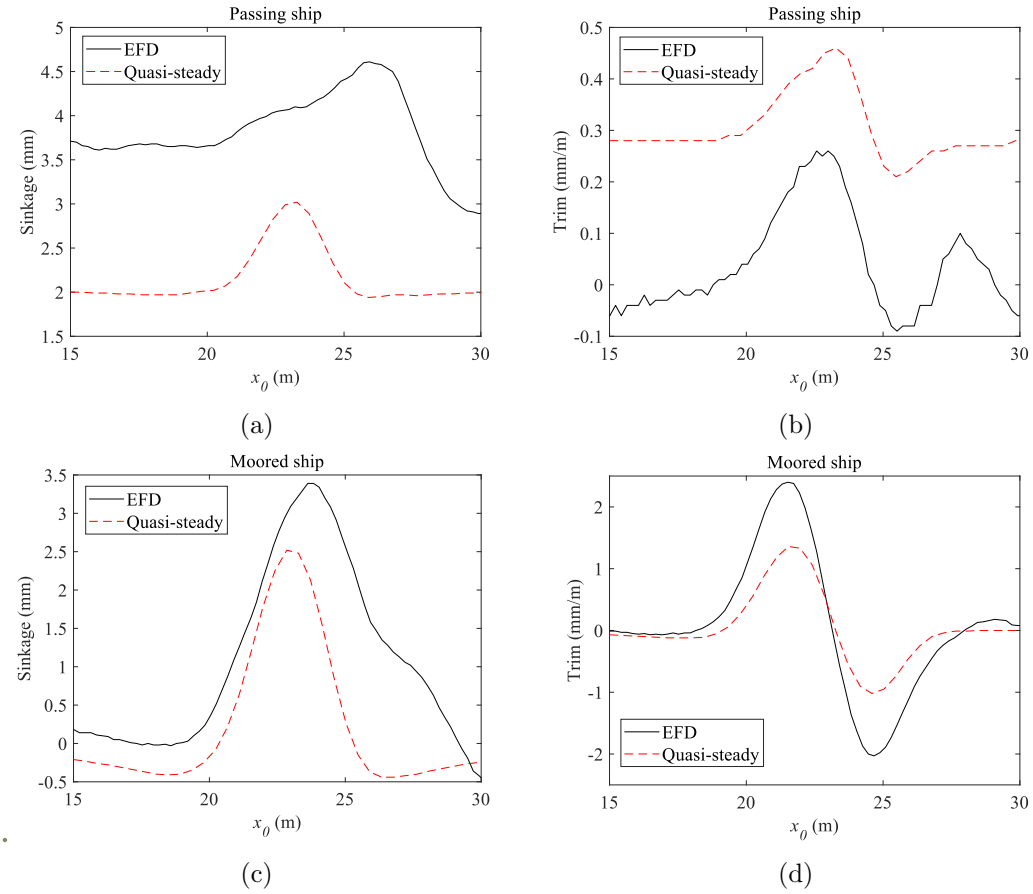

Figure 4.7: Sinkage and trim of the passing and moored ship

Figure 4.8 provides a comprehensive comparison of the hydrodynamic forces of the moored ship caused by the passing ship. The analysis reveals that the MHydro model demonstrates a commendable ability to accurately predict the hydrodynamic forces acting on the moored ship in response to the passing ship's influence. It successfully captures the main characteristics and trends of the forces. However, it is worth noting that certain small oscillations are observed in the experimental results obtained from

the EFD (Experimental Fluid Dynamics) tests, which were not fully captured by the MHydro model. These oscillations can be attributed to the presence of unsteady effects that arise due to the non-linear behaviour of the free-surface condition. The linearised and steady free-surface condition assumed by the quasi-steady is a simplifying assumption made to facilitate computational efficiency and reduce complexity. While this assumption allows for accurate predictions of the overall hydrodynamic forces, it is unable to fully capture the transient and unsteady effects present in the EFD results.

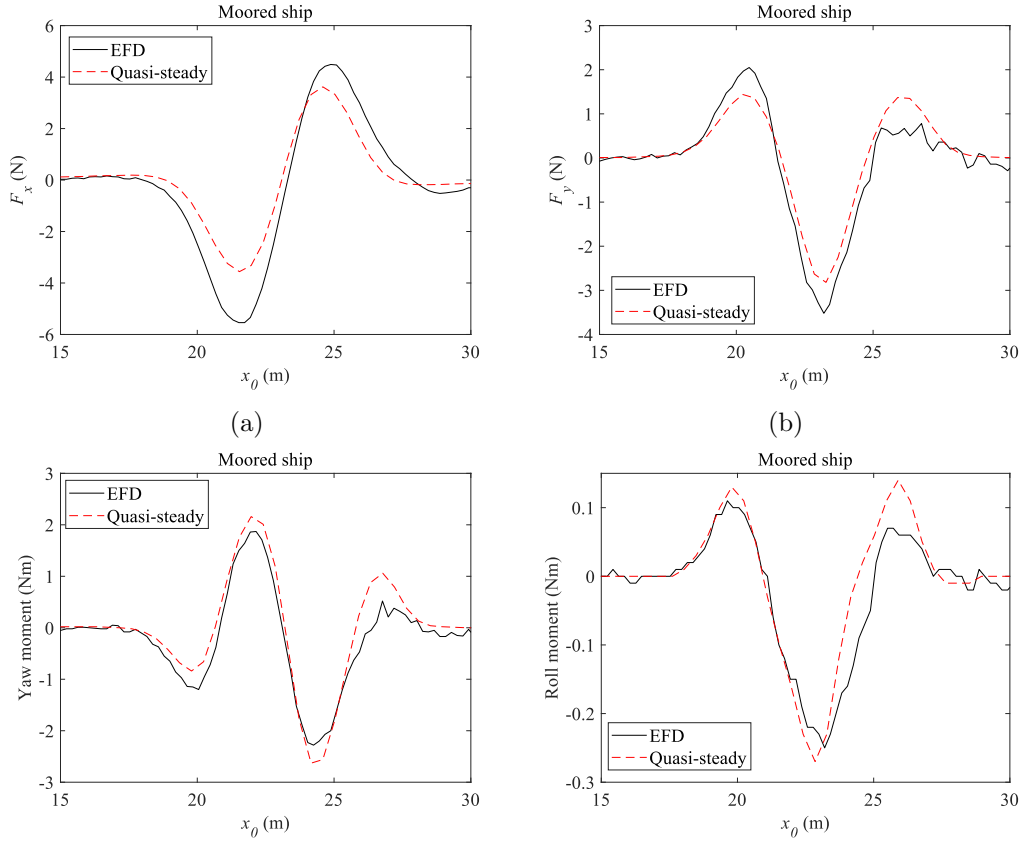

Figure 4.8: Comparison of hydrodynamic forces obtained by EFD and quasi-steady method.

A similar situation is also observed in the prediction of wave elevation. Figure 4.9 highlights a phenomenon where a bulge is present in the wave elevation recorded by wave gauges even after the passing ship has completed its passage of the moored ship.

However, this bulge is not reflected in the results obtained from the quasi-steady model. The reason behind this discrepancy lies in the approach used here, where each time step is treated independently, neglecting the unsteady free surface effects. Unsteady effects are incorporated into the calculation of hydrodynamic forces in the quasi-steady model by considering the derivative of the velocity potential with respect to time, as outlined in Bernoulli's equation.

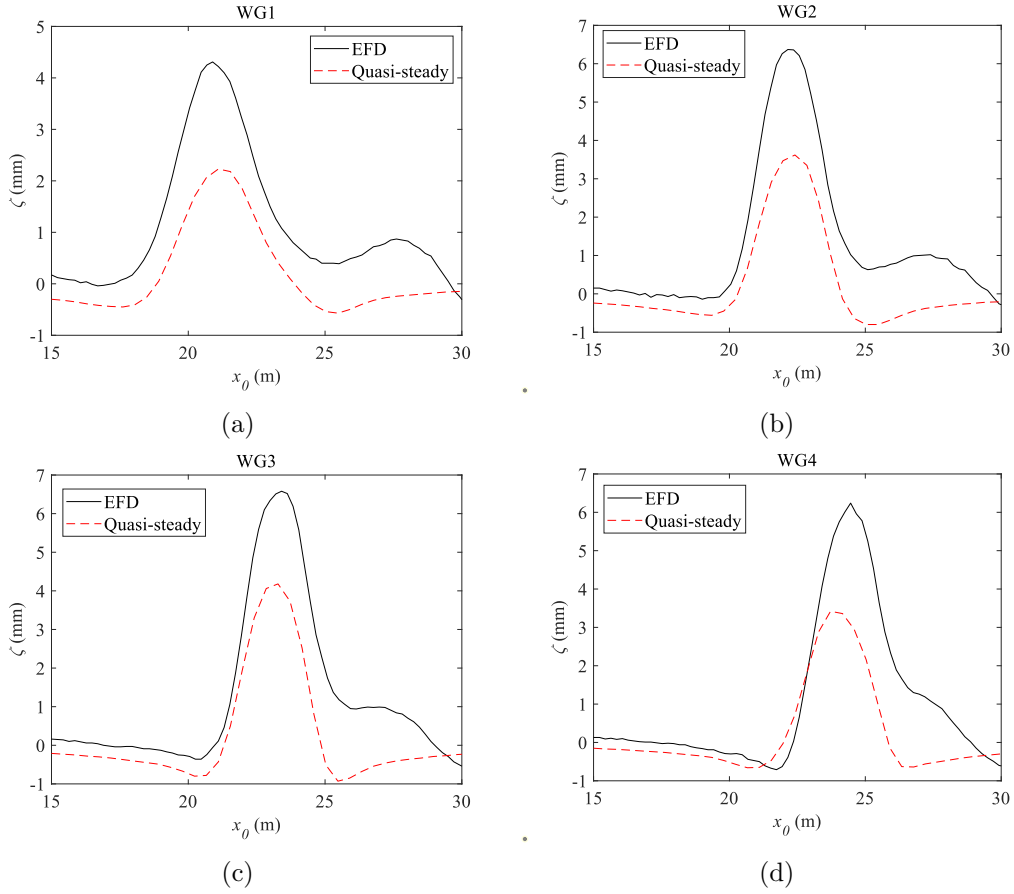

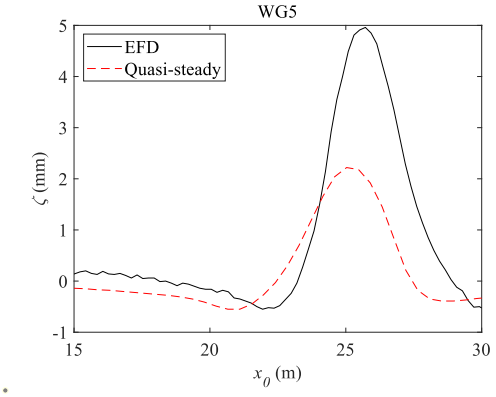

(e)

Figure 4.9: Comparison of wave elevations around the moored ship obtained by EFD and quasi-steady method.

Lastly, it is evident from Figure 4.10 that MHydro's prediction of wave elevation around the bank does not satisfactorily match the observed data. The reasons for this phenomenon in these two locations are not entirely the same. In the case of WG11, the main reason is the utilisation of a linear steady method to solve the free surface boundary conditions in this section. The wave elevation at WG11 primarily originates from the continuously propagating waves generated by passing ships, which belong to far-field waves and are characterized as unsteady waves.

Regarding WG12, the discrepancy observed at the initial stage can primarily be attributed to the absence of the ship's acceleration. The slower speed allows ample time for the acceleration waves to propagate towards the position of WG12. However, the MHydro method fails to account for this acceleration process, resulting in an initial disparity in wave elevation between the simulated results and the EFD measurements. Consequently, the absence of this initial difference in wave elevation also leads to the predicted wave elevation in Figure 4.9 being lower than the corresponding EFD results. As the ship gradually approaches the location of WG12, the influence of unsteady effects becomes increasingly important. Similar to WG11, the wave elevation at WG12 mainly results from the far-field waves generated by the passing ship, where unsteady waves dominate. Consequently, the quasi-steady method

used in this section, which neglects unsteady effects, is inadequate for effectively addressing similar problems.

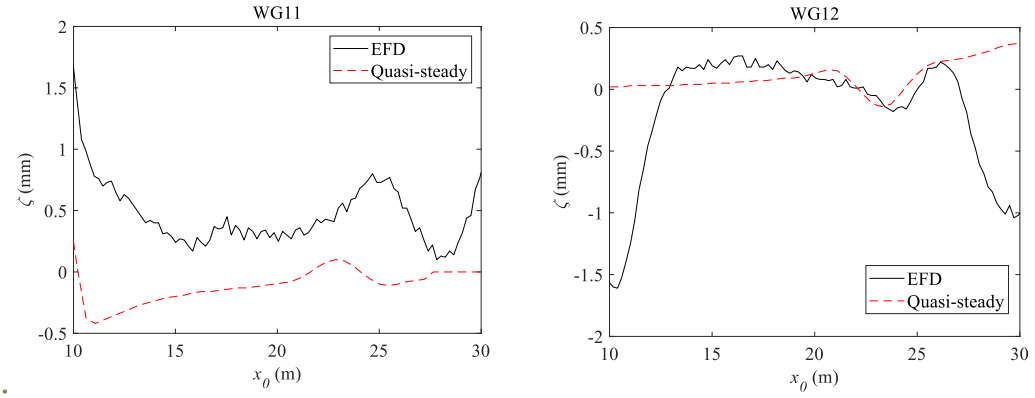

(a) (b)

Figure 4.10: Comparison of wave elevations around the bank obtained by EFD and quasi-steady method.

4.4.2 Fully unsteady method

After conducting the aforementioned comparisons and validating the results through physical model experiments, it can be deduced that the current potential flow solver is reliable in effectively solving a majority of hydrodynamic forces. Consequently, the subsequent phase of this research aims to expand its scope to encompass unsteady effects by employing a fully unsteady method. The chosen research case for this investigation remains C0406S32-CF0700.

Following numerous tests, the grid resolution on the free surface surrounding the passing ship has been determined as 286×20. Additionally, the time step (Δt) has been set to 0.0264s. In this section, a comparison will be made between the hydrodynamic forces and wave patterns obtained using two different methods, against experimental results. As previously mentioned, the first method treats the free surface boundary condition as linear and steady, which is a commonly employed and efficient approach. Subsequently, in the calculation of the pressure integral, the time derivative of the velocity potential is introduced to partially account for the influence of unsteady terms on the free surface and hydrodynamic forces.

In contrast, the second method incorporates unsteady terms through the utilisation of a three-time-level difference scheme while solving the free surface boundary equations, resulting in a fully unsteady approach. The advantage of this method lies in its ability to comprehensively capture the effects of unsteadiness on the results. However, a notable drawback is the necessity to strictly control the length of each time step to ensure the results are not dependent on individual time steps, thus significantly increasing the computational requirements.

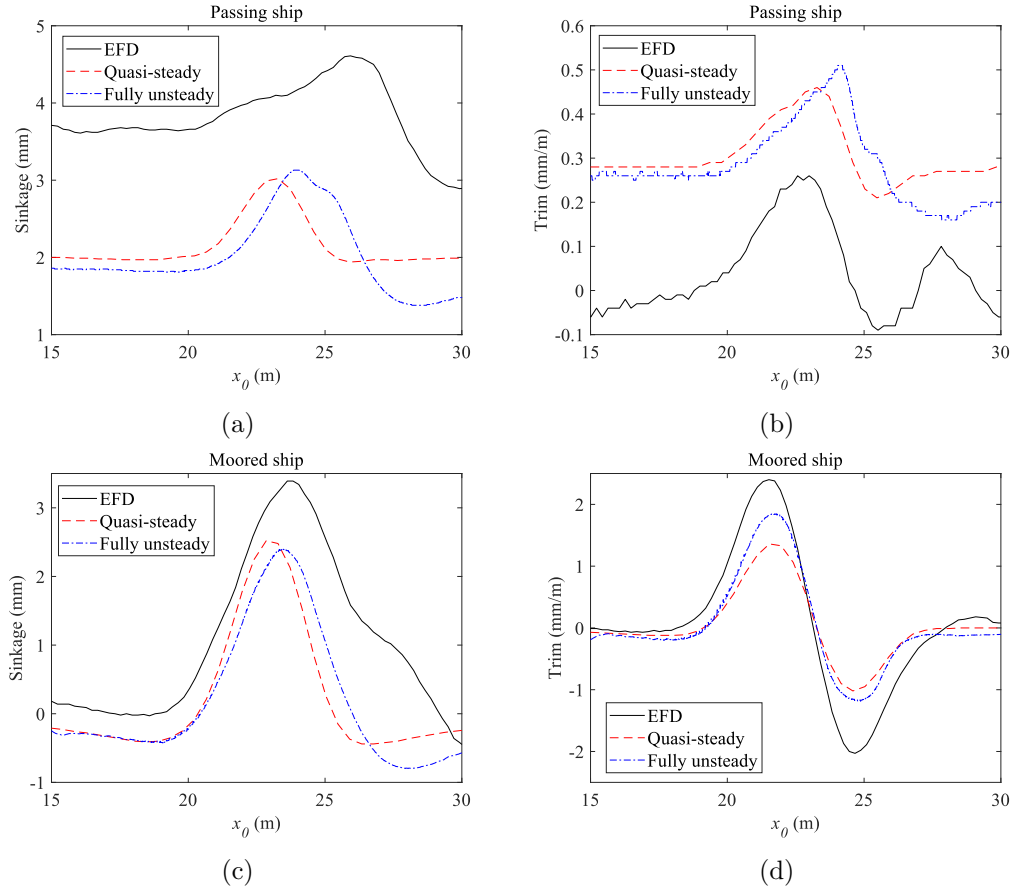

Figure 4.11: Comparison of sinkage and trim for the passing and moored ship obtained by EFD and MHydro method.

As shown in Figure 4.11a and Figure 4.11b, even after considering unsteady effects in the simulation, the calculated results for the sinkage and trim of the passing ship still deviate significantly from the experimental results. As previously mentioned, one of the reasons for this discrepancy is that the MHydro method is based on potential

flow theory, which neglects the viscosity of the fluid. On the other hand, since the inclusion of unsteady effects does not adequately explain the substantial difference between predicted and actual values, it is evident that viscosity alone cannot account for this disparity.

Therefore, this work argues that the influence of the acceleration phase experienced by the passing ship at the initial stage cannot be ignored, especially considering that the selected case represents a shallow-water scenario. As described in Chapter 3, the acceleration effect of the ship becomes more pronounced in shallow water. Consequently, there exist differences between the initial values of the predicted and experimental results, making this comparison inherently unfair.

Compared to the passing ship case, the fully unsteady method yields significantly improved predictions for the sinkage and trim of the moored ship, particularly with respect to the trim, which aligns closely with the experimental results, as shown in Figure 4.11c and Figure 4.11d. As mentioned in the previous section, for a moored ship with zero velocity, accurately simulating the waves generated by the passing ship, including both steady and unsteady waves, naturally leads to more precise results.

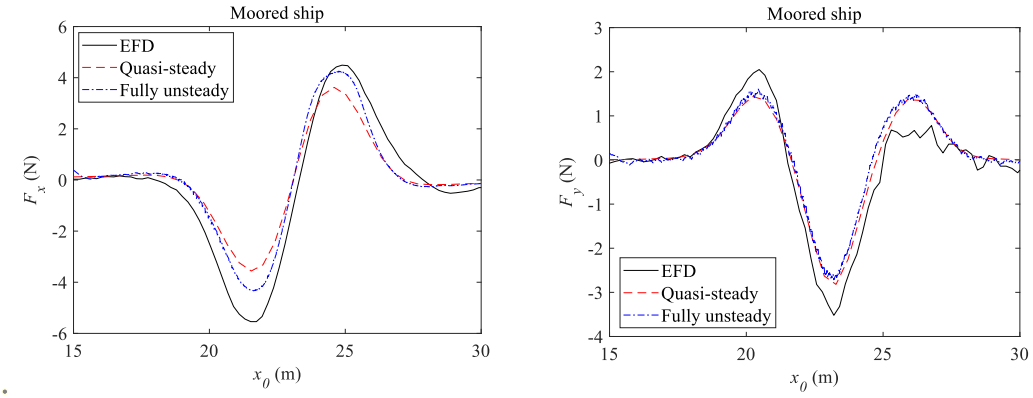

(a) (b)

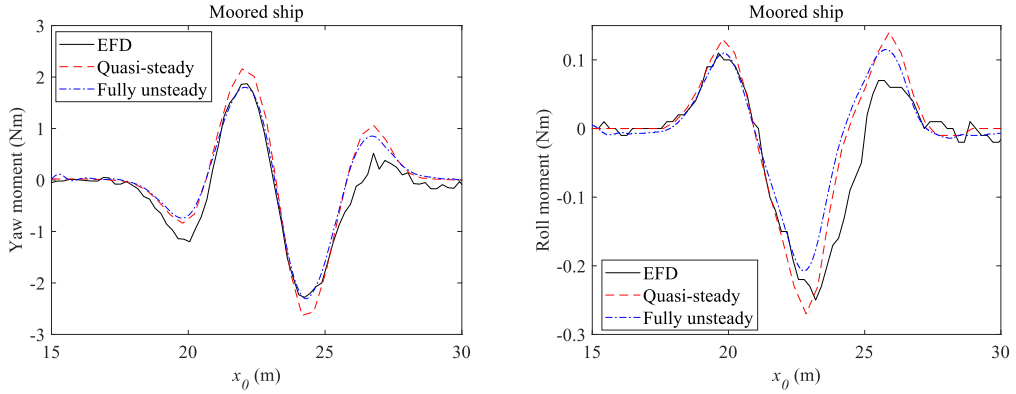

(c) (d)

Figure 4.12: Comparison of hydrodynamic forces for the passing and moored ship obtained by EFD and MHydro method.

As illustrated in Figure 4.12, a notable agreement can be observed between the theoretical and experimental outcomes concerning the hydrodynamic forces exerted on the moored ship. Figure 4.12a highlights that during the approach of the passing ship to the moored ship, the horizontal force initially undergoes oscillations, a phenomenon not captured by the quasi-steady method but evident in the results obtained through the fully unsteady method. This phenomenon is also observable in the initial stages of roll and yaw moment. Furthermore, several results in Figure 4.12 exhibit minor oscillations in the subsequent stages, apart from the prominent peaks or troughs observed in the initial stage. These oscillations primarily arise from far-field waves generated by passing ships. However, due to the relatively low velocity of the passing ship, capturing these oscillations is challenging for simulation results, as the interaction forces are primarily influenced by perturbations caused by near-field waves. Moreover, the fluctuations induced by far-field waves do not significantly deviate from the forces induced by near-field waves. Overall, all the results presented in Figure 4.12 demonstrate excellent agreement with the experimental results.

Furthermore, apart from analysing the hydrodynamic forces, this research also conducted a comparison of the wave elevations, as depicted in Figure 4.13. The comparison involves the wave gauge records of WG1, WG3, WG5 and WG11, WG12.

As described in the captive model test, wave gauges 1, 3 and 5 measure the wave elevation on the portside of the moored ship, from stern to bow, in the time domain. On the other hand, wave gauge WG11 and WG12 capture the waves generated by the passing ship near the bank, specifically at the locations $x_0 = 8$m and $x_0 = 33$m, as illustrated in Figure 4.6.

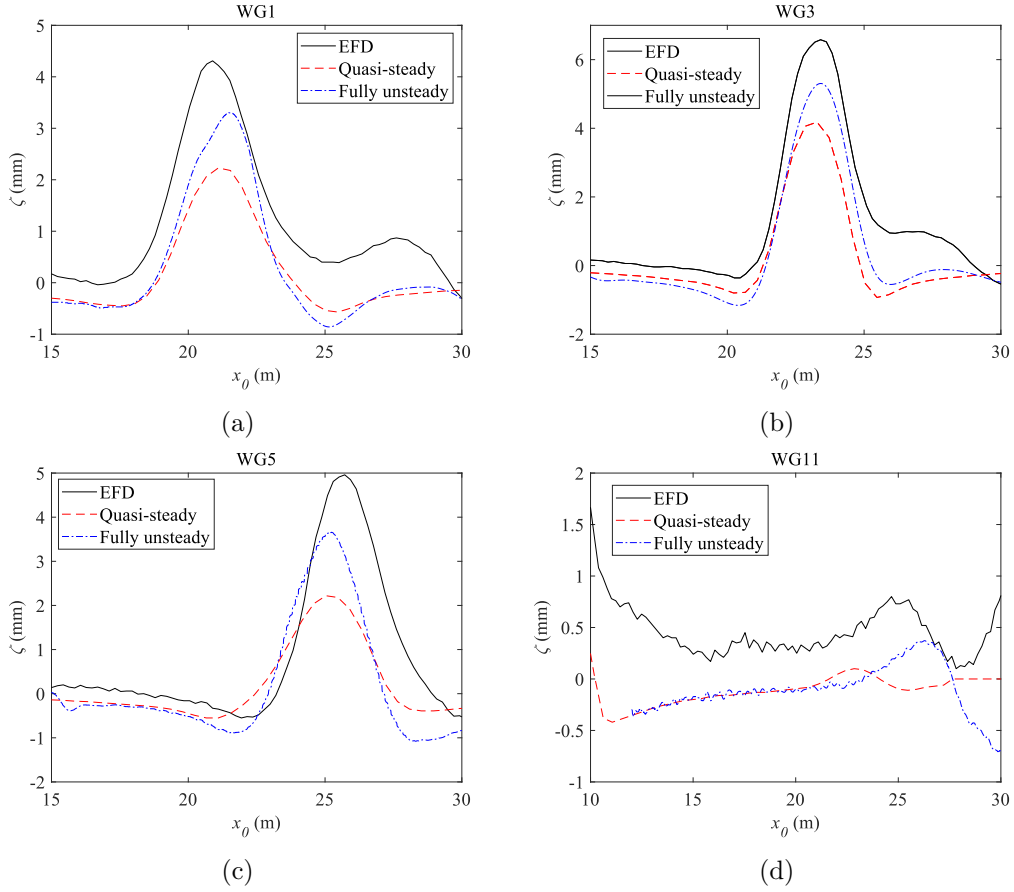

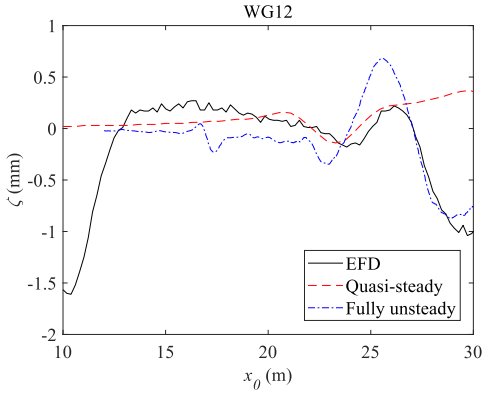

(e)

Figure 4.13: Comparison of wave elevations around the moored ship and bank obtained by EFD and MHydro method.

As depicted in Figure 4.13, the wave elevation results exhibit a consistent trend for both the bank waves and the waves around the moored ship. The only drawback is that the theoretical troughs are slightly smaller than the experimental ones. Additionally, the initial stage difference between the two results has been explained in the previous comparison of hydrodynamic forces. The focus of this section will now shift to discussing the reasons for the discrepancy between the two waves after the overtaking process is completed.

According to the results obtained from the quasi-steady method, once the overtaking process is completed ($x_0 > 27.36$m), the wave results at all positions surrounding the moored ship rapidly return to a horizontal straight line. This behaviour is attributed to the gradual transition of disturbance acting on the moored ship from the divergent stern-wave disturbance generated by the passing ship to the transverse wave disturbance. It is crucial to note that this disturbance, particularly the transverse wave disturbance, is closely associated with unsteady effects. Hence, even after the overtaking process, wave oscillations are still observable in both experimental results and the results obtained from the fully unsteady method.

However, it should be acknowledged that our calculated theoretical values exhibit smaller oscillation amplitudes compared to the experimental results. This discrepancy

may arise due to the absence of flow viscosity and acceleration of the passing ship in our calculations. Finally, it is important to highlight that the Froude number (Fr) used in this research is only 0.0527, indicating a relatively slow passing speed of the ship. In practice, when the ship operates at medium or high speeds, the hydrodynamic forces resulting from far-field wave interactions can become significant. Consequently, it becomes imperative to consider unsteady effects when solving for hydrodynamic forces or wave elevations for high-speed ships.

4.5 Validations and discussions of unsteady bank effect

4.5.1 Free surface deformations

It can be seen in Figure 4.14, the smallest channel is depicted, illustrating the free surface deformations along the quay wall. The greatest reductions in water level are evident when the midship position closely aligns with the wave gauge location, aligning with the physical principle of the pressure system that moves with the ships. However, all the predictions provided by MHydro, while effectively demonstrating the variation trend of wave elevations at their respective locations, consistently underestimate the results. This discrepancy is likely attributable to the fact that the ship remains fixed in the simulations, whereas in the experiments, it is free to heave and pitch. These motions lead to a greater depression in the free surface, especially when the dynamic under keel clearance is limited.

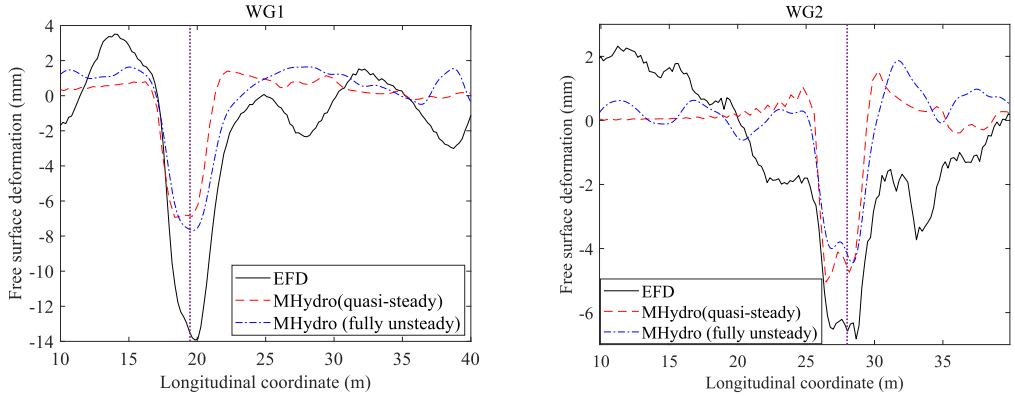

(a) (b)

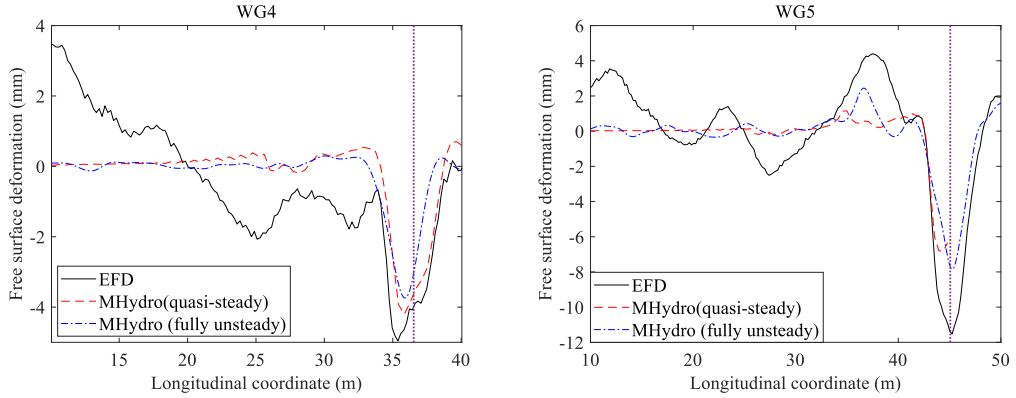

(c) (d)

Figure 4.14: Free surface deformations along the quay wall where the location of wave gauge is presented by a purple dotted line. The horizontal axis here represents the coordinate of x_0.

Figure 4.15 displays the other wave gauges, which focus on the deformation of the free surface at the dock. It can be observed that a similar pattern emerges in the predictions of wave elevations within the main channel, as seen previously. However, regrettably, MHydro fails to provide effective simulations for the waves within the dock. Additionally, a comparison of the wave elevations at WG3 and WG6 reveals a more pronounced decrease in the free surface closer to the quay wall. This aligns with the expected physical phenomenon resulting from ship-bank interactions.

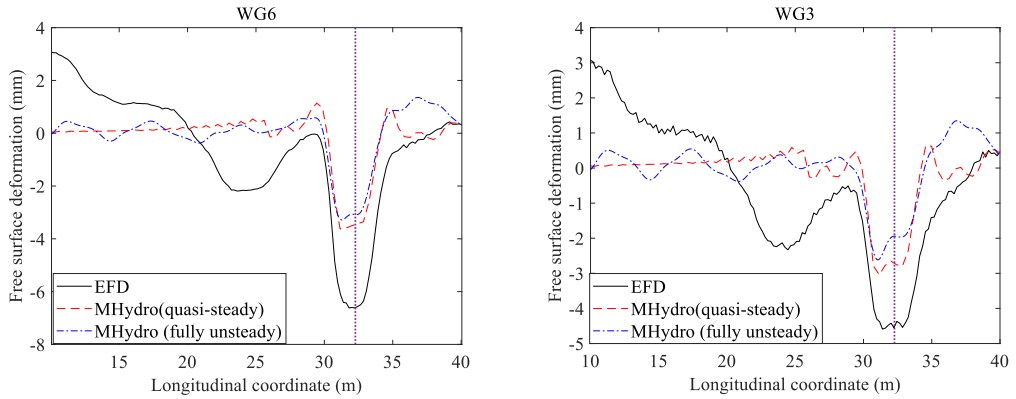

(a) (b)

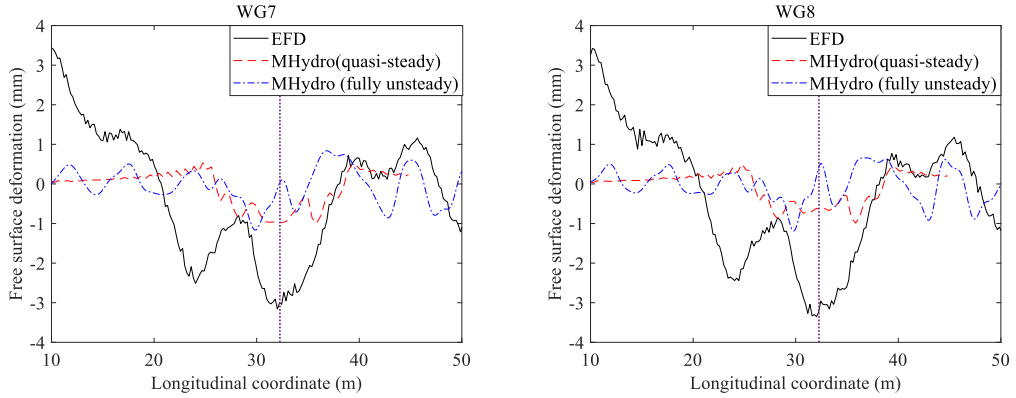

(c) (d)

Figure 4.15: Wave elevations at dock opening.

4.5.2 Velocity profiles

Figure 4.16 presents longitudinal and transverse current profiles. The position of the measurement point is indicated in the figure as a function of the midship location, represented by a purple dashed line. It can be seen that when the ship approaches the measurement location, the longitudinal current velocity reaches its maximum, which is associated with the return flow generated as the ship travels forward along the x-axis. MHydro can predict the longitudinal flow velocity quite well at this point. However, when it comes to predicting the lateral current velocity, although it still captures the correct trend, the predictions generate significant negative values before the midship reaches the measurement location. Although this aligns with the physical fact that water must be displaced for the ship to pass through this point, the overshoot in the experimental results is much smaller than what the numerical simulations suggest.

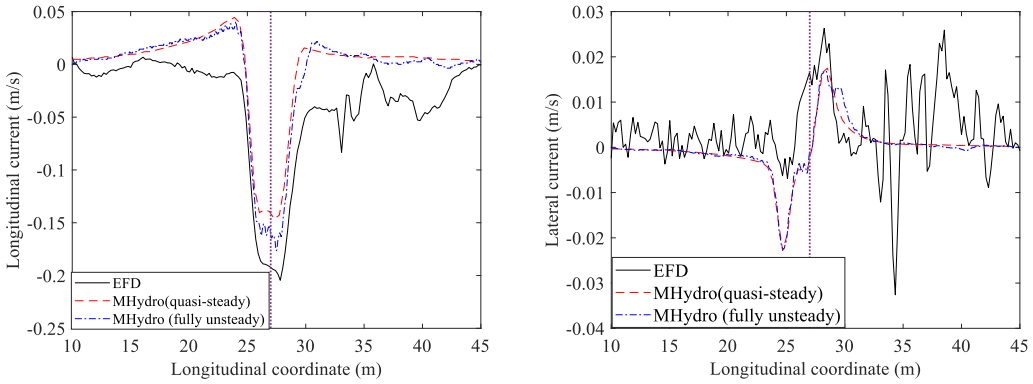

(a) (b)

Figure 4.16: Fluid velocity near the quay wall.

4.5.3 Sinkage and trim

The evolution of the midship sinkage and trim of the ship model can be observed in Figure 4.17. Clearly, when the channel suddenly widens, the ship's sinkage and trim both decrease accordingly. The fully unsteady MHydro effectively captures the oscillatory trend in the ship's sinkage, although it exhibits an overall offset compared to experimental values, leading to an underestimation. This is believed to be closely related to the initial acceleration phase present in the experiments but not included in the simulation results. This acceleration phase induces initial sinkage and trim in the vessel, causing a certain deviation between the numerical simulation and experimental results during the initial phase.

It's worth noting that the unsteady effects result in sustained oscillations in the results, as evidenced by the stable trends seen in predictions provided by the quasi-steady method.

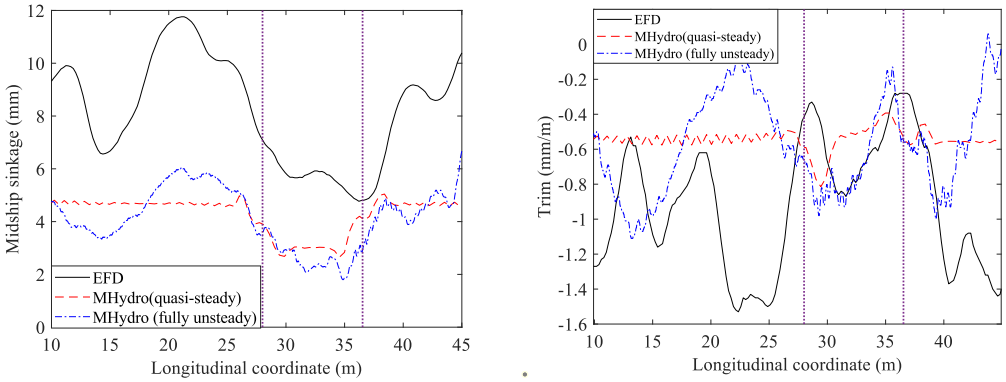

(a) (b)

Figure 4.17: Sinkage and trim where the purple dotted lines represent the location of the dock opening.

4.5.4 Sway force and yaw moment

The sway force and yaw moment applied on the ship model are shown in Figure 4.18. When the ship approaches the dock opening, it experiences a significant lateral yawing moment. At this point, the ship transitions from a state of navigating along the centerline of the channel to a significant eccentric condition at the dock opening, resulting in an attractive force towards the nearest bank due to the ship-bank interaction. Subsequently, as the vessel is about to pass through the dock opening, the attraction at the bow of the ship reappears on the portside bank, explaining the changed sign of yaw moment.

Similar to the previous situation, MHydro is capable of capturing the changing trends in the ship's sway force and yaw moment. However, the predicted values are significantly lower than those obtained from experimental measurements. This discrepancy is closely related to viscosity since MHydro is based on potential flow theory which neglects fluid viscosity.

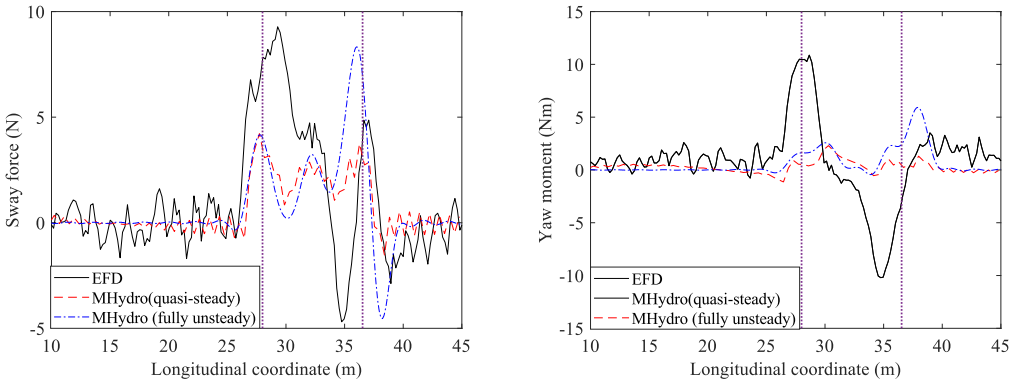

(a) (b)

Figure 4.18: Sway force and yaw moment.

4.6 Summary

Based on the research of Yuan (2019), this research extends the potential flow solver to solve the unsteady effect on the free surface to simulate the ship-passing effect in shallow and confined waterways, and compares it with the experimental results. By comparison, it can be observed that the current potential flow solver can achieve satisfactory results when solving passing ship problems. However, when addressing unsteady bank problems, the obtained results often fall short of the experiment values. This discrepancy is closely related to the initial acceleration phase in the experiment and the viscosity of the fluid. In addition, compared with previous studies, after keeping the unsteady terms in the free surface conditions, this research has been able to successfully capture the oscillation of the wave and forces.

In conclusion, this research provides an improved tool for computing and analysing passing ship problems and unsteady bank problems.

Chapter 5

Unsteady waves generated by a body when entering a lock

5.1 Introduction

Due to sudden changes in waterways, such as variations in banks or water depths, the hydrodynamics of a moving ship become highly intricate and challenging to analyze. One of the most typical and complex scenarios in which hydrodynamics plays a crucial role is when a ship enters a lock. This manoeuvre involves navigating through a confined space with limited clearance, and it poses unique hydrodynamic challenges. Most of the published work on the ship entering lock scenarios has primarily focused on studying the ship's manoeuvrability or the hydrodynamic forces acting on the vessel.

For example, researchers such as Vantorre and Richter (2011) have investigated how the hydrodynamic characteristics of a ship entering a lock are influenced by various factors, including the approach channel and structure layouts, water depth, translation waves, return flow, cushion effects, and other relevant parameters. In the earlier years, experimental measurements were considered the most reliable approach for studying this problem. Notably, the David Taylor Model Basin conducted numerous experiments to explore the effect of different cross-sections on ship manoeuvrability (Schoenherr, 1960). More recently, computational fluid dynamics (CFD) methods (Tezdogan et al., 2016) and 3D potential flow methods (Xu et al., 2016) have also been employed to

address the hydrodynamic challenges encountered during ship lock entry. However, in these studies, the free surface within the lock was often treated as a rigid wall, disregarding the influence of waves. In a step towards more accurate simulations, Yuan (2019) considered the free surface in his simulations of ship lock entry. However, he did not account for the unsteady terms in the free surface boundary conditions, which play a crucial role in capturing the complex dynamics of waves in this scenario.

To overcome these limitations and accurately simulate the unsteady 3D waves within a lock, this thesis utilizes a 3D potential flow solver known as MHydro. MHydro is specifically designed to address the unsteady effects associated with ship-bank, ship-bottom, ship-lock, and ship-ship interactions. It is based on the 3D boundary element method (BEM) and employs a Rankine-type Green function to compute potential flows. However, in contrast to the previous method proposed by Yuan (2019), this research takes a further step by introducing a three-time-level scheme to handle the unsteady problems inherent in the boundary value problem. This scheme ensures that the results at each time step are not treated independently and that the unsteady terms in the boundary conditions are retained. Additionally, a novel meshing method is adopted, enabling the accurate representation of abrupt changes in the free surface caused by variations in the boundary geometry.

5.2 Methods

5.2.1 Description of the problem

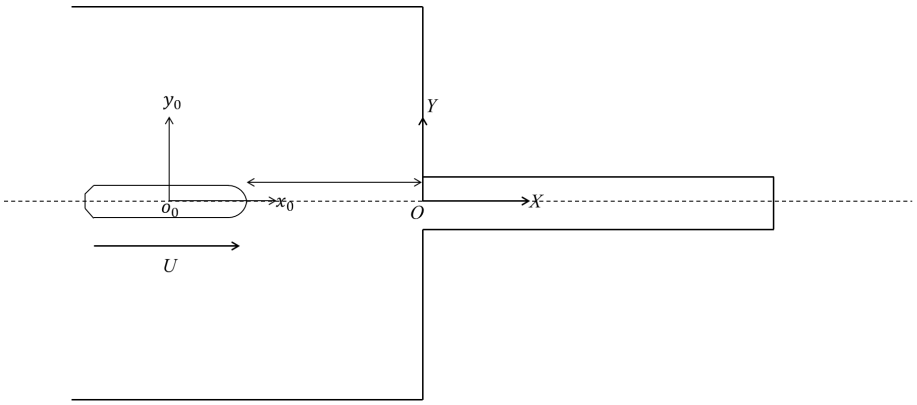

Figure 5.1: Sketch of the problem.

As shown in Figure 5.1, the study in this research involves a total of two right-hand coordinate systems: a global coordinate system $O - XYZ$ that is fixed to the middle of the lock entrance and a local coordinate system $o_0 - x_0y_0z_0$ which is located at the geometry centre of the ship. The positive direction of the x-axis in the global coordinate system points from the lock entrance towards the lock gate, while the x-axis in the local coordinate system points from the ship stern to the ship bow and the positive direction of both z-axes is upward. The ship moves with a constant velocity U along the positive direction of the x-axis and gradually enters the ship lock. It should be noted that, since this method is based on potential flow theory, the fluid in this research is assumed to be ideal, which means it is assumed to be inviscid, irrotational and incompressible.

5.2.2 Return flow

Different from the cases mentioned in the previous chapters, ship-lock interactions are very difficult to predict because the shallow water depth and the sudden narrowing of the channel will also make the bank effect very obvious. When the ship is entering the ship lock, the water will be limited in the narrow space between the ship and the lock gate and keeps accumulating or evacuating which leads to a return flow. In the present

research, the effect of return flow will be added to the body surface condition. Although the ship sails along the positive x-direction with a constant speed U, once it reaches the entrance of the lock, the water volume will be increased by:

$$\Delta V = U A_s(t) \cdot \Delta t \tag{5.1}$$

where A_s is the cross-section area of the ship's wetted surface at moment t. This means a return flow will follow and the same volume of water will flow through the clearance between the ship and the lock bank. As the ship keeps entering the lock, the distance between the ship bow and the lock gate will continue to decrease which results in the velocity of return flow $v(x, t)$ increasing (Yuan, 2019). Considering the return flow as a uniform flow, the effect of the return flow can be treated as an additional speed $v(t)$:

$$\frac{\partial \varphi}{\partial n} = [U + v(t)] n_1 \tag{5.2}$$

where $v(t)$ can be obtained by:

$$v(t) = \begin{cases} 0, & \text{while } t \leq t_e \\ \kappa \frac{\delta}{l} (t - t_e) U^2, & \text{while } t_e < t \leq t_c \end{cases} \tag{5.3}$$

where δ is the blockage ratio which equals the ratio of the cross-section area of the ship's wetted surface to the wetted cross-section area of the lock, l is the lock length, t_e represents the moment when the ship arrives at the entrance of the lock and t_c represents the moment when the ship is totally in the lock. As the existence of the return flow, the ship will receive an acceleration and κ is, therefore, the acceleration coefficient. After the moment t_c, the return will still exist. However, the acceleration coefficient will be smaller than κ because the total water volume in the lock will remain constant at this time, while the return flow mainly comes from the change in water volume. In this case, an empirical iteration method is introduced to estimate the return flow velocity:

$$v(t_n) = v(t_{n-1}) + \kappa \frac{\delta}{l} (U \Delta t) \left[v(t_{n-1}) - v(t_c) + U \right], \text{ while } t > t_c \tag{5.4}$$

where $v(t)$=$v(t_c)$ is the initial condition of Eq. (5.4).

Another thing that needs to be pointed out is that a new automatic updating mesh method is used in this chapter. As mentioned earlier, the results at each time step in this solution are interrelated, which means that the distance from the corresponding associated panel to the ellipsoid should be fixed at each time step. In past studies, due to the fixed shape or length of the computational domain, a simple approach was sufficient, where the entire computational domain moved forward with the ship, as shown in Figure 5.2a. However, in the case of the ship-lock problem, the changing geometry of the bank and the closed lock gate prevent the computational domain from continuing to move forward when the leading edge of the domain reaches the bank or the location of the lock gate. In order to ensure the continuity of the grid on the free surface in both time steps and in response to the changing boundaries, this research adopts a strategy of removing the cells at the last column of the free surface from the previous time step, allowing the remaining cells to maintain temporal continuity, as illustrated in Figure 5.2b.

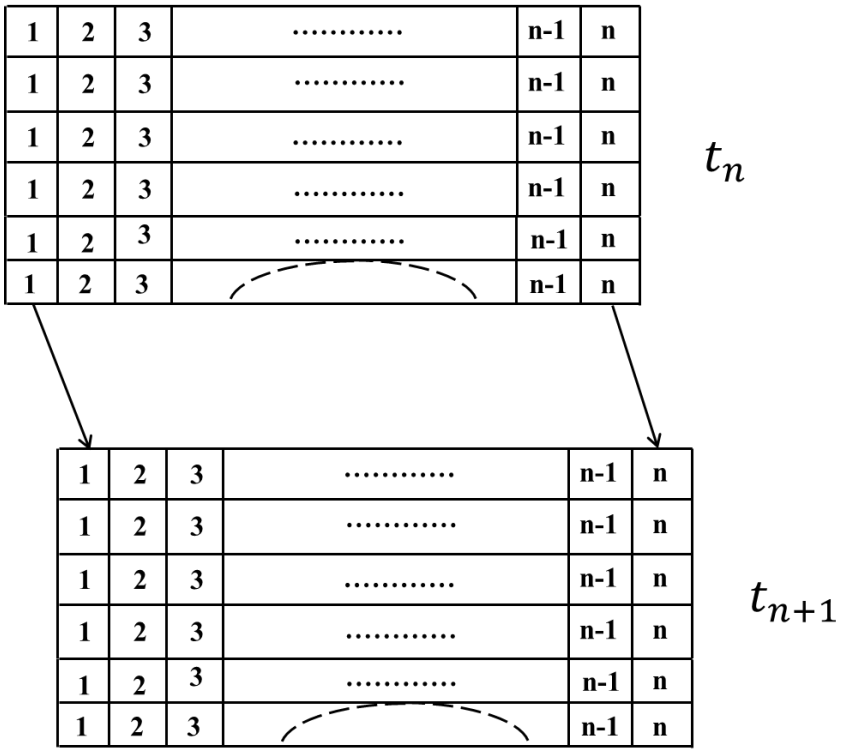

(a)

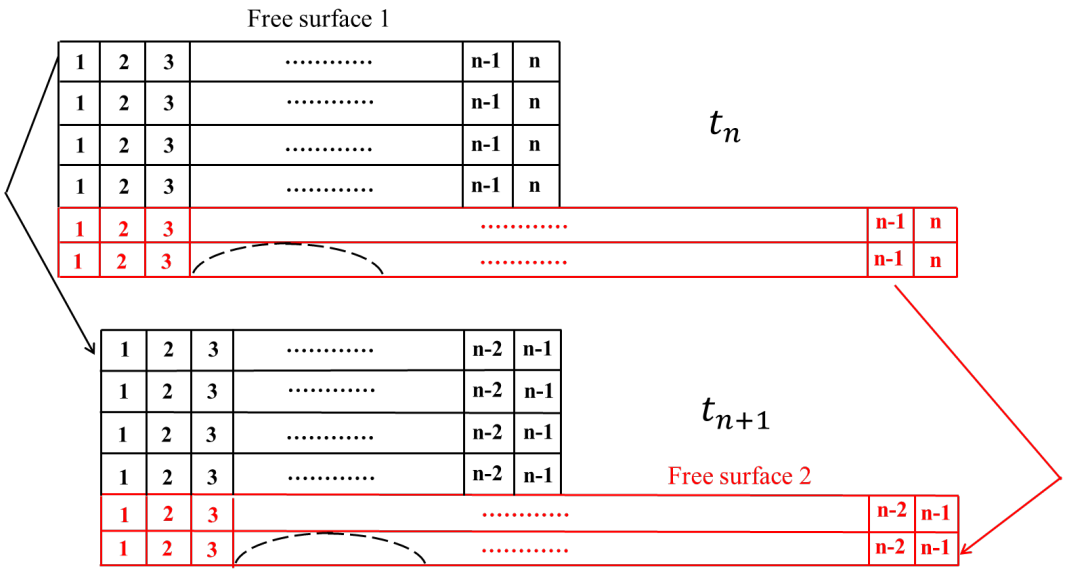

(b)

Figure 5.2: Correspond relation of free surface 1 and free surface 2 between each time step.

5.3 Experiment and numerical simulation settings

This chapter consists of two cases: one is a submerged ellipsoid entering a lock and the other is the entry of a box into a lock. To validate the accuracy of the simulation results, the author conducted separate experiments for each case.

5.3.1 A submerged ellipsoid entering a lock

The first experiment involved in this research is an ellipsoid entering the lock under the deep-water condition.

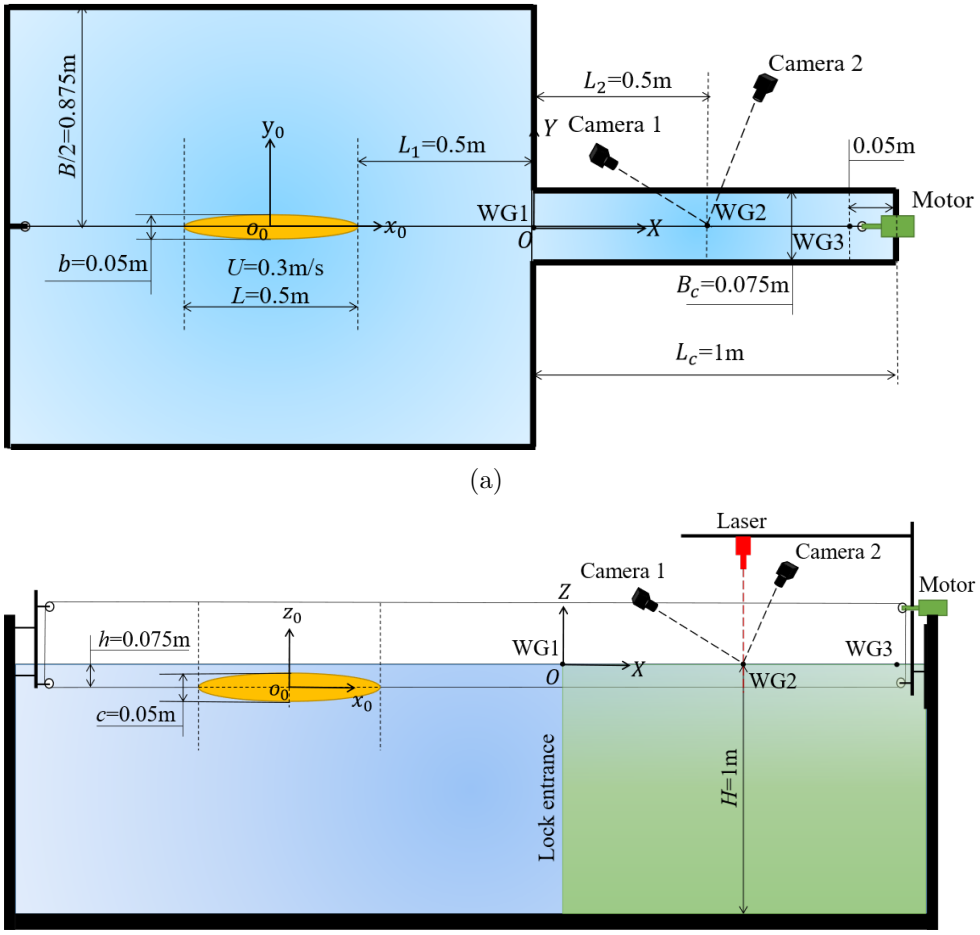

Figure 5.3: The sketch of the problem and the experimental setup. (a) Top view; (b) side view.

This case involves the motion of a submerged ellipsoid (length:0.5m, width and height: 0.1m) as it enters a lock. As shown in Figure 5.3, the submerged ellipsoid is towed by a fishing wire that is connected over four pulleys in a close loop configuration. Driven by a motor, the ellipsoid will enter the lock with a target forward/backward speed. Due to the confined experiment condition, instead of wave gauges, an optical method based on the stereo vision principle was used. A steady-state laser transmitter is used to generate an illuminant at the position where the wave elevation needs to be measured in this case. During the process of entering the lock, the cameras set above the lock area will continuously film the light dot on the water surface with a frequency of 60

Hz. Thus, the time-history information of the free surface elevation at this point is obtained by calculating the position of the light dot. The model tests of an ellipsoid entering a lock were conducted at Kelvin Hydrodynamics Laboratory (KHL). The 3D Compact wave tank of KHL is used in this test, which is 9.267 m (length) × 3.15 m (breadth) × 1 m (depth).

In the numerical modelling, the panels are distributed on the body surface, free-surface and bank surface and in order to save computational time, this chapter utilizes the symmetry of the calculation domain and only establishes half of the domain, thus reducing the total number of panels required in the solution. The specific parameters of the ellipsoid used in the experiment are shown in Table 5.1. Furthermore, a convergence analysis is also included in this chapter to ensure the stability of the numerical simulation results, as shown in Figure 5.4 where the wave-making resistance is the non-dimensionalized coefficients of surge force which can be calculated by:

$$C_w = \frac{R_w}{(1/2)\rho U^2 S} \tag{5.5}$$

where S is the area of the wet body surface, ρ is the density of the water, U is the veloicity of the ellipsoid and R_w denotes the wave-making resistance, which equals F_1 in Eq. (5.5).

Table 5.1: Main particulars of the ellipsoid.

Length ($\boldsymbol{L}$) (m)	0.5
Breadth ($\boldsymbol{B}$) (m)	0.1
Draft AmidshipsDraft ($\boldsymbol{T}$) (m)	0.125
Longitudinal CoG ($\boldsymbol{X_G}$) (m)	-0.75
Vertical CoG ($\boldsymbol{Z_G}$) (m)	-0.075

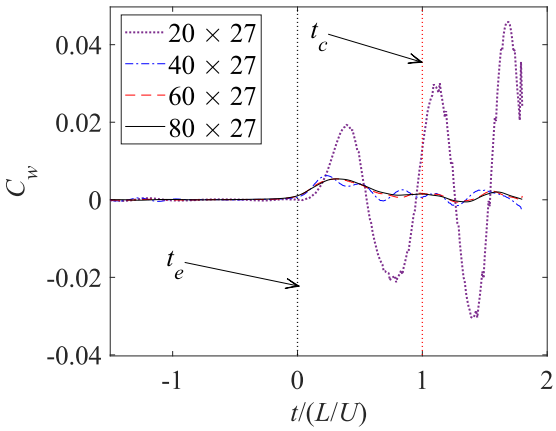

Figure 5.4: Convergence study on the numerical model where C_w is the wave-making resistance coefficient of the ellipsoid and $t/(L/U)$ is the dimensionless over time t.

The convergence study of the number of panels on the free surface includes four sets of grids, i.e., 40×27, 60×27 and 80×27 panels in the x and y directions within each ship length. After considering both the accuracy of the computational results and computational efficiency, this chapter chose the third set of grids to construct the numerical model. To conclude, there are 600, 468 and 4440 panels respectively distributed on the body surface, bank surface and free surface, as shown in Figure 5.5.

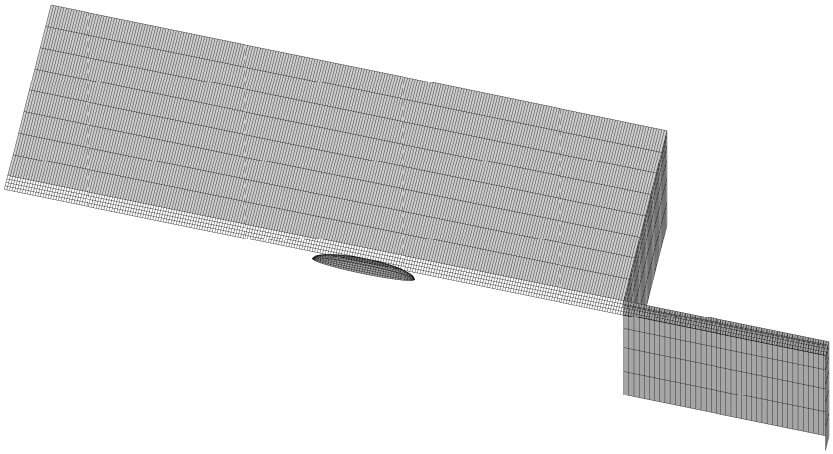

Figure 5.5: Panel distribution on the computation domain of an ellipsoid advancing into a lock (only half of the computational domain is shown here).

Due to the use of a completely unsteady method in this chapter, it is necessary to ensure

that all results are interrelated to each other at each time step, while this method also has strict requirements on the time step. In the end, the time step in this simulation was set to 0.0139s.

5.3.2 A box entering a lock

In this research, the primary focus is to accurately simulate the unsteady hydrodynamic effects that occur during the process of a ship entering a lock. Due to the significant difference in shape between the ellipsoid and the ship, and the ellipsoid is submerged, this research also designed another experiment. Furthermore, to facilitate the verification and reproducibility of the experimental results, the research team deliberately chose a simple and well-defined object as the experimental subject. Consequently, a box-shaped object was selected as the prototype for the experiments. By analyzing and validating the experimental results, the researchers can ensure the accuracy and reliability of the subsequent numerical simulations. Furthermore, the extensive data collected during the experiments are intended to be made publicly available for other researchers in the field. This will enable them to independently verify the findings, replicate the experiments under different conditions, and draw meaningful comparisons with their own studies.

Table 5.2 shows the parameters of several typical vessels capable of navigating in the designed ship locks. For the convenience of model construction and to facilitate potential replication by other researchers, this research has chosen the Bulk carrier with the block coefficient (C_B) closest to 1 to simplify the ship hull into a box-like structure for experimentation and a 1/115 scale model is built. The specific model dimensions of the box and the lock can be found in Table 5.3.

Table 5.2: The parameters for ships that can be accommodated in the lock.

	Bulk carrier	8000 TEU ship	1200 TEU ship
$\boldsymbol{L_{OA}}$ (m)	282.6	348.5	369.2
$\boldsymbol{L_{pp}}$ (m)	277.2	328.5	348.0
$\boldsymbol{B}$ (m)	45.9	42.4	49.0
$\boldsymbol{T}$ (m)	15.0	14.4	15.2
$\boldsymbol{C_B}$ (-)	0.84	0.65	0.65
Number of blades	4	6	6
$\boldsymbol{D_p}$ (m)	7.41	8.38	9.40
$\boldsymbol{P/D_p}$ (-)	0.66	1.0	1.07
AEP (-)	0.63	0.96	1.03
Rudder area (m^2)	74.8	81.5	92.0

Table 5.3: Model information

Scale factor	Lock (MS)	Box (MS)
$\boldsymbol{L}$ (m)	3.5	2.4
$\boldsymbol{B}$ (m)	0.5	0.4
$\boldsymbol{T}$ (m)	0.225	0.15
$\boldsymbol{D}$ (m)	0.3	0.2

The model test results are based on captive model test results with the Third Set of lock chambers of the Panama Canal which have a length varying between 427m and 488m and a width of 55m (Delefortrie et al., 2009). This test was conducted in the towing tank of Kelvin Hydrodynamics Laboratory (KHL), which has the following dimensions: $76 \times 4.6 \times 2.5\ m^3$ (useful length, width and maximal depth), see KHL's official website for more detailed information on this facility.

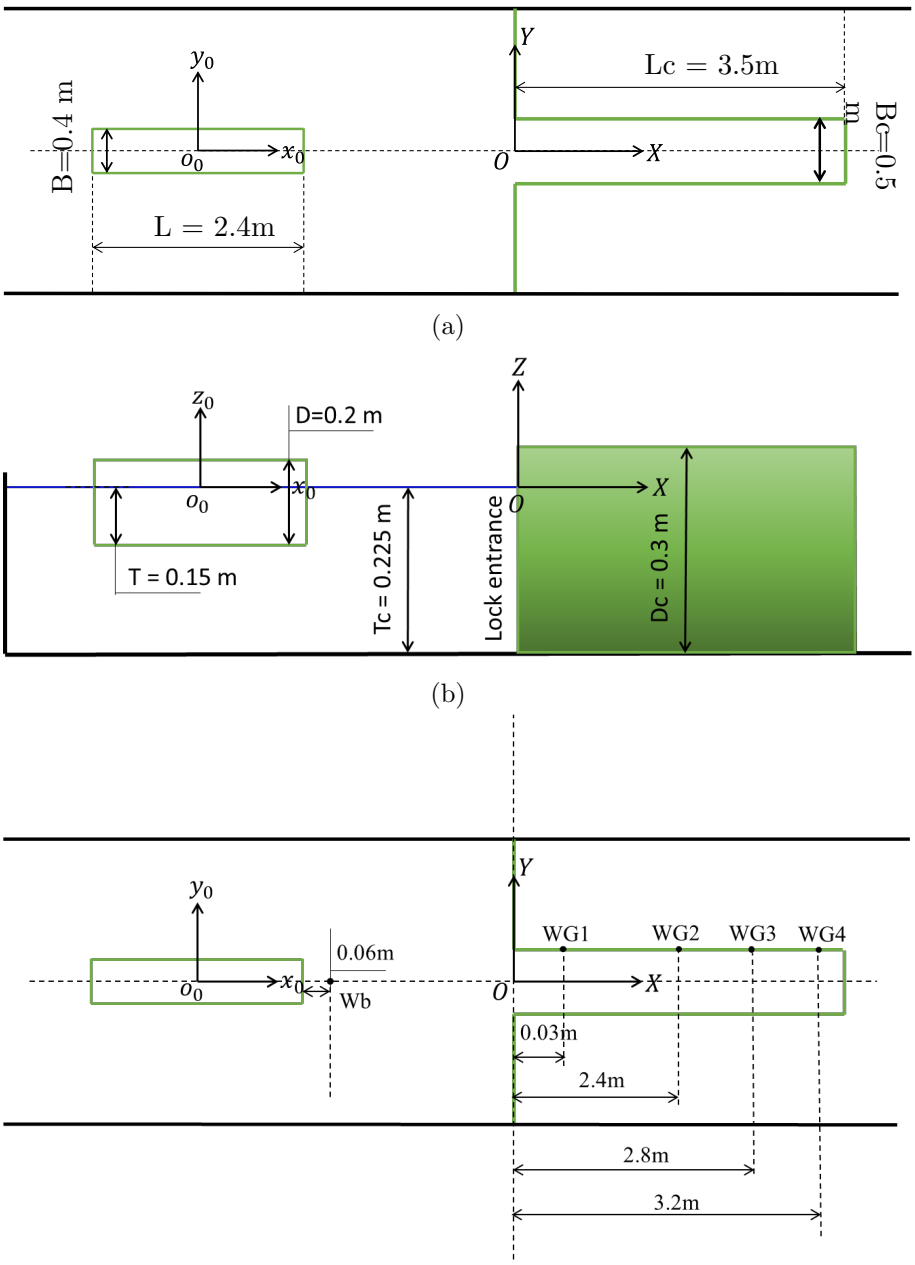

Figure 5.6: General layout of the towing tank for a box entering a lock and the positions of wave gauges. (a) Top view of the tank; (b) side view of the tank; (c) the positions of wave gauges.

Figure 5.6 shows the general layout of the tank with the position of the tank fixed coordinate system O-XYZ. The body-fixed coordinate system o_0-$x_0y_0z_0$, which travels

with the ship model, is also shown in Figure 5.6. Its origin is located amidships on the static water plane. In the tests, the box model is fixed in the all six degrees of freedom which means the sinkage and trim will be obtained from the force divided by the hydrostatic restoring force. The sinkage of the ship model was measured near the bow and the stern and then recomputed as midship sinkage and trim around the ship's origin. The same is true for the lateral force, which was measured near bow and stern and then expressed as a total sway force and yawing moment around the box's origin. The environment was installed by means of vertical plywood elements, sufficiently ballasted to ensure a watertight closure. Along the environment the water level variations have been measured using wave gauges located at 5 different positions, as shown in Figure 5.6c. The wave elevation in front of the bow of the box is recorded by an ultrasonic altimeter which move with the box together and the waves in the lock are measured by four fixed wave gauges.

Figure 5.7: Photograph of the experimental setups.

The box is fixed to the carriage with reinforced steel and gradually enters the pre-installed lock under the traction of the carriage, as shown in Figure 5.7. In addition, besides using the traditional wave gauge to measure wave elevations, this test innovatively adopts a new method that digitizes the free-surface points inside the

lock and records the motion of all nodes using a high-speed camera to achieve a complete reconstruction of the wave field within the lock. As shown in Figure 5.7, two cameras are installed in front of the lock model, and particles are scattered on the free surface within the lock to facilitate the identification of the nodes constituting the free surface from the acquired data.

Due to the unsteady nature of the test conditions, the reproducibility of the experiment is closely related to the acceleration phase of the box and the sudden narrowing of the channel. Especially when the box's acceleration starts at a relatively short distance from the lock entrance, the measured wave elevations inside the lock, particularly at the entrance, can be significantly affected. To avoid such a situation, the test is set to begin in calm water, and the position where acceleration starts is set at a distance of 12 meters from the entrance of the lock. This ensures that the box has sufficient distance to accelerate before reaching the entrance, minimizing the impact from the acceleration wave.

In the numerical modelling, the panels are distributed both on the free surface and, wetted body surface of the ship hull and the bank surface. Due to the symmetry of the computational domain and to save computational time, this research only constructed a numerical model for half of the computational domain. The other half was reflected using mirroring techniques in the numerical calculations. Similarly, the model of the bottom surface was not directly constructed; instead, it was treated as a mirrored surface for similar reasons, as shown in Figure 5.8. After conducting convergence studies, this research ultimately arranged 520 cells on the body surface, 2746 cells distributed across the free surface, and 1510 cells on the bank surface.

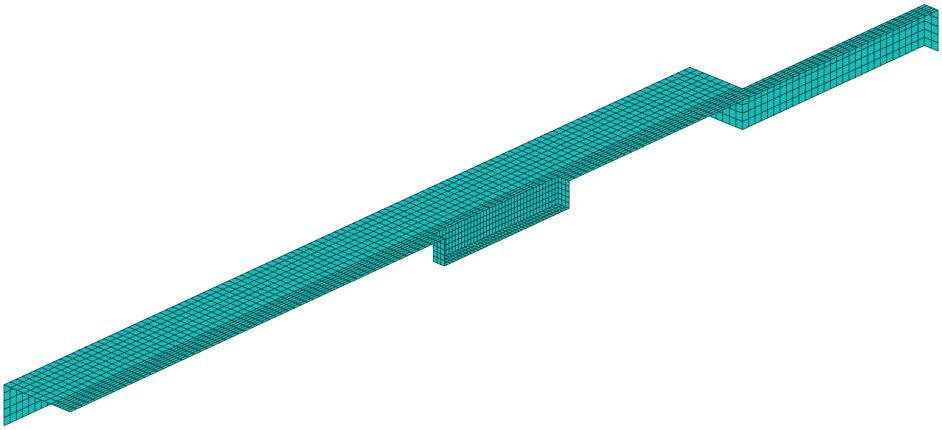

Figure 5.8: Panel distribution on the computation domain of a box entering a lock model.The computational domain is truncated at $3.5L$ upstream, $1L$ sideways and $3.5L$ downstream.

5.4 Results and discussion

In this chapter, the results obtained by MHydro will be compared with those from model experiments and CFD simulations to validate the accuracy of the MHydro method. As mentioned earlier, the model experiments were conducted at KHL, while the CFD results were provided by Dr. Terziev using STAR-CCM software. During the simulation, STAR-CCM took approximately 30,000 CPU hours, whereas MHydro, significantly faster, required only a few real hours. This substantial reduction in simulation time greatly improved efficiency.

5.4.1 A submerged ellipsoid entering a lock in deep water

Firstly, a validation is conducted by comparing the numerical results with the experimental measurement. Unfortunately, due to measurement accuracy issues, only the wave data of two fixed points in the global coordinate system were recorded in the experiment. As shown in Figure 5.3, the free surface elevations at two wave gauges are captured by both numerical (MHydro and CFD) and experimental (EFD) methods. It can be seen the agreement of these three methods is generally

satisfactory. Some oscillations are captured by the measurements before the ellipsoid enters the lock ($t/(L/U) < 0$) while they are not seen in the simulation results. A reasonable explanation is these oscillations are initiated at the acceleration stage while in the numerical simulation, a constant speed U is given at the first time step of simulation. The significant reduction in the oscillations observed at WG2 can support this assumption, as the accelerating waves constantly dissipate when they propagate forward. In addition to the oscillations prior to the initiation of the ellipsoid's entry into the lock, a minor oscillation is also observed in Figure 5.9a during the entering process. The underlying cause of this phenomenon will be elaborated upon in detail subsequently. It is also found that the numerical predictions at WG2 in Figure 5.9b is less satisfactory, particularly when the ellipsoid gradually entered the lock. This indicates that some nonlinear phenomena occur when the gap between the ellipsoid and the lock entrance is very small while the method employed in this chapter is linear and unsteady, which leads to deviations between the MHydro results and those obtained from CFD simulations and experiments.

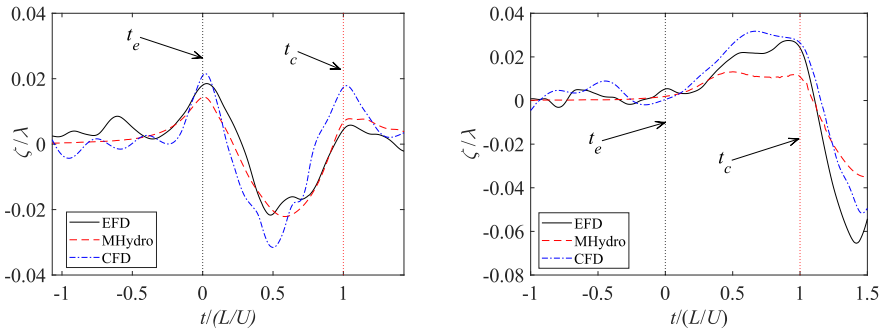

(a) (b)

Figure 5.9: Validation of free-surface elevations at Fr=0.136. λ is the wave length of the generated wave by the ellipsoid and X axis represents the position of the ellipsoid bow under the global coordinate system. (a) Free-surface elevation at WG1; (b) free-surface elevation at WG2.

Piston effect

Figure 5.10 illustrates the variation trend of the free surface inside the lock after the ellipsoid begins to enter. In this research, the water in the ship lock is considered

analogous to a sponge, and the entry of the ellipsoid compresses the "sponge," causing a rise in the overall free surface. From an energy perspective, during the entry process, the water "sponge" absorbs a portion of the ellipsoid's kinetic energy and converts it into gravitational potential energy, resulting in the rise of the free surface. However, water is not an actual sponge; it possesses fluidity. When the free surface rises to a certain height, the accumulated potential energy is released, causing return flow within the channel and lowering the elevation of the free surface. In this research, this motion is regarded as the piston effect. The movement of the "piston" within the gap represents an energy conversion process, so on a microscopic level, the water inside the lock can be visualized as numerous vertical slices being horizontally divided. Each slice can be considered as a spring, with the restoring force decreasing as it approaches the gate. Consequently, the amplitude of the free surface fluctuations also diminishes accordingly.

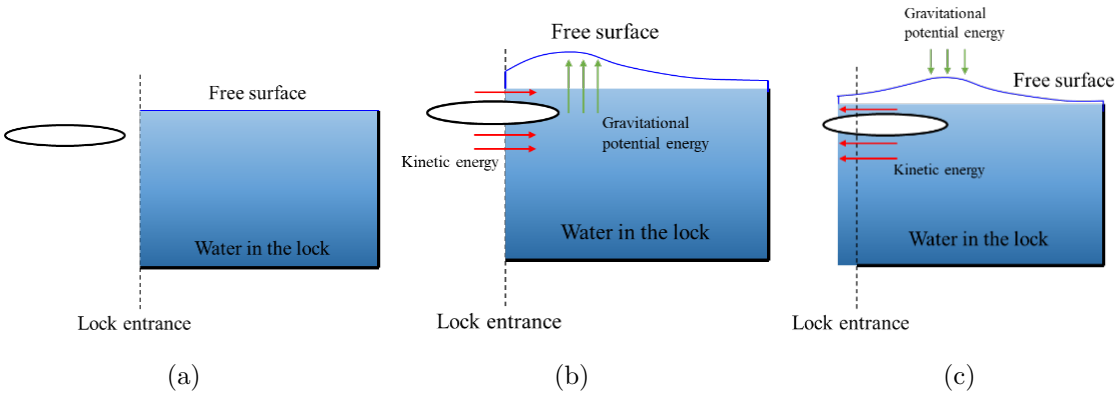

Figure 5.10: The schematic diagram of the variation of the free surface inside the lock during the ellipsoid entering the lock.

These speculations can be validated in Figure 5.11. Figure 5.11a shows the evolution of the waves in the centre line of lock, the x-axis represents the centre line of the lock at every specific moment, the y-axis represents the temporal progress of the ellipsoid entering the lock and the z-axis records the wave cut of each point on the centre line at the corresponding moment. For example, t_e, t_c, and t_d respectively represent the moments when the ellipsoid has just arrived the entrance of the lock, ellipsoid is totally in the lock and the ellipsoid is about to reach the lock gate, thus the three lines in Figure 5.11a respectively represent the wave cut on the centre line of the lock at the

aforementioned three corresponding moments. It can be seen, the free surface in the lock is very calm before t_e, however as soon as the ellipsoid arrives the lock entry, the waves in the lock are quickly built. As the ellipsoid gradually entered the lock, the free surface inside the lock began to undulate up and down and this phenomenon is well demonstrated by the wave elevation at Wave Gauge 3 (WG3). WG3 is used to record the time history of the waves at the end of the lock. Both the data of WG3 and the wave elevation at the ellipsoid bow in the body-fixed coordinate system are shown in Figure 5.11b. An obvious wave can be observed at WG3 after the start of entering. The same phenomenon can also be observed at the ellipsoid bow.

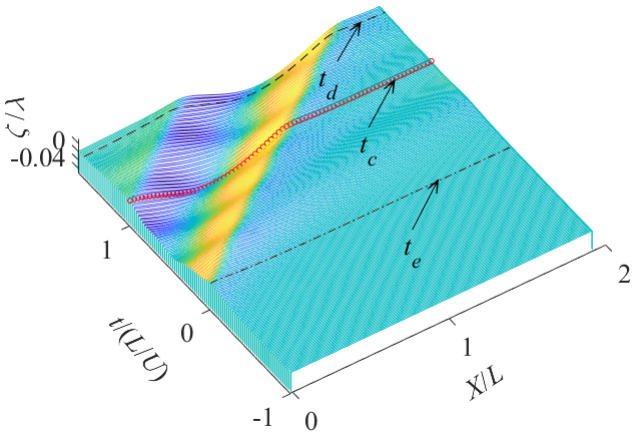

(a)

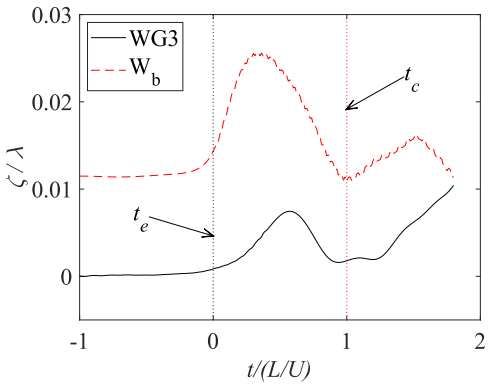

(b)

Figure 5.11: Waves evolution during the ellipsoid entering the lock at Fr=0.136. (a) Waterfall plot of wave cut in the centre line of lock; (b) free-surface elevation at WG3 and the ellipsoid bow.

Obviously, the piston motion in the lock is affected by the entering speed. To better study the piston, a higher speed case has been simulated. The wave elevations at five points in Figure 5.12 were recorded for research purposes and the detailed coordinates can be found in Table 5.4.

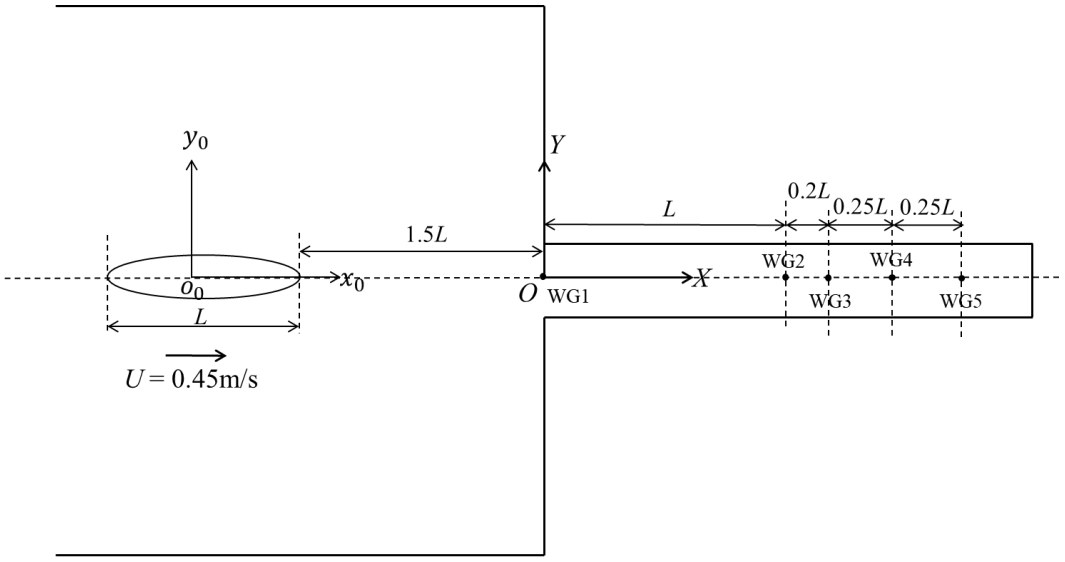

Figure 5.12: The positions of wave gauges.

Table 5.4: The position coordinates of wave gauges in the global coordinate system.

	X	***Y***	***Z***
WG1	0	0	0
WG2	0.5	0	0
WG3	0.6	0	0
WG4	0.725	0	0
WG4	0.85	0	0

Figure 5.13 shows the wave cuts in the lock of the high speed case. It can be seen, the entry of the ellipsoid generated the waves in the lock and a more detailed description of the piston motion in the lock is presented by the wave data at WG3, WG4, and WG5 in Figure 5.13b. As previously mentioned, piston motion causes the free surface of the water in the entire lock to rise and fall simultaneously. This phenomenon is clearly demonstrated in Figure 5.13b. After the entry of the ellipsoid ($t/(L/U) > 0$), the free surface at three points begins to rise simultaneously. This rise reaches its peak when approximately half of the ellipsoid has entered the lock ($t/(L/U) = 0.5$), after which a decrease is expected. Because of the piston effect, a low pressure field is created in the lock which results in the formation of a wave trough on the free surface after $t/(L/U) > 1$. Subsequently, as the ellipsoid gradually approached the three points one by one, the free surface at these locations was no longer determined by the piston effect, but by the pressure field at the ellipsoid bow, thus losing the characteristics of piston motion. However, the piston motion is not only reflected at the points near the end of the lock but can also be observed at the entrance of the lock.

However, it should be noted that the phenomenon of the free surface rising and falling simultaneously is not entirely synchronous. While the elevation changes of the free surface inside the lock are indeed a result of the piston effect, they are also influenced by variations in the pressure field caused by the forward motion of the ellipsoid. In fact, this research observe a slight time difference in the changes of the free surface at the three points depicted in Figure 5.13b. This difference is only evident because these three points are relatively close to each other, and the piston effect dominates at this time, making the discrepancy less noticeable.

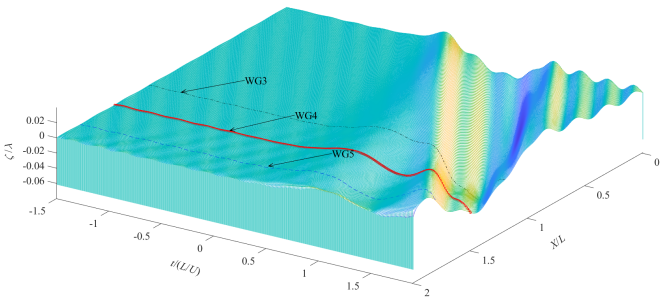

(a)

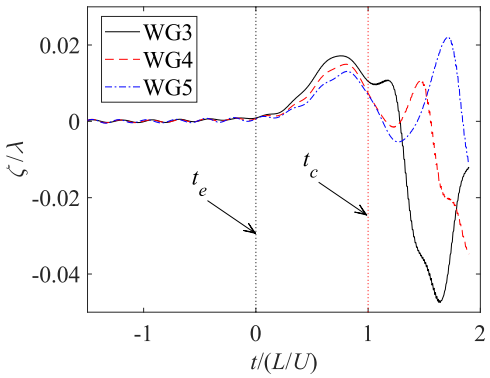

(b)

Figure 5.13: Wave cuts in the lock. (a) Waves evolution in the centre line of lock during the ellipsoid entering the lock at Fr=0.2; (b) free surface elevation at WG3, WG4 and WG5.

Additionally, the waves at WG1, WG2 and WG5 are also influenced by the piston effect. As shown in Figure 5.14a, due to its location at the entrance of the lock, the waves at WG1 are mainly dominated by the pressure field around the ellipsoid, so the characteristics of the waves here can be very different from those at other locations. However, even with such positioning, the piston effect is still evident. It can be seen from Figure 5.14a, the wave elevation at WG1 reaches its trough when approximately half of the ellipsoid has entered the lock ($t/(L/U)$=0.5). Thereafter, as shown in Figure 5.14b, a rising is expected due to the high pressure field located at the stern of the ellipsoid gets closer to the lock entrance. Interestingly, after a brief increase, the wave elevation at WG1 exhibit a decreasing trend again, which occurs almost

simultaneously with the decrease in wave elevation at WG2 and WG5. The research believes that this is because at this moment, the rise of the free surface inside the lock reaches its peak and begins to release stored gravitational potential energy, leading to the decrease at WG1. However, due to the presence of the high pressure field at the ellipsoid stern, this decrease is very short-lived, so the wave elevation at WG1 quickly resume its rapid upward trend. In conclusion, the phenomenon observed at WG1 is also caused by the piston effect.

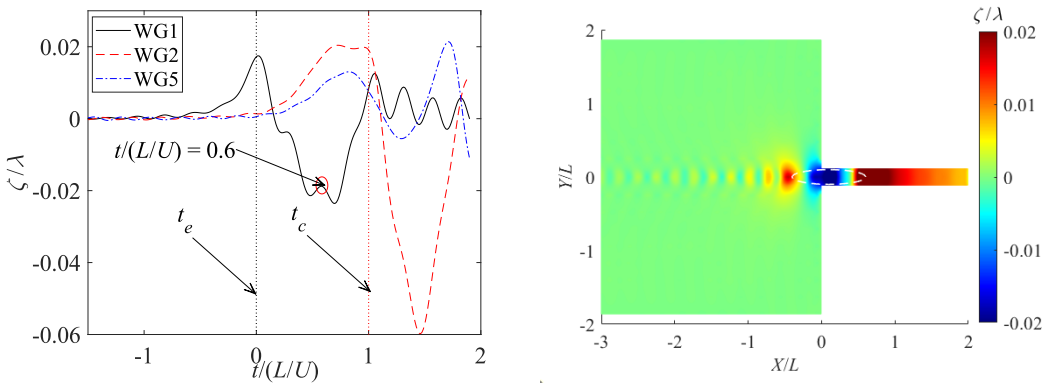

Figure 5.14: Wave cuts in the lock. (a) Free surface elevation at WG1, WG2 and WG5; (b) Wave field when $t/(L/U) = 0.6$.

Unsteady effect

Since this research considers that the piston effect is caused by the combination of the unsteady effect due to the sudden narrowing of the waterway and the obstruction of water by the closed lock gate, a steady case and a case with an open lock gate were simulated to prove this hypothesis. As shown in Figure 5.15a, the wave elevations at WG3, WG4 and WG5 are recorded to observe the fluctuation of the free surface inside the lock. It can be seen from Figure 5.15, in the steady case, except for slight fluctuations, the free surface at WG3, WG4 and WG5 remains calm between $t/(L/U) > 0$ and $t/(L/U) < 1$. Until the ellipsoid gradually approaches these positions, noticeable wave elevations are then observed. Obviously, in the steady case, the wave elevations at the selected points are completely dominated by the pressure

field around the ellipsoid, and there are no characteristics of piston motion. Therefore, it can be explicitly pointed out in this research that the piston effect is inseparable from the unsteady wave generated when the ellipsoid enters the lock. However, the results in Figure 5.15b seem to provide some different conclusions. Figure 5.15b depicts the situation when the lock gates remain open.

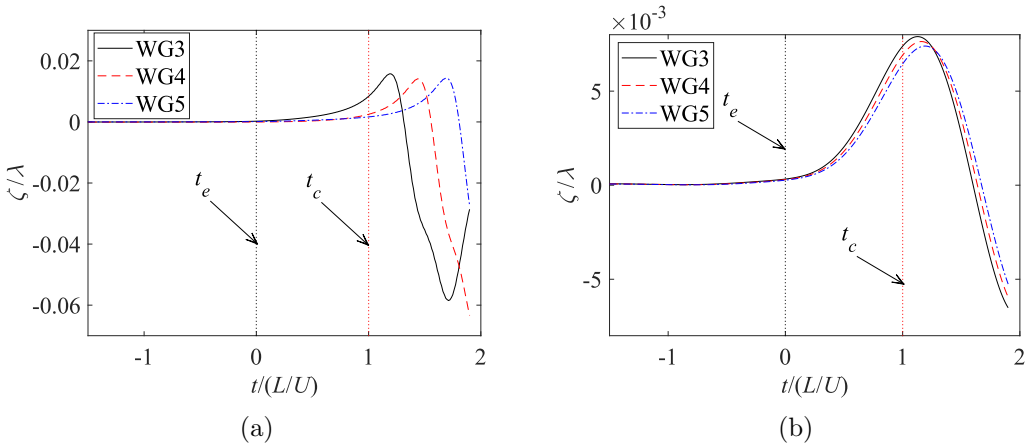

Figure 5.15: Free surface elevation at WG3, WG4 and WG5. (a) The steady case; (b) the case with lock gate opened.

In this case, it can be observed that the free surface at the three points begins to rise simultaneously after the ellipsoid starts to enter the lock ($t/(L/U) > 0$) and then begins to rapidly decline shortly after the ellipsoid is fully in the lock. At first glance, this phenomenon appears to be consistent with the definition of piston effect. However, upon closer examination, it is found that there is a slight time difference rather than complete synchronization in the wave elevations at the three points, both when they start to rise and when they begin to decline. The reason for this phenomenon is that the three points are too close to each other, causing their movements to appear very consistent.

To avoid the unrealistic compression of the free surface during the lock entry process caused by a too-short calculation domain, this research significantly extended the length of the lock and conducted a new simulation with the gates kept open, as shown in Figure 5.16a.

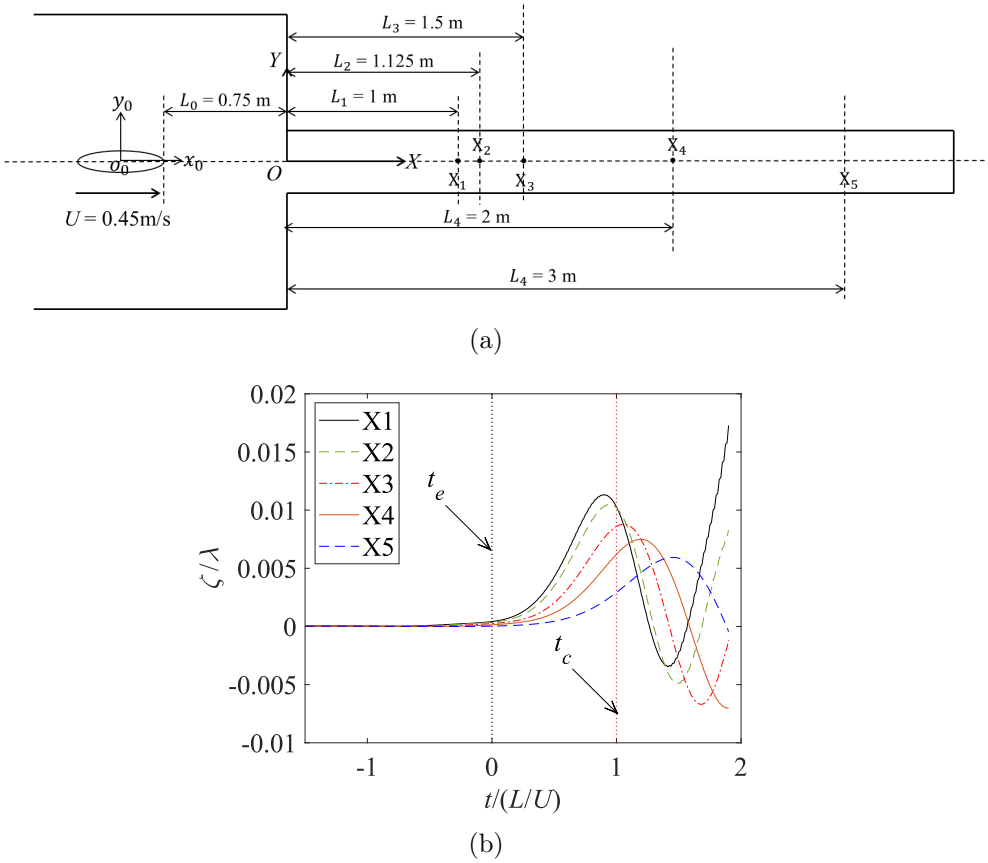

Figure 5.16: The case of the lock gate being kept open. (a) Positions where wave data are recorded; (b) wave cuts at the corresponding locations.

It can be observed from Figure 5.16b, a significant uplift can be observed on the free surface after $t/(L/U) > 0$, because the unsteady effect is considered in this case. However, these undulations no longer occur simultaneously but rather one by one as the ellipsoid approaches. In other words, due to the unsteady effect, a long unsteady wave is generated when the ellipsoid begins to enter the lock, and the variation of the free surface inside the lock, especially at the points far from the lock entrance, are caused by the propagation of this long wave. It is obvious that this kind of motion is different from the piston motion. Therefore, this piston motion can only be observed when the lock gate is closed. The existence of the lock gate stops the accelerated water particles keeping moving forward. The kinetic energy is converted into gravitational energy and then transformed into kinetic energy once again, causing a

rising and descending of the free surface as mentioned before.

Negative resistance effect

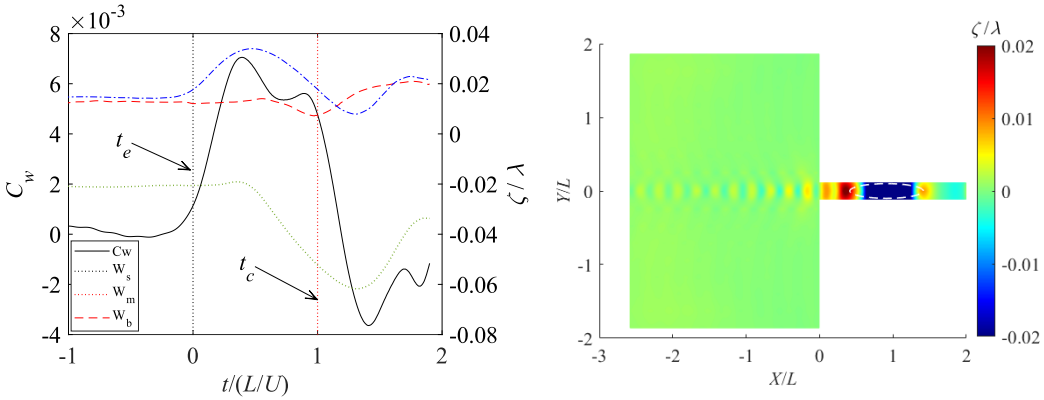

Figure 5.17: Free surface elevation and forces on the ellipsoid when it enters the lock at Fr=0.2. (a) Wave making resistance coefficient and free surface around the ellipsoid, where W_b represents the wave elevation at ellipsoid bow, W_m shows the wave change at the middle of the ellipsoid and W_s is the wave elevation at the ellipsoid stern; (b) wave field at $t/(L/U) = 1.41$ when the ellipsoid enters the lock at Fr=0.2.

It is also interesting to monitor the wave making resistance coefficient because it exhibited a negative value after the ellipsoid is totally in the lock ($t/(L/U) > 1$). This research believes that this is closely related to the wave field around the ellipsoid. As shown in Figure 5.17a, the wave making resistance quickly increases after the ellipsoid begins to enter the lock, which is consistent with the change in the wave field around the ellipsoid bow. Subsequently, as the wave elevation at the ellipsoid bow reaches its crest and begins to descend, the wave making resistance also decreases accordingly. However, when approximately half of the ellipsoid has entered the lock ($t/(L/U) = 0.5$), the wave field at the ellipsoid stern W_s begins to be affected by the suddenly narrower waterway. Therefore, the trend of W_s in Figure 5.17a is observed to be decreasing, which leads to a slight increase in the pressure difference between the bow and stern of the ellipsoid. This results in the appearance of a second peak in the wave making resistance. After $t/(L/U) > 1$, the wave elevation at the ellipsoid bow continues to decrease while the wave elevation at the stern keeps rising and

eventually intersects with the bow waves. This indicates the existence of a low pressure field at the ellipsoid bow due to the piston effect, while the stern exhibits a high pressure field. This pressure differential generates additional thrust for the ellipsoid, finally resulting in a negative value for the wave making resistance in Figure 5.17a. The wave field around the ellipsoid can also be more clearly observed in Figure 5.17b. In addition to the wave field, the pressure distribution on the ellipsoid can also be used to provide a good explanation for this phenomenon.

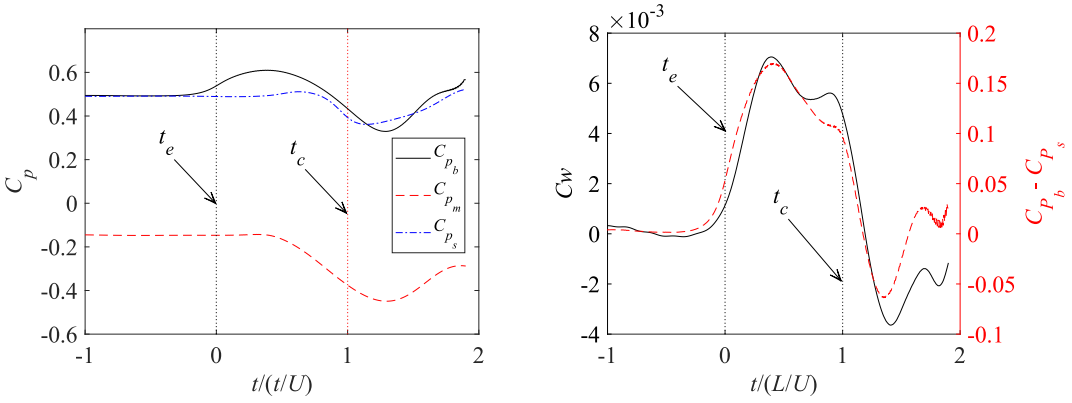

Figure 5.18: Wave making resistance and pressure around the ellipsoid when it enters the lock at Fr=0.2. (a) The pressure coefficient applied on the bow, middle and stern of the ellipsoid; (b) the wave making resistance of the ellipsoid and the pressure difference between the bow and stern of the ellipsoid.

As can be seen in Figure 5.18a, C_{P_b} and C_{P_s} respectively represents the pressure at the bow and stern of the ellipsoid. After the ellipsoid begins to enter the lock ($t/(L/U) > 0$), the pressure at the bow starts to increase, while the pressure at the stern begins to change after the ellipsoid has travelled halfway into the lock ($t/(L/U) > 0.5$). Up to this point, the pressure at bow is significantly greater than the pressure at the stern, therefore the wave making resistance is positive. However, as the ellipsoid continues to enter the lock, the pressure at the bow and stern begins to cross over, and for a certain period of time, the pressure at the bow even becomes greater than the pressure at the stern. As a result, the wave making resistance becomes negative. Therefore, this research believes that the pressure difference between the bow and stern of the ellipsoid can be used to explain the changes in wave making resistance very well. As shown in

Figure 5.18b, the trend of the pressure difference is highly consistent with the variation trend of the wave making resistance, which fully demonstrates the correctness of the previous explanation for the negative value appearing in the resistance.

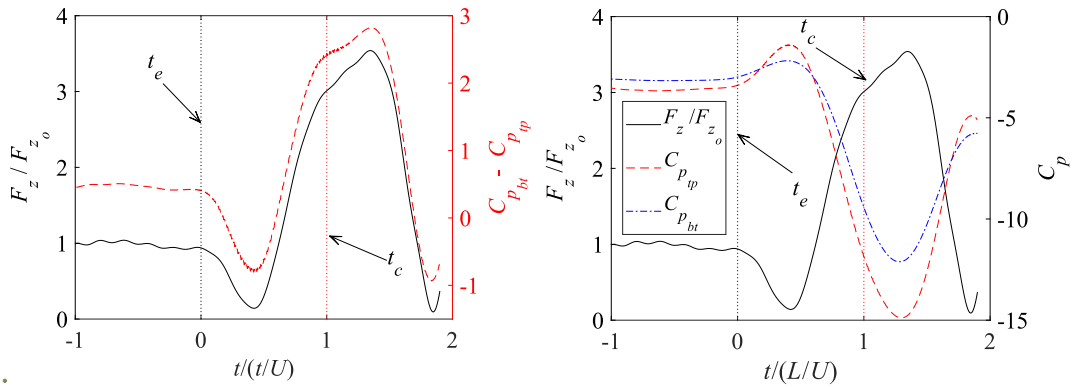

Figure 5.19: Vertical force nondimensionalized by the force at open water and the pressure acting on the the ellipsoid.

A similar approach can also be used to explain interesting findings related to the heave force. As shown in Figure 5.19a, the pressure difference between the top and bottom of the ellipsoid perfectly matches the variation in the vertical force acting on the ellipsoid. When the ellipsoid begins to enter the ship lock, the pressure difference appears as a negative value, which means that at this time, the pressure at the top of the ellipsoid is greater than that at the bottom, and the vertical force also shows a negative value accordingly. However, the more fundamental reason for this pressure field change is the variation in flow velocity. After the ellipsoid enters the lock, the rising free surface in the lock inhales water which means the water under the ellipsoid moves forward under the global coordinate system. It's like the moving speed of the ellipsoid is getting lower so a surprising drop of F_z is observed. The piston (free surface) then moves down and creates a returning flow at the bottom, which accelerates the entering speed. As a results, the vertical force increases. When the free surface starts to rise again, the vertical force falls. The pressure changes around the ellipsoid provide strong evidence for this hypothesis. Figure 5.19b shows the changes in the heave force applied on the ellipsoid, as well as the changes in the pressure field at the top and bottom of the

ellipsoid. It can be seen, after the ellipsoid begins to enter the lock ($t/(L/U) > 0$), the pressure starts to drop sharply. According to the Bernoulli's equation, this means that the flow velocity at the bottom of the ellipsoid increases, which is known as the phenomenon of stall in the ellipsoid. Then, the pressure at the bottom of the ellipsoid quickly increases, and the flow velocity slows down until the level of the free surface inside the lock reaches its peak again, at which point the trend reverses again.

5.4.2 A box entering a lock

As previously mentioned, in order to investigate the unsteady hydrodynamic phenomena during a ship entry into a lock, a box lock entry case was also subjected to model experiments and numerical simulations as part of this research.

Model experiment

The experiment consisted of five different velocity conditions, namely, U equals to 0.1 m/s, 0.15 m/s, 0.2 m/s, 0.25 m/s and 0.3 m/s. In this research, results from three sets of experiments conducted at velocities of $V = 0.1$ m/s,$V = 0.2$ m/s, and $V = 0.3$ m/s were compared. It can be seen in Figure 5.20a, the total resistance acting on the box exhibited a more pronounced stepwise increase with increasing box velocity. This phenomenon is likely attributed to the unsteady effect. As the box's velocity increases, a greater volume enters the lock per unit of time and the channel experiences a sudden constriction, resulting in a more significant unsteady effect. A more detailed proof will be provided in a subsequent section.

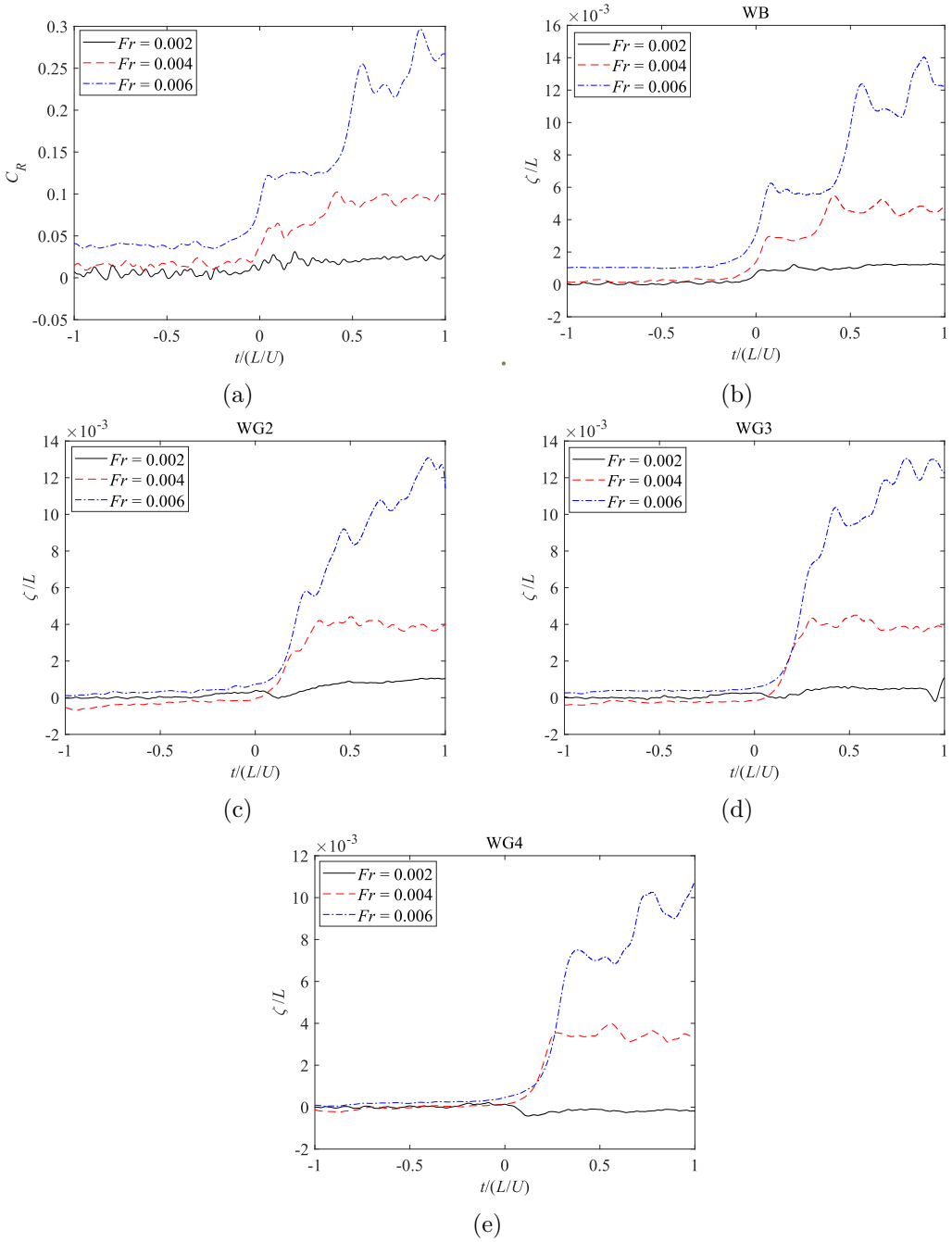

Figure 5.20: Results of the model experiments at different Froude Number where C_R is the dimensionless coefficient of the total resistance applied on the box. The x-axis represents both the dimensionless time and, simultaneously, the position of the bow of the box throughout the entire process of it entering the lock. When $t/(L/U) = 0$, the bow of the box has just reached the entrance of the lock.

The way in which the wave at the bow changes aligns with the variations in total resistance, which is understandable since in this problem, the pressure field at the bow of the box plays a dominant role.

Regarding the waves within the lock, as shown in Figure 5.20c to Figure 5.20e, as the velocity increases, larger waves are generated at WG2, WG3, and WG4, and the entire free surface rises at a faster rate.

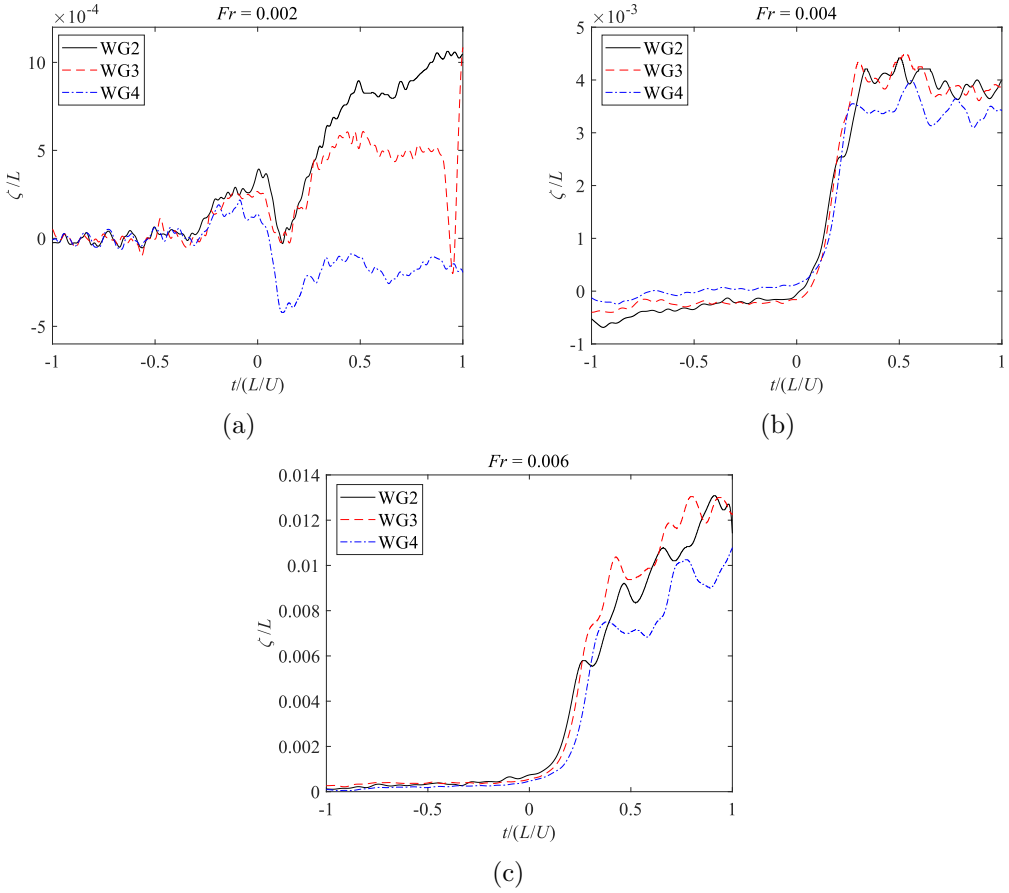

Figure 5.21: Wave elevations in the lock at different Froude Number.

After comparing the waves generated by the box within the lock at different velocities which are presented in Figure 5.21 , it was found that the expected piston effect is not pronounced at a velocity of 0.1 m/s, where the influence of viscosity on the fluid should be emphasized. As the velocity increases, a noticeable simultaneous rise in the free surface within the lock is observed, followed by sustained oscillations at the higher level. However, a simultaneous drop in the free surface is still not reflected in the

experimental results. This is because in this experiment, the distance between the lock banks and the sides of the box is too small, limiting the fluid's ability to flow from both sides of the lock to the outside. If the velocity continues to increase, this situation should improve.

Validation of the numerical simulation

Firstly, a preliminary validation of the simulation results will be conducted in this section. The model experiment with a velocity of 0.3 m/s has been selected as a case study, not only because at this velocity, the elevation of the free surface inside the lock is more pronounced, but also because the data from this set of experiments has been validated through five repeated trials, as shown Figure 5.22.

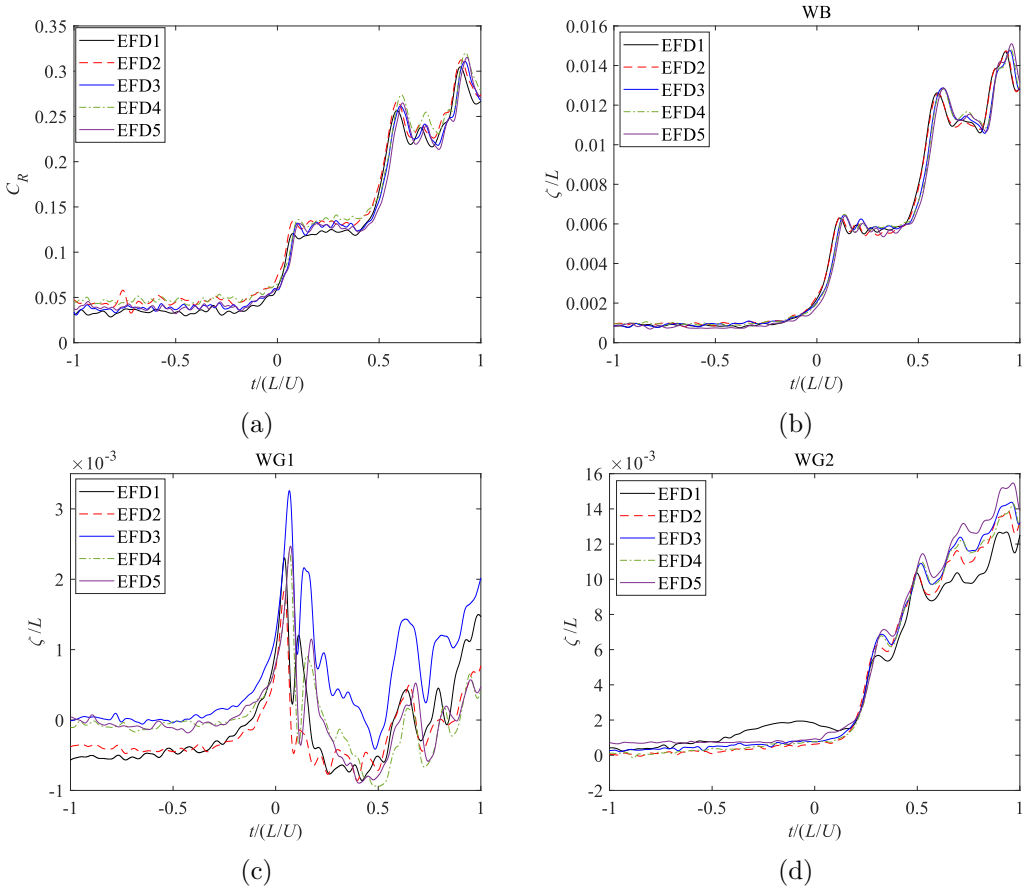

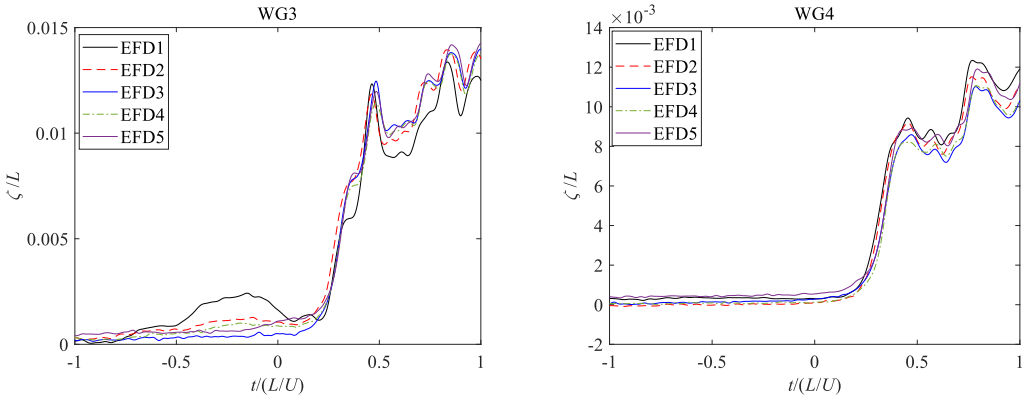

(e) (f)

Figure 5.22: Repetitions of the Model Experiment when $U = 0.3$ m/s.

Similarly, the numerical results provided by MHydro in this section will be compared with those from CFD simulations and experimental data.

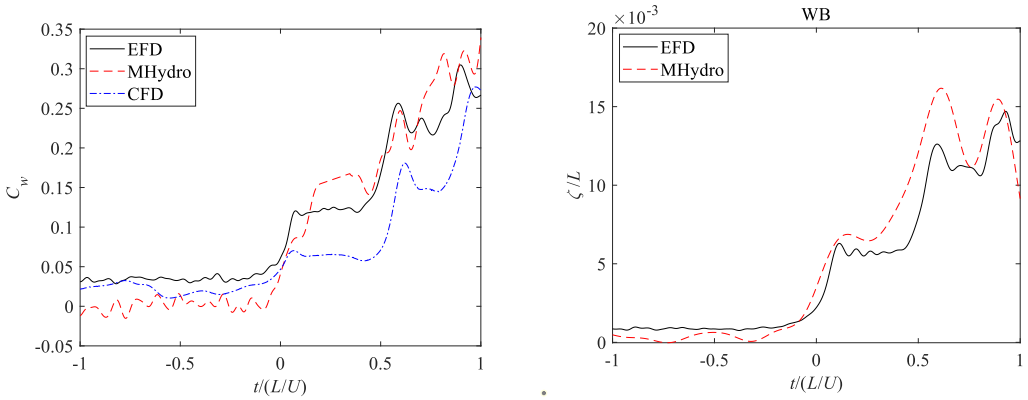

(a) (b)

Figure 5.23: Comparison of the surge force applied on the box and the wave elevation at the bow while F_r=0.06 where the results from EFD and CFD are total resistance and MHydro' result is wave making resistance.

As shown in Figure 5.23a, both numerical simulation methods successfully capture the trend of the surge force variation when the box starts entering the lock. However, compared to the CFD method, MHydro does not fully capture many fine details. In the initial stage, there is a gap between the results obtained from MHydro and the experimental results. This is because MHydro can only provide the wave making

resistance experienced by the box during its forward motion, while the experimental results account for the total resistance. The difference arises from the neglect of frictional forces in the simulation process. At this stage, the Froude number (Fr) is low (Fr=0.06) which means the box's velocity is very low. As a result, the frictional resistance dominates the total resistance during this phase.

Another piece of evidence supporting this observation is presented in Figure 5.23b, which illustrates that MHydro reasonably captures the wave elevation at the bow of the box during the lock entry process. However, it is regrettable that due to the limitations of CFD in providing results in the body-fixed coordinate system, the comparison of simulation results at WB can only be accomplished between EFD and MHydro. As can be seen, the experimental results exhibit three distinct steps, occurring at $t/(L/U)$ equal to 0.2, 0.5, and 0.75. Similarly, the numerical simulation results also reflect this trend quite well, although the positions of the steps are slightly different.

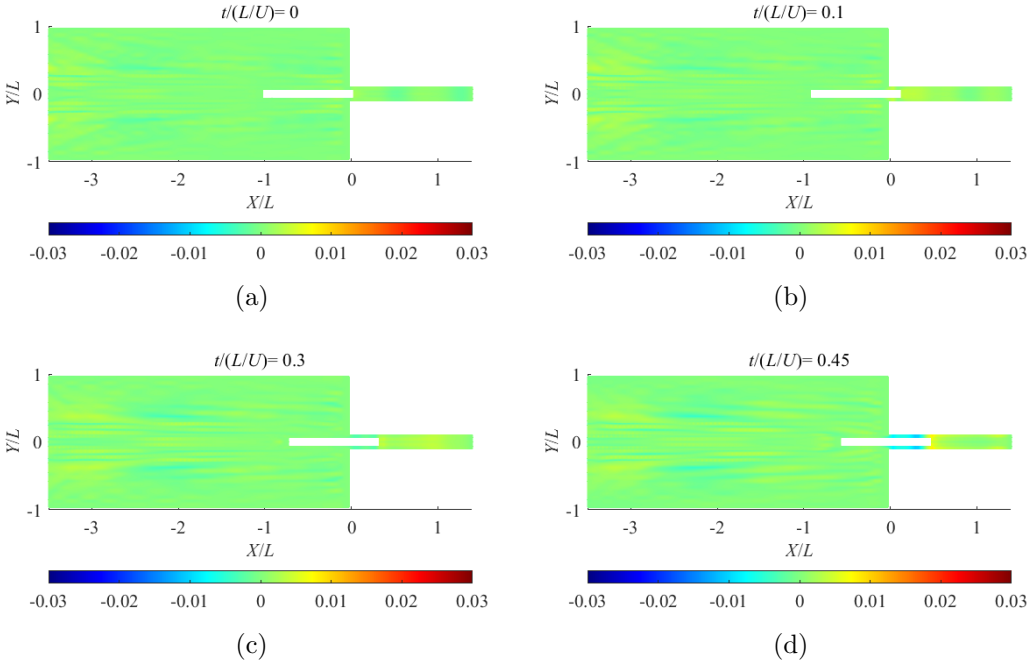

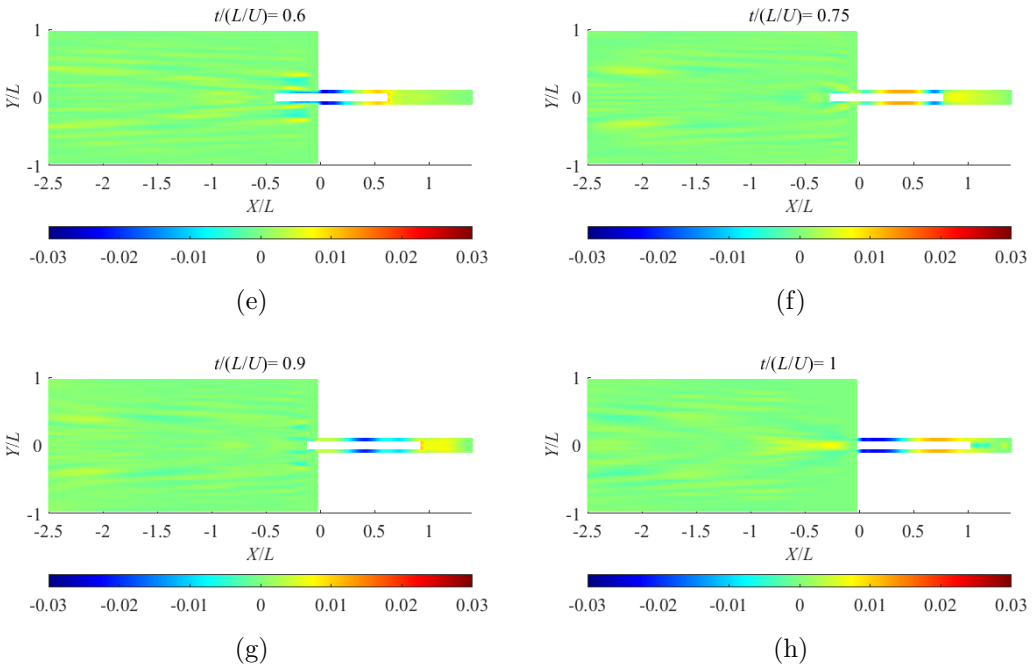

Figure 5.24: The wave field in the lock when the box is entering the lock, where the color bar represents ζ/L.

Finally, Figure 5.24 displays the wave field within the lock during the box's entry process. From this, it can be directly observed that the elevation of the bow waves undergoes three distinct transitions, occurring approximately at $t/(L/U)$ equal to 0.1, 0.6, and 0.9.

Figure 5.25 illustrates the validation of the predicted wave heights within the lock, the location of the wave guages can be found in Figure 5.25e. The simulation results from MHydro generally exhibit good agreement with the EFD results, wave elevations' oscillations are also well reflected in the predictive results, although certain details remain unaccounted for. In contrast, the results obtained from CFD are in excellent agreement up to $t/(L/U) <= 0.6$. However, beyond this moment, the experimental results exhibit a stable trend, while CFD predictions continue to rise.

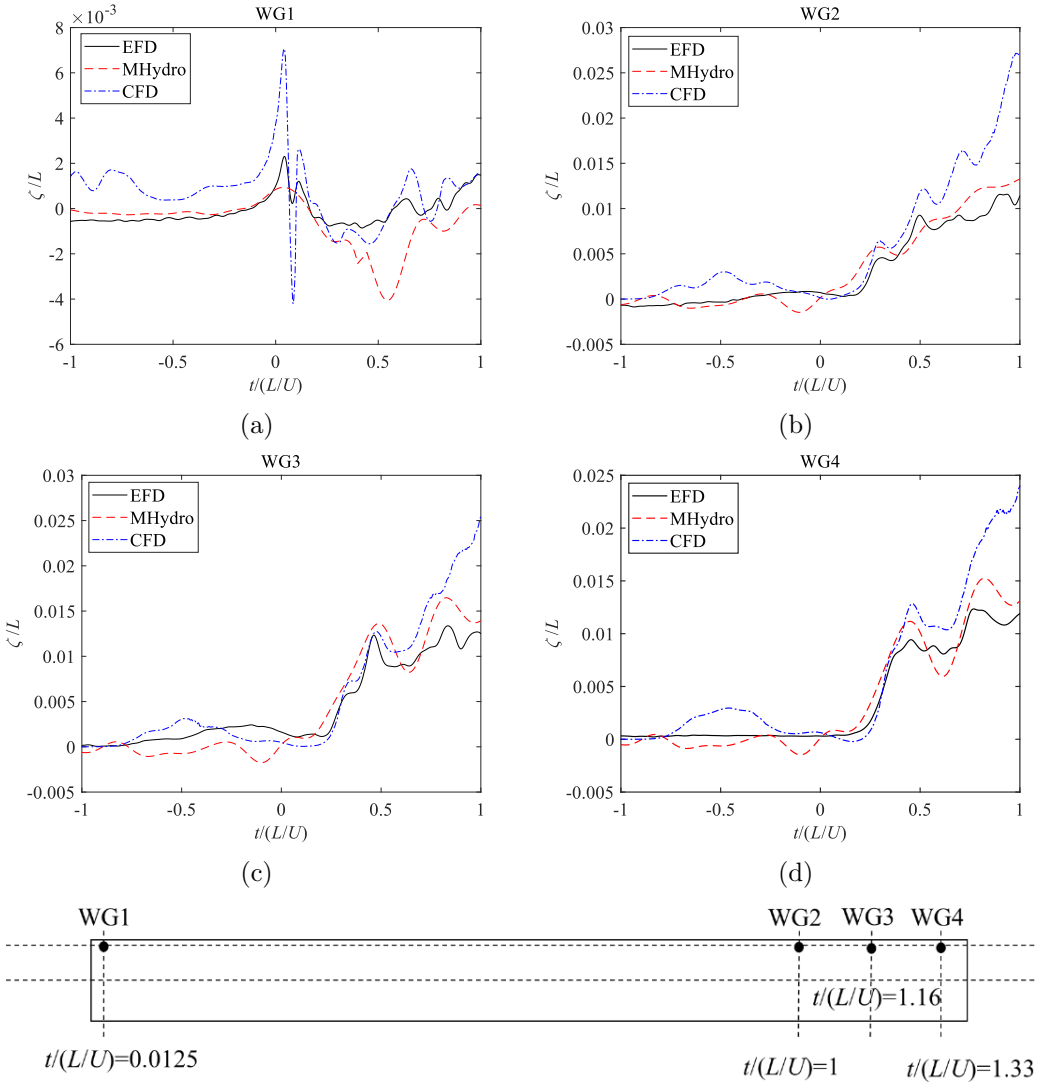

Figure 5.25: Comparison of the wave elevations in the lock while F_r=0.06.

It can be observed that initially, as the box just begins to enter the lock, there is a relatively small change in the volume of fluid within the lock ($t/(L/U) <= 0.2$). Consequently, there is no significant variation in the free surface. Subsequently, as the box continues to enter, the box's kinetic energy is converted into gravitational potential energy, leading to a rapid rise in the free surface. As mentioned in the previous section, after reaching its highest level, the gravitational potential energy is reconverted into

kinetic energy, resulting in the outflow of fluid from the lock and a subsequent overall decrease in the free surface. However, this phenomenon was not observed in this case. When $t/(L/U) = 0.45$, the free surface inside the lock reaches its highest level and then continues to oscillate at that location. This indicates that at this moment, the kinetic energy absorbed and lost by the fluid has reached a balance so the height of the free surface no longer shows significant changes.

Return flow effect

Due to the sudden narrowing of the waterway, when the box enters, it not only elevates the free surface height within the lock but also induces significant return flow inside the lock. This return flow has a substantial impact on the results. As shown in Figure 5.26, most of the hydrodynamic phenomena within the lock are primarily attributed to the presence of return flow. When the return flow is not considered in the simulation (κ=0), there is almost no noticeable change in the free surface within the lock. However, wave resistance is closely related to the wave elevations, and as a result, the prediction of wave making resistance is completely distorted under this condition.

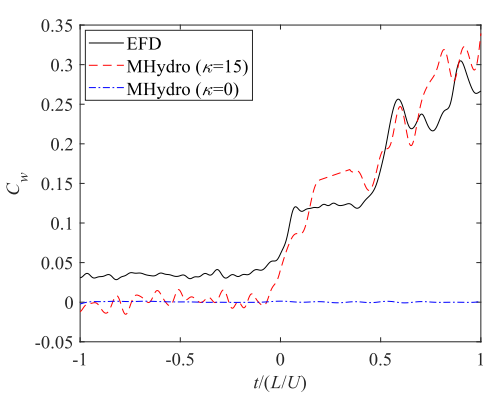

(a)

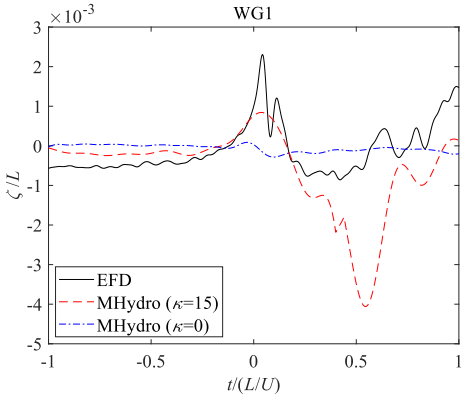

(b)

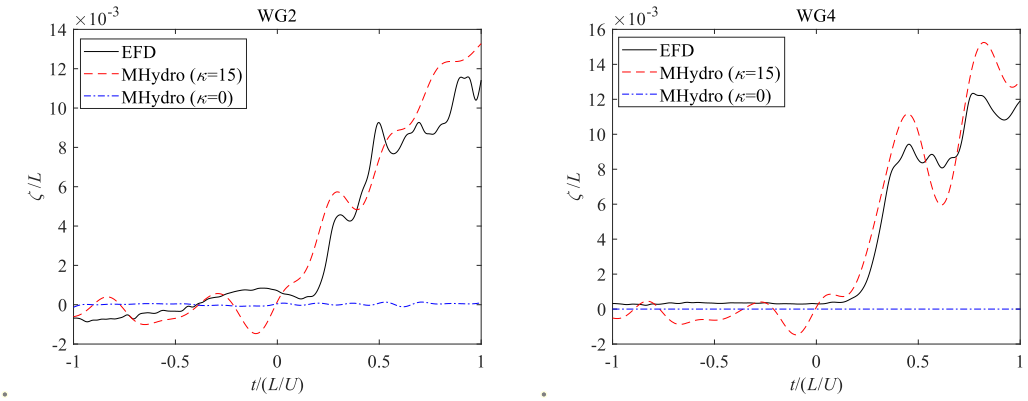

(c) (d)

Figure 5.26: Comparison of the numerical simulation results with different acceleration coefficient κ while F_r=0.06.

Moreover, it is noteworthy that the research conducted in this thesis has unveiled that the return flow within the lock is not uniform. Fluid in proximity to the bow of the box is frequently subject to more pronounced effects of return flow, in contrast to positions nearer to the banks. This can be attributed to the box's entry, which serves as the primary instigator of the return flow phenomenon. Consequently, the flow field around the bow, which moves in tandem with the box, naturally exhibits a more pronounced correlation with the return flow, compared to the free surface at fixed positions located at a distance from the box.

Free surface effect and piston effect

Figure 5.27 presents a comparison of the total resistance and wave making resistance with different method. It can be observed that the numerical simulation results progressively approach the experimental results, starting from treating the free surface as a rigid wall, then establishing a linear quasi-steady free surface, and finally incorporating the unsteady effects on the free surface. Notably, the step phenomena observed in the experimental results are only visible in the fully unsteady simulation results, indicating a close association with unsteady effects. This explains why the step phenomena become more pronounced only as the box's velocity increases. A

higher entry velocity will induce more significant unsteady effects on the free surface within the lock.

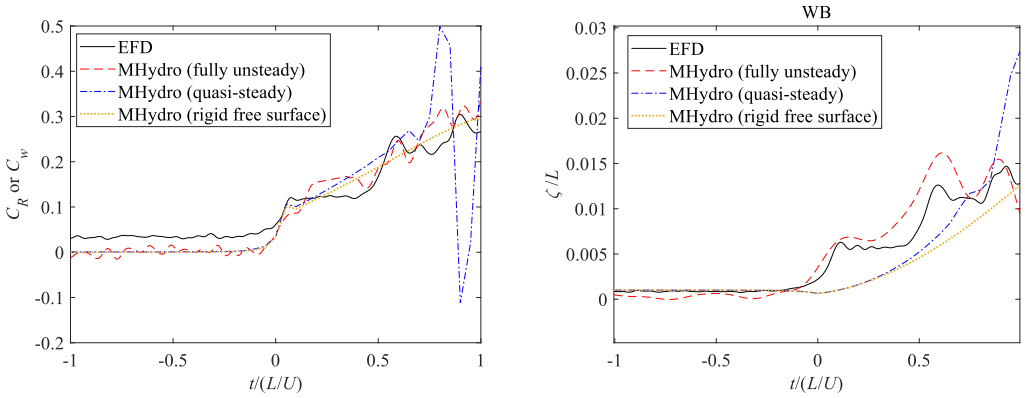

(a) (b)

Figure 5.27: Resistance applied on the box obtained by different methods. As before, the results from EFD provides the total resistance C_R, while the results from MHydro only include the wave making resistance C_w.

The wave elevations inside the lock further demonstrate the necessity of establishing a 3D free surface and considering its unsteadiness in the current problem, as illustrated in Figure 5.28.

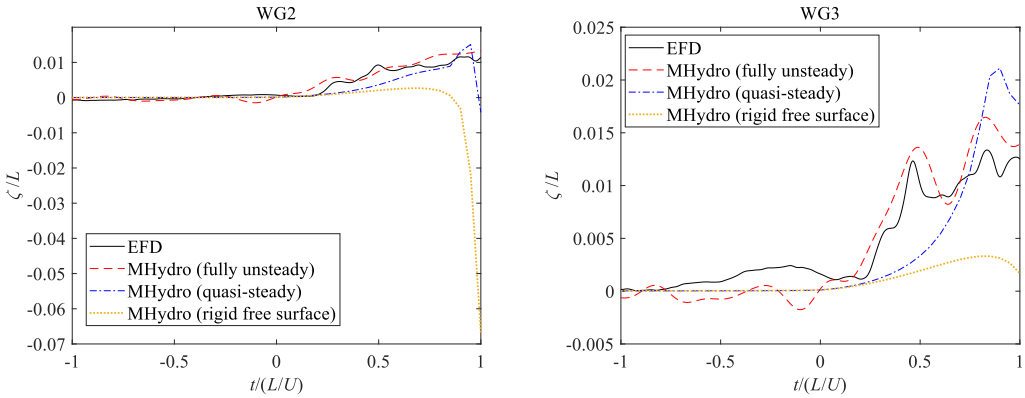

(a) (b)

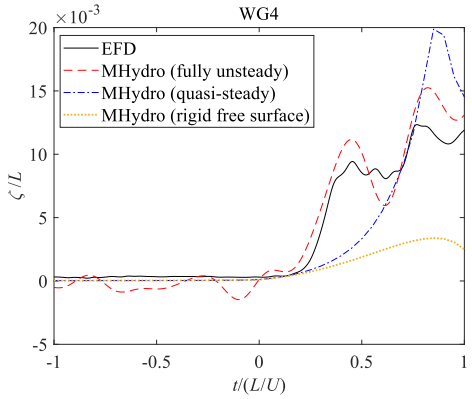

(c)

Figure 5.28: Wave elevations inside the lock.

Furthermore, this research also reveals that the unsteady effects of the free surface are indispensable for simulating the piston phenomenon inside the lock. When the free surface effects are completely disregarded, the free surface inside the lock only rises sequentially as the bow of the vessel approaches, influenced by the high-pressure field. However, when a linear quasi-steady free surface is established, although the free surface inside the lock can also rise simultaneously, the entire process follows a smooth curve rather than the abrupt lift observed in the experiments as the box enters. Only the results obtained using the fully unsteady MHydro method effectively replicate this phenomenon, as shown in Figure 5.29.

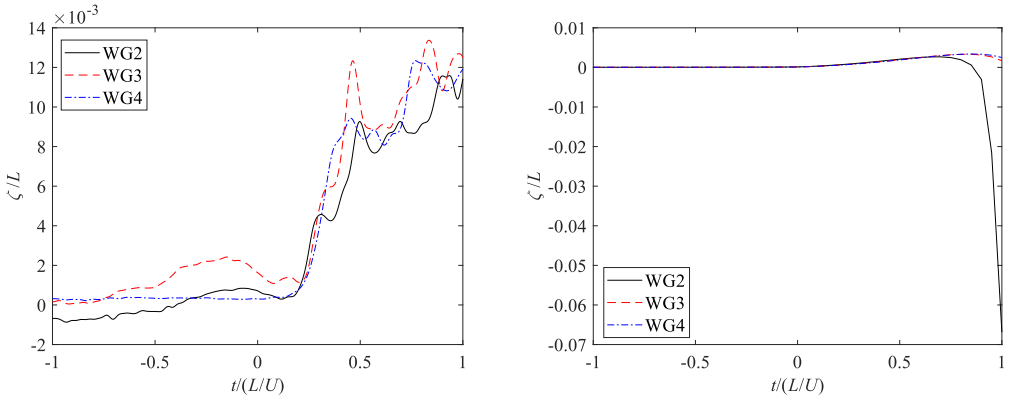

(a) (b)

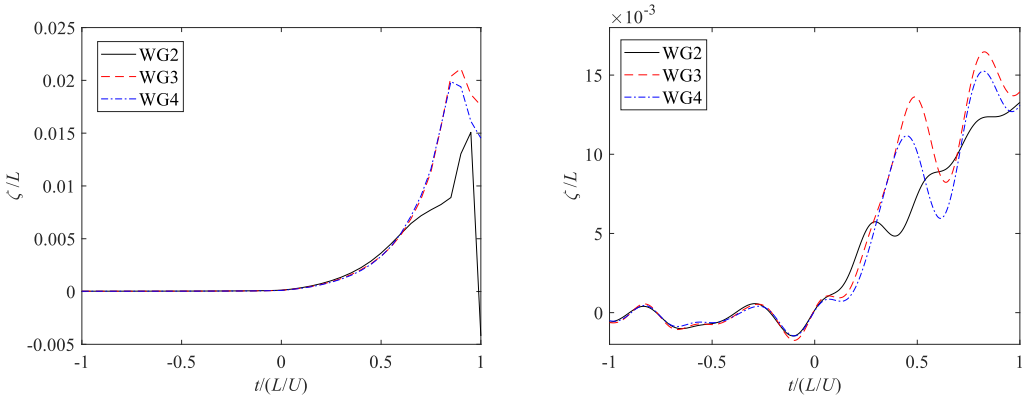

(c) (d)

Figure 5.29: Wave elevations at WG2, WG3 and WG4. (a) EFD results; (b) results with a rigid free surface; (c) results with a quasi-stady free surface; (d) results with a fully unsteady free surface.

However, as previously mentioned, it is regrettable that the free surface level did not exhibit a clear simultaneous decrease phenomenon in the current case. Nevertheless, it can still be observed that there are some such trends in the changes of waves at WG3 and WG4. As shown in Figure 5.29a and Figure 5.29d, from $t/(L/U) = 0.5$ to $t/(L/U) = 0.8$, the wave elevations at both of the two locations underwent a process of initial decrease followed by an increase, and this change occurred simultaneously. The reason for this phenomenon lies in the energy conversion, which has been explained previously. Additionally, from an external perspective, it is also due to the relatively greater flow space at these two points, as they are farther from the lock entrance, enabling the lowering of the free surface.

5.5 Summary

In the current research, the potential flow solver, MHydro, is extended to handle unsteady problems and applied it to the ship-lock scenario. Through the research mentioned in Chapter 4, It's pleasing to discover the existence of a piston phenomenon in the process when an ellipsoid entering a lock, where the free surface rises and falls simultaneously. This phenomenon is closely related to the unsteady

effects during lock entry and the closing of the lock gate. Further more, the piston effect is also closely related to the speed of the ellipsoid. When the speed is higher, the unsteady effects also increase, leading to a more pronounced piston effect. This research also found an interesting phenomenon known as negative resistance. This is due to the rising of free surface (or due to piston effect) at the front of the ellipsoid, which makes the bow pressure higher. Because of the piston effect, the free surface starts to fall after X/L=1. It creates a low pressure field in the lock, sucking the ellipsoid to move towards the lock. That is why a negative wave-making resistance is observed after the ellipsoid is completely in the lock.

During the simulation and comparison of the results of the box entry into the lock, it's found that MHydro can generally capture the forces acting on the box during lock entry and the trends of wave generation. However, there are still deficiencies in its ability to predict many detailed aspects accurately. While MHydro provides a good overall trend, it may not fully capture all intricacies and complexities involved in the flow dynamics during the lock entry process. The limitations in accurately capturing the detailed flow behaviors during lock entry are attributed to the inadequacy of the return flow model used in this research The return flow within the lock is non-uniform, leading to some inaccuracies in the simulation results. Improving the model will be a crucial task for the author's future work.

Finally, in the case of the box entry into the lock, a pronounced piston effect was not observed. This is attributed to the narrow gap between the box, the lock walls, and the bottom, which significantly restricts the fluid motion. However, it should be noted that the absence of the piston effect in this specific case does not imply that the phenomenon does not exist during lock entry. In fact, the piston effect is closely related to the ratio of the wetted cross-sectional area of the ship to the wetted cross-sectional area of the lock, as well as the entry velocity. Further research is needed to investigate the influence of these factors on the occurrence and magnitude of the piston effect during ship-lock interactions.

Chapter 6

Conclusions and Future work

The primary objective of the work presented in this thesis is to study the steady and unsteady wave generated by a single body and multi-bodies travelling in deep and shallow water. The main achievements against the objectives are outlined below:

6.1 Unsteady hydrodynamics of an accelerating ships in open water area

The hydrodynamic behavior of a vessel undergoing sustained acceleration in shallow water is investigated using the 3D-Rankine source method based on potential flow theory and linear unsteady free surface conditions. In the numerical simulation, the effects of gravity acceleration and water depth on the results are explored, and a comprehensive study is conducted on the issue of past the critical transition.

This research find results showed excellent agreement in the low and high-speed range, past the critical transition, indicating that the resistance in that range is linear and dominated by unsteady rather than nonlinear terms. A point near but less than F_h=1 was identified for both water depths modelled where all acceleration intensities cross, creating an intersection point. The existence of this point was explained through the proximity of the trans-critical boundary and the fact that no steady flow is possible when the depth Froude number is unity. Before the critical speed, wave-making resistance is directly proportional to acceleration. Once the speed

exceeds the critical speed ($F_h > 1$), the relationship becomes inversely proportional. This interesting phenomenon provides valuable guidance for energy-saving considerations during ship navigation.

Although this research has confidence in the results presented herein in view of the agreement between the two solvers, experimental data of trans-critically accelerating ship resistance would be invaluable in demonstrating the exact level of accuracy. In addition, models of trans-critical acceleration in fully confined water are of particular interest since the blockage ratio would also be an important parameter. Such cases are also interesting because the trans-critical range can occupy a significant portion of the depth Froude number depending on the blockage (Lataire et al., 2012a).

Furthermore, the impact of added mass on accelerating vessels has not been explicitly addressed in this thesis. In fact, due to the adopted free surface formulation and constraints on vessel motion, the effects of added mass are absent or cannot be isolated for individual analysis in this research. Future objectives will encompass refining current methodologies for extracting the added mass term and integrating the vessel's six-degree-of-freedom motion into the simulation.

Finally, based on the comparison between the results obtained from the two solvers, this research is highly confident in the proposed findings and conclusions. However, the experimental data on resistance for cross-critical accelerated vessels remains invaluable in validating the accuracy of the numerical simulation results. Moreover, the model for cross-critical acceleration in fully pressurized water is particularly intriguing, as the blockage ratio is also a significant parameter. Investigating the issue of cross-critical acceleration for vessels in restricted waterways will also be one of the key focuses for future research.

6.2 Ship passing problem in confined water area

Based on the research of Yuan (2019), this research introduces unsteady effects into the study of ship passing problems and employs a real-time updating grid generation method to ensure that the free surface grid aligns with the boundaries of the

computational domain at each time step. After comparing with experimental results, this research concludes that the potential flow solver MHydro can accurately predict the hydrodynamics acting on the moored ship. Additionally, by constructing a fully unsteady free surface, the oscillations of forces and waves induced by far-field waves are also successfully captured.

Unfortunately, in simulating the unsteady bank problem, the research method employed in this research, while able to reasonably predict the trends in variation of the hydrodynamic forces acting on the ship, wave elevations in the channel, and flow velocities on the seabed, consistently underestimates these quantities when compared to experimental results. This discrepancy can be attributed partly to the absence of the initial acceleration phase in the simulations and partly to the influence of viscosity. However, by employing the fully unsteady approach, the same sustained oscillations observed in the experimental results were captured. This further underscores that these oscillations are a result of the unsteadiness in the free surface.

Although accurate numerical simulation results require higher mesh density, which pose challenges to computer computational power and time consumption, this research still presents an improved tool for computing and analyzing unsteady multi-body and unsteady bank problems.

However, it should be noted that the simulation of the ship passing problem in this research is based on the premise that one of the ships is moored and does not have any forward speed. At this point, the moored ship can be treated as a type of bank. However, when both ships have forward speeds, the problem becomes much more complex. Due to the unsteady nature of the method used in the thesis, it is necessary to ensure that the correspondence between the cells on the free surface and the ship's hull is consistent at each time step. This becomes challenging when the two ships have different sailing speeds since there are two body-fitted coordinate systems. Resolving this issue requires the authors to implement the transformation between Eulerian coordinates and Lagrangian coordinates on the free surface grid, and this matter will be a subject of future research.

6.3 Ship-lock problem

The unsteady numerical simulation algorithm has been developed to investigate the unsteady wave generated by a ship in unsteady bank problem. In this research, there are two cases included, one is an submerged ellipsoid entering a lock in deep water and the other is a box entering a lock in shallow water.

In the case of the ellipsoid, the thesis is delighted to announce the discovery that when the ellipsoid begins to enter the lock, the free surface inside the lock exhibits a phenomenon called "piston motion," characterized by simultaneous rising and falling motions. This phenomenon is primarily related to the unsteady effects occurring when the ellipsoid enters the ship lock. When neglecting the unsteady effects, the free surface inside the lock would only experience a continuous rise under the influence of the pressure field at the bow of the ellipsoid, and there would be no occurrence of any downward motion. Indeed, this is also why the piston phenomenon is closely correlated with the speed of the ellipsoid entering the ship lock. Higher speeds imply more pronounced unsteady effects, leading to a more distinct piston motion. As the velocity increases, the impact of unsteady effect becomes more apparent, resulting in a clearer manifestation of the piston phenomenon. Furthermore, this piston phenomenon is also related to the presence of the closed gate, as they restrict the fluid flow within the lock. When the gate is opened, the entry of the ellipsoid will only generate a continuous propagating long wave inside the lock, without exhibiting the piston motion.

Another intriguing phenomenon observed is that the ellipsoid experienced negative wave-making resistance at certain moments. This is due to the rising of the free surface at the front of the ellipsoid, causing higher pressure at the bow. As a result of the piston effect, the free surface begins to descend after X/L=1. It generates a low-pressure field inside the lock, attracting the ellipsoid towards the lock. That's why it is observed that there is a negative wave-making resistance after the ellipsoid is fully locked in place.

Finally, the simulation and research on the box entering the lock demonstrate that MHydro can provide a good prediction of the forces acting on the box during the

lock entry process and the trends of wave generation inside the lock. However, due to the inaccuracies in the return flow model, some details may be lost. Moreover, it is regrettable that no significant piston-like phenomenon was observed in the experimental data for the box entering the lock.

In conclusion, this research suggests that further research is necessary to elucidate the relationship between the piston phenomenon and the ratio of the cross-sectional area of the ship's wetted area to that of the ship lock. The consideration of nonlinear effects in the free surface should also be part of future work. In fact, this isn't overly challenging; it simply involves extending the already employed three-level difference scheme from time domain to the space domain. Additionally, the impact of vessel speed on this phenomenon needs to be explored. Moreover, accurately simulating the return flow generated inside the ship lock and overcoming the limitations imposed by the current use of acceleration coefficients will be challenging tasks.

Bibliography

Andrun, M., Blagojević, B., and Bašić, J. (2019). The influence of numerical parameters in the finite-volume method on the wigley hull resistance. *Proceedings of the Institution of Mechanical Engineers, Part M: Journal of Engineering for the Maritime Environment*, 233(4):1123–1132.

Barratt, M. (1965). The wave drag of a hovercraft. *Journal of Fluid Mechanics*, 22(1):39–47.

Bašić, J., Blagojević, B., and Andrun, M. (2020). Improved estimation of ship wave-making resistance. *Ocean Engineering*, 200:107079.

Beck, R. F., Newman, J. N., and Tuck, E. O. (1975). Hydrodynamic forces on ships in dredged channels. *Journal of Ship Research*, 19(03):166–171.

Calisal, S. (1977). Effect of initial acceleration on ship wave pattern and wake survey methods. *Journal of Ship Research*, 21(04):239–247.

Day, A. H., Clelland, D., and Doctors, L. J. (2009). Unsteady finite-depth effects during resistance tests on a ship model in a towing tank. *Journal of marine science and technology*, 14:387–397.

Delefortrie, G., Willems, M., Laforce, E., Vantorre, M., De Mulder, T., De Regge, J., and Wong, J. (2008). Tank test of vessel entry and exit for third set of panama locks. In *The Proceedings of the International Navigation Seminar following PIANC AGA 2008, China Communications Press*, pages 517–530.

Delefortrie, G., Willems, M., Vantorre, M., and Laforce, E. (2009). Behavior of post

panamax vessels in the third set of panama locks. In *International Conference on Marine Simulation and Ship Maneuverability (MARSIM'09)*. Panama Canal Authoritiy; International Marine Simulator Forum.

Doctors, L. J. (1975). The experimental wave resistance of an accelerating two-dimensional pressure distribution. *Journal of Fluid Mechanics*, 72(3):513–527.

Doctors, L. J. (1993). On the use of pressure distributions to model the hydrodynamics of air-cushion vehicles and surface-effect ships. *Naval Engineers Journal*, 105(2):69–89.

Doctors, L. J., Day, A. H., and Clelland, D. (2008). Unsteady effects during resistance tests on a ship model in a towing tank. *Journal of ship research*, 52(04):263–273.

Doctors, L. J. and Sharma, S. D. (1972). The wave resistance of an air-cushion vehicle in steady and accelerated motion. *Journal of Ship Research*, 16(04):248–260.

Feldman, J. (1972). Transcritical shallow water flow past slender ships.

Flagg, C. and Newman, J. (1971). Sway added-mass coefficients for rectangular profiles in shallow water. *Journal of Ship Research*, 15(04):257–265.

Fujino, M. (1968). Experimental studies on ship manoeuvrability in restricted waters. *International Shipbuilding Progress*, 15(168):279–301.

Ghassemi, H. and Yari, E. (2011). The added mass coefficient computation of sphere, ellipsoid and marine propellers using boundary element method. *Polish Maritime Research*, 18(1):17–26.

Gourlay, T. P. and Tuck, E. (2001). The maximum sinkage of a ship. *Journal of Ship Research*, 45(01):50–58.

Grue, J. (2017). Ship generated mini-tsunamis. *Journal of Fluid Mechanics*, 816:142–166.

Haussling, H. and Van Eseltine, R. (1978). Waves and wave resistance for air-cushion vehicles with time-dependent cushion pressures. *Journal of Ship Research*, 22(03):170–177.

Havelock, T. (1909). The wave-making resistance of ships: a theoretical and practical analysis. *Proceedings of the Royal Society of London. Series A, Containing Papers of a Mathematical and Physical Character*, 82(554):276–300.

Havelock, T. (1949). The resistance of a submerged cylinder in accelerated motion. *The Quarterly Journal of Mechanics and Applied Mathematics*, 2(4):419–427.

Havelock, T. H. (1908). The propagation of groups of waves in dispersive media, with application to waves on water produced by a travelling disturbance. *Proceedings of the Royal Society of London. Series A, Containing Papers of a Mathematical and Physical Character*, 81(549):398–430.

Hess, J. L. and Smith, A. M. O. (1964). Calculation of nonlifting potential flow about arbitrary three-dimensional bodies. *Journal of ship research*, 8(04):22–44.

Javanmard, E., Mansoorzadeh, S., and Mehr, J. A. (2020). A new cfd method for determination of translational added mass coefficients of an underwater vehicle. *Ocean Engineering*, 215:107857.

Jiang, T., Henn, R., and Sharma, S. D. (2002). Wash waves generated by ships moving on fairways of varying topography. In *24th Symposium on Naval Hydrodynamics, Fukuoka, Japan*, pages 441–457.

Jin, Y., Chai, S., Duffy, J., Chin, C., Bose, N., and Templeton, C. (2016). Rans prediction of flng-lng hydrodynamic interactions in steady current. *Applied Ocean Research*, 60:141–154.

Johnson, J. W. (1957). Ship waves in navigation channels. *Coastal Engineering Proceedings*, (6):40–40.

Kevorkian, J. and Yu, J. (1989). Passage through the critical froude number for shallow-water waves over a variable bottom. *Journal of Fluid Mechanics*, 204:31–56.

Lataire, E., Delefortrie, G., and Vantorre, M. (2016). Impact of banks on ship squat. In *4th MASHCON*, pages 115–121. Bundesanstalt für Wasserbau.

Lataire, E., Vantorre, M., and Delefortrie, G. (2009). Captive model testing for ship to ship operations. In *International Conference on Marine Simulation and Ship Maneuverability (MARSIM'09)*. Panama Canal Authoritiy; International Marine Simulator Forum.

Lataire, E., Vantorre, M., and Delefortrie, G. (2012a). A prediction method for squat in restricted and unrestricted rectangular fairways. *Ocean Engineering*, 55:71–80.

Lataire, E., Vantorre, M., Delefortrie, G., and Candries, M. (2012b). Mathematical modelling of forces acting on ships during lightering operations. *Ocean Engineering*, 55:101–115.

Lea, G. K. and Feldman, J. P. (1972). Transcritical flow past slender ships. In *9th Symposium on Naval Hydrodynamics, Washington DC, USA*, pages 1527–1542.

Lee, B. W. and Lee, C. (2019). Equation for ship wave crests in the entire range of water depths. *Coastal Engineering*, 153:103542.

Li, M., Yuan, Z.-M., and Yeung, R. W. (2020). Unsteady wave-making resistance of an accelerating ship. In *International Conference on Offshore Mechanics and Arctic Engineering*, volume 84379, page V06AT06A020. American Society of Mechanical Engineers.

Lunde, J. (1951). On the linearized theory of wave resistance for deplacement ships in steady and accelerated motion. In *Norwegian Ship Model Experiment Tank, Technical University of Trondheim, Norway, Meddelelse Nr. 5, Presented at: Summer Meeting of The Society of Naval Architects and Marine Engineers, SNAME Transactions, Washington DC, Volume 59, pp. 25-85.*

Lunde, J. K. (1957). The linearized theory of wave resistance and its application to ship shaped bodies in motion on the surface of a deep, previously undisturbed fluid. *Norwegian Ship Model Experiment Tank, Technical University of Trondheim,*

Norway, Meddelelse Nr. 23, Presented at The Society of Naval Architects and Marine Engineers, SNAME, Washington DC, Technical and Research Bulletin No. 1-18.

Molland, A. F., Turnock, S. R., and Hudson, D. A. (2017). *Ship resistance and propulsion*. Cambridge university press.

Mousaviraad, S. M., Sadat-Hosseini, S. H., Carrica, P. M., and Stern, F. (2016a). Ship–ship interactions in calm water and waves. part 2: Urans validation in replenishment and overtaking conditions. *Ocean engineering*, 111:627–638.

Mousaviraad, S. M., Sadat-Hosseini, S. H., and Stern, F. (2016b). Ship–ship interactions in calm water and waves. part 1: analysis of the experimental data. *Ocean engineering*, 111:615–626.

Newman, J. N. (2018). *Marine hydrodynamics*. The MIT press.

NTSB (1991). *Marine Accident Report: Explosion and Fire aboard the U.S. Tank-ship Jupiter, Bay City, Michigan, September 16, 1990.* National Transportation Safety Board.

Pinkster, J. A. (2004). The influence of a free surface on passing ship effects. *International Shipbuilding Progress*, 51(4):313–338.

Quadvlieg, F., S. F. S. C. D. O. J. F. (2014). Workshop on verification and validation of ship manoeuvering simulation methods (simman 2014). pages 1–563.

Redekopp, L. and You, Z. (1995). Passage through resonance for the forced korteweg–de vries equation. *Physical review letters*, 74(26):5158.

Remery, G. (1974). Mooring forces induced by passing ships. In *Offshore technology conference*, pages OTC–2066. OTC.

Sakamoto, N., Wilson, R. V., and Stern, F. (2007). Reynolds-averaged navier-stokes simulations for high-speed wigley hull in deep and shallow water. *Journal of Ship Research*, 51(03):187–203.

Schoenherr, K. (1960). Data for estimating bank suction effects in restricted water and on merchant ship hulls. In *First Symposium on Ship Maneuverability*, pages 199–210.

Shebalov, A. (1970). Theory of ship wave resistance for unsteady motion in still water. *The University of Michigan, Department of Naval Architecture and Marine Engineering, College of Engineering, Translated by: Michail Aleksandrov.*

Sian, A. Y., Maimun, A., and Ahmed, Y. (2016). Simultaneous ship-to-ship interaction and bank effect on a vessel in restricted water. In *4th International Conference on Ship Manoeuviring in Shallow and Confined Water.*

Söding, H., Hamburg-Harburg, T., Conrad, F., and Potsdam, S. (2005). Analysis of overtaking manoeuvres in a narrow waterway. *Ship Technology Research*, 52(4):189–193.

Sun, X., Yan, X., Wu, B., and Song, X. (2013). Analysis of the operational energy efficiency for inland river ships. *Transportation Research Part D: Transport and Environment*, 22:34–39.

Terziev, M., Liu, Y., Yuan, Z., and Incecik, A. (2023). The resistance of a trans-critically accelerating ship in shallow water. *Ship Technology Research*, pages 1–19.

Terziev, M., Tezdogan, T., Demirel, Y. K., Villa, D., Mizzi, S., and Incecik, A. (2021a). Exploring the effects of speed and scale on a ship's form factor using cfd. *International Journal of Naval Architecture and Ocean Engineering*, 13:147–162.

Terziev, M., Tezdogan, T., and Incecik, A. (2021b). Modelling the hydrodynamic effect of abrupt water depth changes on a ship travelling in restricted waters using cfd. *Ships and Offshore Structures*, 16(10):1087–1103.

Tezdogan, T., Incecik, A., and Turan, O. (2016). A numerical investigation of the squat and resistance of ships advancing through a canal using cfd. *Journal of marine science and technology*, 21:86–101.

Torsvik, T., Dysthe, K., and Pedersen, G. (2006). Influence of variable froude number on waves generated by ships in shallow water. *Physics of Fluids*, 18(6):062102.

Tuck, E. (1964). A systematic asymptotic expansion procedure for slender ships. *Journal of Ship Research*, 8(03):15–23.

Tuck, E. (1978). Hydrodynamic problems of ships in restricted waters. *Annual Review of Fluid Mechanics*, 10(1):33–46.

Tuck, E. O. (1966). Shallow-water flows past slender bodies. *Journal of fluid mechanics*, 26(1):81–95.

Tuck, E. O. (1967). Sinkage and trim in shallow water of finite width, schiffstechnik bd. 14. *Heft*, 73:92–94.

Tuck, E. O. and Newman, J. (1976). Hydrodynamic interactions between ships. In *Symposium on Naval Hydrodynamics, 10th, Proceeding, Pap and Discuss, Cambridge, Mass, June 24-28, 1974.*, number Proceeding.

Tuck, E. O. and Taylor, J. P. (1970). Shallow wave problems in ship hydrodynamics. In *8th Symposium Naval Hydrodynamics*, pages 627–659.

Tunaley, J. K. (2014). Ship wakes in shallow waters. *LRDC Rep*, 6.

Van Zwijnsvoorde, T., Delefortrie, G., and Lataire, E. (2022). Passing ship effects in shallow and confined water: Open model test data for validation purposes. In *Proceedings of the 6th MASHCON International Conference on Ship Manoeuvring in Shallow and Confined Water, Glasgow, UK*, pages 22–26.

Vantorre, M. and Delefortrie, G. (2013). Behaviour of ships approaching and leaving locks: Open model test data for validation purposes. In *3rd International Conference on Ship Manoeuvring in Shallow and Confined Water: with non-exclusive focus on Ship Behaviour in Locks*, pages 1–16. Flanders Hydraulic Research.

Vantorre, M. and Richter, J. (2011). Maneuverability in lock access channels,". In *What's new in the design of navigation locks" 2nd International Workshop, PIANC–New Orleans, 13-14 Sept. 2011, Paper 6*, volume 2.

Vantorre, M., Verzhbitskaya, E., and Laforce, E. (2002). Model test based formulations of ship-ship interaction forces. *Ship Technology Research*, 49:124–141.

Varyani, K. and Krishnankutty, P. (2006). Modification of ship hydrodynamic interaction forces and moment by underwater ship geometry. *Ocean engineering*, 33(8-9):1090–1104.

Wakaba, L. and Balachandar, S. (2007). On the added mass force at finite reynolds and acceleration numbers. *Theoretical and Computational fluid dynamics*, 21(2):147–153.

Wang, Q. (2007). An analytical solution for two slender bodies of revolution translating in very close proximity. *Journal of Fluid Mechanics*, 582:223–251.

Wang, S. (1975). Dynamic effects of ship passage on moored vessels. *Journal of the Waterways, Harbors and Coastal Engineering Division*, 101(3):247–258.

Wehausen, J. V. (1961). Effect of the initial acceleration upon the wave resistance of ship models. Technical report, CALIFORNIA UNIV BERKELEY BERKELEY.

Xiang, X. and Faltinsen, O. M. (2011). Maneuvering of two interacting ships in calm water. *Marine Systems & Ocean Technology*, 6:65–73.

Xu, H., Zou, Z., Zou, L., and Liu, X. (2016). Unsteady hydrodynamic interaction between two cylindroids in shallow water based on high-order panel method. *Engineering Analysis with Boundary Elements*, 70:134–146.

Yao, J.-x. and Zou, Z.-j. (2010). Calculation of ship squat in restricted waterways by using a 3d panel method. *Journal of Hydrodynamics*, 22(1):472–477.

Yeung, R. W. (1975). Surface waves due to a maneuvering air-cushion vehicle. *Journal of Ship Research*, 19(04):224–242.

Yeung, R. W. (1978). On the interactions of slender ships in shallow water. *Journal of Fluid Mechanics*, 85(1):143–159.

Yuan, Z.-M. (2019). Ship hydrodynamics in confined waterways. *Journal of ship research*, 63(01):16–29.

Yuan, Z.-M., Incecik, A., and Jia, L. (2014). A new radiation condition for ships travelling with very low forward speed. *Ocean Engineering*, 88:298–309.

Yuan, Z.-M., Kellet, P., Incecik, A., Turan, O., and Boulougouris, E. (2015). Ship-to-ship interaction during overtaking operation in shallow water. *Journal of Ship Research*, 59(03):172–187.

Yuan, Z.-M., Li, L., and Yeung, R. W. (2019). Free-surface effects on interaction of multiple ships moving at different speeds. *Journal of Ship Research*, 63(04):251–267.

Zhou, X., Sutulo, S., and Guedes Soares, C. (2012). Computation of ship hydrodynamic interaction forces in restricted waters using potential theory. *Journal of Marine Science and Application*, 11(3):265–275.

Zou, L. and Larsson, L. (2013). Numerical predictions of ship-to-ship interaction in shallow water. *Ocean Engineering*, 72:386–402.